Micro-particles as thermal probes in a low-pressure rf-discharge

Dissertation
zur Erlangung des Doktorgrades
der Mathematisch-Naturwissenschaftlichen Fakultät
der Christian-Albrechts-Universität zu Kiel

vorgelegt von
Horst R. Maurer

Kiel,
Oktober 2010

Referent:	Prof. Dr. Holger Kersten, Universität Kiel
Korreferent:	Prof. Dr. Ir. G.M.W. Kroesen, Eindhoven University of Technology
Tag der mündlichen Prüfung:	03.12.2010
Zum Druck genehmigt:	03.12.2010

gez. Prof. Dr. Lutz Kipp, Dekan

Kurzfassung

In dieser Dissertation wird eine Methode zur Messung der Temperatur von Mikropartikeln in einem Plasma vorgestellt und die Verwendung dieser Partikel zur Bestimmung der relevanten Energieflüsse diskutiert. Diese Temperaturdiagnostik kann zur Charakterisierung von partikelhaltigen Prozessplasmen dienen, in denen die Oberflächentemperatur einen wichtigen Parameter in plasmatechnischen Verfahren darstellt. Darüber hinaus eröffnet die Kenntnis der Partikeltemperatur einen alternativen, nichtelektrischen Zugang zum Verständnis von Plasma-Wand-Wechselwirkungen, der ergänzend zu konventionellen Methoden wertvolle Informationen liefern kann.

Zur Messung der Temperatur werden temperatursensitive optische Eigenschaften geeigneter Leuchtstoffpartikel benutzt, die von einer externen Strahlungsquelle zur Lumineszenz angeregt werden. Frühere Untersuchungen der Partikeltemperatur waren auf gepulste Plasmaquellen begrenzt oder zeigten ein sehr schnelles Ausbleichen der verwendeten Leuchtstoffe, was beides einen negativen Einfluss auf die Genauigkeit der Messungen hatte. In dieser Arbeit werden erstmals systematische Messungen sowohl in Edelgas als auch unter Zumischung von Molekulargasen durchgeführt, die keine dieser Einschränkungen aufweisen. Der statistische Fehler der gemessenen Temperaturen liegt im Bereich von nur wenigen K. Dies erlaubt die Identifizierung systematischer Abweichungen, die durch eine Aufheizung des Plasmagefäßes während des Betriebes entstehen, sowie z.B. eine Quantifizierung des Einflusses externer Wärmequellen. Darüber hinaus lässt sich sehr gut der direkte Einfluss veränderter Entladungsparameter auf die Partikeltemperatur studieren, da die Temperaturmessung unabhängig von den Entladungsbedingungen ist.

Unter Zuhilfenahme der Sondentheorie lässt sich für die Mikroteilchen ein kalorimetrisches Bilanzmodell aufstellen, in der die Partikeltemperatur als Observable auftaucht. Eine Energiebilanz bei niedrigem Gasdruck in Argon kann in sich geschlossen über den gesamten Parameterbereich beschrieben werden. Der wesentliche Prozess zur Aufheizung der Mikropartikel ist demnach durch die Rekombination von Elektronen und Ionen an der Partikeloberfläche gegeben. Die Partikeltemperatur bei höheren Gasdrücken in Argon, wo die Beschreibung der Ionentrajektorien durch Orbitalbahnen ihre Gültigkeit verliert, entspricht qualitativ dem zu erwartenden Verhalten. In einem weiteren Schritt wird die Komplexität des Plasmas erhöht, indem ein Molekulargas beigemischt wird. In der Energiebilanz taucht nun ein weiterer Term auf, der den energetischen Beitrag der Rekombination dissoziierter Moleküle an der Partikeloberfläche berücksichtigt. Unter den untersuchten Entladunsbedingungen mit 9 Pa Argon und 1 Pa Wasserstoff liegt der Anteil dieses Beitrags zum totalen Energieeinstrom bei etwa 1/5. Ein wesentlicher Energieeintrag geschieht hier also durch Assoziationsprozesse an der Partikeloberfläche. Der damit verbundene Dissoziationsgrad entspricht der zu erwartenden Grössenordnung.

Abstract

In this thesis, a method for the measurement of the temperature of micro-particles in a plasma is presented and the utilization of the particles for the determination of the relevant energy fluxes is discussed. This temperature diagnostic can be used for the characterization of particle-containing process plasmas, where the surface temperature is an important parameter in plasma-based surface processing. Additionally, the knowledge of particle temperatures offers the opportunity of an alternative, non-electrical approach to plasma-surface interactions, which in addition to conventional plasma diagnostics could provide valuable information.

For the measurement of particle temperatures, temperature-sensitive optical features of suitable phosphor grains are utilized, which can be excited by means of an external illumination source. Former investigations of the particle temperature in plasmas were limited to pulsed plasma operation or showed rapid bleaching of the utilized phosphors, thus affecting the measurement accuracy. In this thesis, systematic measurements are performed for the first time both in noble gas and in molecular gas mixtures which do not depend on the mentioned limitations. The Statistical error of the measured temperatures is about few K. This allows for the identification of systematic deviations caused by heating of the plasma chamber during operation or e.g. of the influence of external heat sources. Moreover, the direct influence of changing discharge parameters can be studied because the temperature measurement is independent of the discharge conditions.

Based on probe theory, a calorimetric balance model for the micro-particles can be established where the particle temperature occurs as an observable. An energy balance at low pressures in argon can be established consistently within the whole parameter range. According to this, the fundamental process for particle heating is the result from the recombination of electrons and ions at the particle surface. At higher argon pressures where the description of ion trajectories by orbital motion becomes inappropriate, the particle temperature qualitatively shows the expected behavior. In a next step, the complexity of the plasma is increased by adding molecular gas. Now an additional term occurs in the energy balance, describing the contribution from the association of dissociated molecules at the particle surface. For the investigated conditions with 9 Pa argon and 1 Pa hydrogen, the contribution due to association processes at the particle surface is about 1/5. Hence, a fundamental energy source for particle heating is the recombination of dissociated hydrogen at the particle surface. The degree of dissociation, connected to this contribution, is in accordance to the expected order of magnitude.

Contents

1. Introduction **1**
- 1.1. Occurrence of plasmas . . . 2
- 1.2. Definition and properties of plasmas . . . 7
- 1.3. Capacitively coupled rf discharges . . . 8
- 1.4. Confinement of micro-particles in an rf-discharge . . . 11

2. Theory **17**
- 2.1. OML collection of charge carriers by a small object immersed in a plasma . . . 17
- 2.2. Evaluation of Langmuir probe characteristics . . . 22
- 2.3. Energy balance of substrates in a plasma environment . . . 25
  - 2.3.1. Self-consistent calculation of the floating potential . . . 29
- 2.4. Macroscopic bodies in a plasma environment . . . 30

3. Thermographic phosphors **35**
- 3.1. Luminescence . . . 35
- 3.2. The influence of temperature on phosphor materials . . . 36
- 3.3. Thermographic phosphors . . . 37
- 3.4. The fluorescent method for temperature measurement of micro-particles in a plasma . . . 38

4. Experimental work **46**
- 4.1. Experimental Setup . . . 46
- 4.2. Langmuir probe measurements . . . 48
- 4.3. Particle temperature measurements . . . 51
- 4.4. Calorimetric probe measurements . . . 59

5. Discussion of the energy balance **63**
- 5.1. Plasma parameters . . . 63
- 5.2. Energy flux to the dummy substrate . . . 64
- 5.3. Particle temperatures and plasma-particle interaction . . . 67

6. Summary and conclusion **74**

List of Figures **77**

List of Tables **81**

A. List of abbreviations **82**

1. Introduction

Today, plasma technology is a key feature in many emerging industrial sectors like microelectronics, nanotechnology, optics, biological or medical industry and many others, dealing with surface modification. Here, the energetic conditions at the surface of a substrate in processes like sputtering, plasma etching or thin film deposition are crucial for the improvement of such applications with respect to morphology, stoichiometry and process rates [1, 2, 3, 4, 5]. Hence, monitoring and controlling the constitutional parameters like gas pressure and composition or substrate temperature is essential, and understanding the plasma-surface interaction plays a key role in the design of the process conditions. A prominent tool for the quantification of energy fluxes towards a substrate are calorimetric probes, first invited by Thornton [6]. The temperature change of a dummy substrate allows the measurement of the integral power deposition. Moreover, different energy contributions, e.g. kinetic energies of electrons and ions as well as the released recombination energy, can be separated by biasing the substrate [7, 8, 9, 10].

Beneath treating macroscopic wafers in plasmas, also the plasma-based synthesis and modification of powder with specific properties offers a variety of new applications [11, 12, 13, 14, 15, 16, 17, 18, 19]. Some of them are the improvement of optical or mechanical properties for coatings [14, 19], for sintering processes [15], disperse composite catalysts [11] or polymorphous solar cells [12, 13]. In the case of small particles in low pressure plasmas, the electronic and energetic conditions at their surface are affected by their size and geometry [20, 21, 22, 23], and their surface temperature is determined by the balance of energy exchange with its environment. Several studies addressed the grain temperature, both theoretically [23, 24, 25, 26] and experimentally [27, 28, 29, 30, 31, 32, 33, 34]. Daugherty and Graves measured the temperature-dependent decay time of the fluorescence of manganese activated magnesium fluorogermanate particles in a pulsed argon discharge during the plasma-off phase [27]. Swinkels at al. utilized Rhodamine-B dyed melamine-formaldehyde particles, and compared their temperature-dependent emission spectrum in the plasma to spectra from an calibration oven [34]. Oliver and Enikov measured the incandescent radiation from particles in a plasma jet, which of course is only possible at rather high particle temperatures above $T_\mu = 1000$ K.

But the knowledge of the temperature of micro-particles is not only beneficial for the improvement of technical plasmas. The interaction of micro-particles or commonly of objects with plasmas is still not fully understood. A new, semi-invasive diagnostic tool for plasma-surface interaction could offer the possibility to obtain valuable supplemental information and, thus, improve the understanding of the related basic phenomena. This could in return be of concern for theoretical and astrophysical questions, as well as for plasma physics in general.

The aim of this work is to qualify micro-particles as a diagnostic tool for the measurement of the particle temperature and as calorimetric probes, based on the

observation of temperature-dependent luminescent features of the particles. Using this technique the performance of systematic measurements in argon and argon mixtures under variation of the plasma parameters is intended. Finally, the demonstration of the feasibility of the particles for the utilization as calorimetric probes is proposed, where a model is applied to describe the contribution of different energy fluxes (e.g. radiation, kinetic energies of charge carriers, energy release from recombination processes) to the micro-particle's energy balance.

Starting with a brief introduction, where the basic terms for this work are explained, the theoretical base for the description of the interactions between microparticles and plasma environment and the self-consistent calorimetric model are given in chapter 2. This description covers both the electrical as well as the energetic conditions at the particle surface. In chapter 3, the temperature-dependence of luminescence is explained and different phosphors are compared with respect to their feasibility for the measurements. In chapter 4 the detailed experimental setup and the measurement procedures are introduced for plasma experiments. Experimental results from the particle temperature measurements as well as from additional plasma diagnostics are shown for different plasma parameters. For comparison, also measurements with a calorimetric probe are shown. The results of the measurements are discussed in terms of validity of intrinsic assumptions and applicability of the calorimetric model in chapter 5. Then, the model is applied to measurement results obtained under low-pressure conditions in argon. The resulting findings are discussed and applied to a second iteration, where the complexity of the model is increased by the addition of a molecular gas to the plasma. Now, dissociation processes and plasma chemistry occurs and the energetic interaction between plasma and micro-particles has to account for energy release due to additional processes. The model results are compared to data from literature and its plausibility is discussed. Finally, a conclusion is drawn which would be of benefit for investigations in the near future.

1.1. Occurrence of plasmas

In ancient times, the Greeks divided matter into the four elements earth, water, air and fire. In analogy, we can experience matter to appear in four states of which the first three ones are solid ('earth'), fluid ('water') and gaseous ('air'). Solid matter can be molten by heat supply, resulting in a fluid, and by further heating the fluid can vaporize and form a gas. Each of these states has very characteristic properties, and the transition between these states implies the requirement of latent heat to overcome a barrier. Increasing the gas temperature leads to more and more energetic collisions between the gas particles. Inelastic collisions can occur, where kinetic energy is used to excite or even ionize gas particles. The result is a partially or fully ionized gas, containing ions and free electrons. With increasing ionization, the properties of the gas change. The electrical conductivity increases and the gas starts to emit light. At some point which is defined later it is not longer a gas but an electron-ion plasma, corresponding to the fourth element 'fire' of the Greeks. For simplicity, a plasma will be considered to be composed of neutrals, free electrons and singly charged positive ions in the following.

There are lots of examples for natural plasmas, for instance the hot plasma of the inner sun, the solar wind and solar eruptions. But also the earths ionosphere and magnetosphere are plasmas, which can trap energetic particles from the solar wind and guide them towards the upper atmosphere in the polar regions, causing the occurrence of impressive northern lights, as shown in fig. 1.1. Another prominent example are lightnings, even if these atmospheric discharges only exist for some milliseconds. Despite natural plasmas a lot of technical plasmas exist, which often are powered by external electrical fields. The technical analogon for lightnings are electrical sparks or arc discharges, used in electrical disruptive devices, for plasma cutting and arc welding. Electric fields can be used to accelerate free electrons, which usually are always present in a gas due to natural radiation. Due to collisions, the energetic electrons then create a plasma containing hot electrons and cold ions which sometimes are just above gas temperature. Such cold plasmas can be in contact to surfaces without thermal destruction. An example for such a plasma is shown in fig. 1.3. These plasmas are used in many applications, e.g. for illumination devices like fluorescent tubes and lamps, arc lamps or plasma displays. A large field of technical applications is connected to industrial surface processing, e.g. plasma etching, plasma assisted deposition of thin layers or plasma surface modification. These processes are used for the production of semiconductors, of layers with specific optical, electrical or mechanical properties like solar cells or for cleaning purposes. Recently large effort was put into research on plasma medicine and dental technologies. Other applications are found in analytic techniques like spectroscopy or in propulsion devices for spacecrafts. A prominent example for hot technical plasmas is controlled fusion research, where a plasma is confined by electromagnetic fields and heated to more than a hundred million Kelvins to ignite a nuclear fusion process similar to that in the sun. A detailed overview on natural and technical plasmas is given in textbooks like [40].

An interesting point of plasma physics, not only because of numerous technical applications as mentioned above, is their interaction with surfaces and - in particular - with dust. One could think in nature the occurrence of dust in a plasma is rather exceptional, but there are many examples in the extraterrestrial environment: Interstellar clouds like the Eagle Nebula (shown in fig. 1.2) or the Horsehead nebula, comets with tails split into a gas and a dust tail, or the phenomenon of noctilucent clouds in the earth's upper atmosphere. If a surface is in contact with a plasma, it will initially be hit by more electrons than ions due to the large mobility of the light electrons. The net collection of electrons leads to charging of the surface and a nearly electron-free region in front of the surface, called the 'sheath'. The surface potential becomes more negative with respect to the plasma, repelling electrons and attracting ions. At a certain negative potential electron and ion current are equal and equilibrium is achieved. Of course, under certain conditions this charging process can be dominated by others, for example by photoionization from a strong uv source and the surface potential can become positive with respect to the plasma environment. In technical plasmas, the surface potential is often utilized for the acceleration of ions towards the surface to perform anisotropic etching, to implant ions or to sputter the surface. Moreover, the electrical field occurring in the sheath

Figure 1.1: Northern lights in the cloudless sky over Bear Lake, Alaska at January 18, 2005. Photographer: Joshua Strang, USAF. Shown is the not digitally processed version of this famous photograph. Downloaded from [35].

Figure 1.2: Dust pillar of the Eagle Nebula, photographed by the Hubble telescope by NASA, ESA, STScI/AURA. Downloaded from [36].

Figure 1.3: Gas discharge being operated by Raymond W. Plamer at the Lewis Electromagnetic Propulsion Division, Cleveland, Ohio 1961. Photograph downloaded from [37].

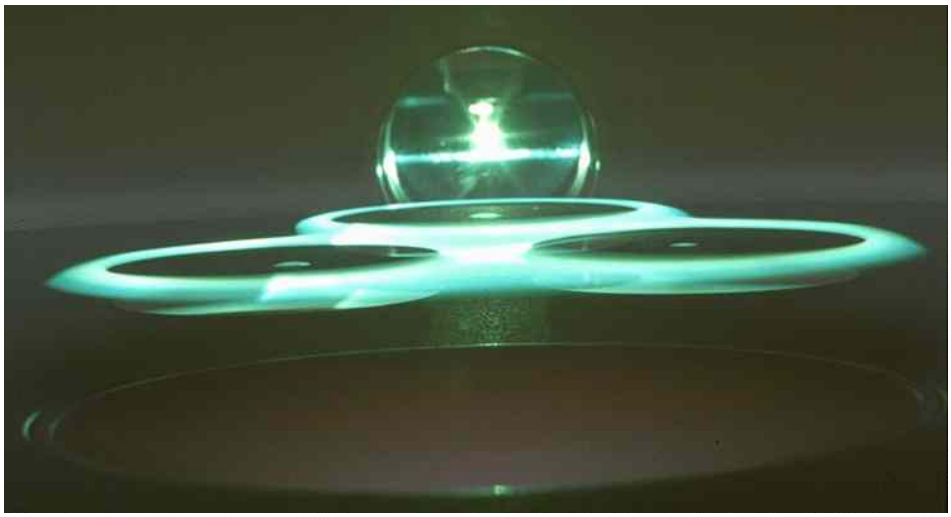

Figure 1.4: Dust cloud, formed in a processing plasma above three Si wafers and irradiated by a laser sheet, as published by G. Selwyn and co-workers in [38]. Image from [39].

in front of a surface is not only able to repel free electrons, but it can also repel microscopic particles, which are charged negatively from the plasma. Under certain conditions nano- or micro-sized particles can be confined in a stable position where the net force on the particles (which is mainly gravitation and electric force for micrometer scaled particles in typical gas discharges) is zero. The discovery in the late 1980s of 'killer particles' in silicon etching plasmas forming in-situ [38, 42] was an important step in the improvement of semiconductor industry and opened a completely new field of applications. A photograph of Selwyn's discovery is shown in fig. 1.4, where dome-shaped dust clouds are formed above three silicon wafers, made visible by illumination due to a laser sheet through the window of the discharge chamber.

If the charge on the particles is high enough and the particle density is sufficient, they can behave like an additional plasma species and show collective behavior. Then one speaks of a 'dusty plasma'. Collective behavior becomes manifest in order phenomena like wave propagation and dust crystals, which can be observed in real time using video microscopy. Fig. 1.5 shows a monolayer of monodisperse charged dust particles, confined in the electrical field in front of an electrode. The direct and inexpensive observability in the lab grew dusty plasma research into a very active field since more than a decade. But also in extraterrestrial environment collective phenomena can be observed, for example so-called spokes in the rings of Saturn. A more detailed overview on dusty plasmas can be found in textbooks [40, 43, 44] or in several review articles [45, 46, 47].

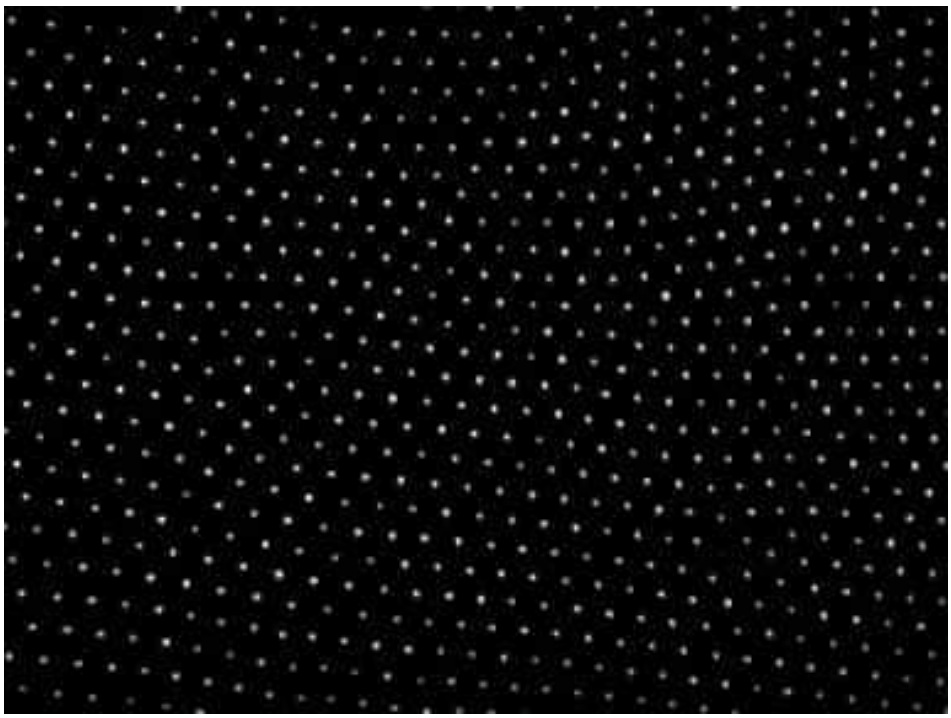

Figure 1.5.: Plasma crystal, forming a single layer in the plasma sheath, illuminated by laser radiation. Image taken from [41].

1.2. Definition and properties of plasmas

In analogy to a neutral gas, which is characterized by a number density n and a temperature T of the gas species, a plasma is characterized by the charge carrier densities n_e, n_i and temperatures T_e, T_i of electrons and ions, respectively. Within the plasma, free electrons and ions interact. In the vicinity of a charge Q, the trajectories of electrons and ions respond to the charge's electrical Coulomb potential

$$\Phi_\mathrm{C}(r) = \frac{Q}{4\pi\varepsilon_0 r} \quad . \tag{1.1}$$

In this equation, ε_0 is the vacuum permittivity and r is the distance from the charge. The net charge carrier densities around Q change, tending to compensate its presence and obtaining quasi-neutrality. As a consequence the electric field of the charge is screened and it is no longer of Coulomb type. The resulting potential

$$\Phi_\mathrm{D}(r) = \frac{Q}{4\pi\varepsilon_0 r} \exp\left\{-\frac{r}{\lambda_\mathrm{D}}\right\} \tag{1.2}$$

is called 'Debye-Hückel potential' or 'Yukawa potential' and is also observed in electrolytes. The parameter λ_D is the 'Debye length' or screening length which is the characteristic scale length in a plasma at which the potential $\Phi_\mathrm{D}(\lambda_\mathrm{D})$ is reduced to the factor $1/e \cdot \Phi_\mathrm{D}(0)$. It is composed of an electron and an ion part

$$\lambda_\mathrm{D}^{-2} = \lambda_\mathrm{De}^{-2} + \lambda_\mathrm{Di}^{-2} \quad . \tag{1.3}$$

The electron Debye length is given by

$$\lambda_\mathrm{De} = \sqrt{\frac{\varepsilon_0 k_\mathrm{B} T_\mathrm{e}}{n_\mathrm{e,0}\, e_0^2}} \quad , \tag{1.4}$$

where T_e is the electron temperature and $n_\mathrm{e,0}$ the undisturbed electron density, k_B the Boltzmann constant and e_0 the elementary charge. The ion Debye length λ_Di is described similarly, using ion temperature T_i and density $n_\mathrm{i,0}$. In plasmas with cold ions ($T_\mathrm{i} \ll T_\mathrm{e}$), the ion term is often dropped because $\lambda_\mathrm{D} \approx \lambda_\mathrm{De}$ and the shielding is mainly performed by the more mobile electrons. On a macroscopic scale, a plasma is quasi-neutral because the charge carriers can quickly response to electrical fields. However, on short scales in the order of λ_D, spatial charge fluctuations can develop. Typical values for λ_D are in the order of 10^{-4} m in laboratory plasmas.

But where is the difference between a plasma and a partially ionized gas? A compact and concise definition has been formulated by F.F. Chen [48], who wrote

> *a plasma is a quasineutral gas of charged and neutral particles which exhibits collective behavior.* (1.5)

These requirements can be explained as follows: An ionized gas is quasineutral, only if its size is large compared to the Debye length λ_D and disturbances remain small compared to the system. The plasma species show collective behavior, if a large quantity of charge carriers is coupled via electromagnetic interaction, i.e. if a large

quantity of charge carriers can respond to each other or if the number density of charge carriers within a sphere of radius λ_D is large. Furthermore, to show collective behavior also the life time of the plasma must remain sufficiently long. An electron can traverse a distance of the order of λ_D within a time of $\tau_\mathrm{e} = \lambda_\mathrm{D}/v_\mathrm{e}$, where the electron velocity v_e may be approximated the electron thermal velocity if the disturbance is small. Hence the plasma must exist over a time span of $T \gg \tau_\mathrm{e}$ This response time τ_e is a characteristic quantity, usually used in form of a frequency

$$\omega_\mathrm{pe} = \sqrt{\frac{n_{\mathrm{e},0} e_0^2}{\varepsilon_0 m_\mathrm{e}}} \quad , \tag{1.6}$$

called the electron 'plasma frequency'. In eqn. (1.6), m_e is the electron mass. Of course collisions within a plasma occur, but the long-range interaction of plasma species should not be destroyed by collisions. This is the case if the collision frequency is smaller than the frequency of typical plasma oscillations ω_pe. If these requirements are fulfilled, the behavior of plasma species fundamentally differs from that of gas particles, determined by short-range Van-der-Waals collisions and showing no long-range interaction, and the term 'plasma' is used. A more detailed description can be found in introductive textbooks about plasma physics [40, 48].

1.3. Capacitively coupled rf discharges

Low-temperature plasmas can be generated in different ways. In technical applications often electric fields are used as a power source to generate and sustain a plasma [49]. Here, plasma ignition is started by accelerating free electrons to energies above the ionization threshold, which are to some extent present in the gas due to cosmic radiation and natural radioactivity. The energetic electrons can undergo inelastic collision with neutrals, and more free electrons are produced which can participate in the process. If sufficient energy is deposited in the gas, an avalanche-like series of reactions can occur until the ionization rate is balanced by recombination processes, and a plasma can form. Electrical discharges can be classified as alternating current (ac) discharges, direct current (dc) discharges or pulsed (ac or dc) discharges. The ac discharges can be operated in the microwave region, where a frequency of $\omega_\mathrm{mw}/(2\pi) = 2.45$ GHz is widely used. The radio-frequency (rf) region ranges around 1 MHz $\leq \omega_\mathrm{rf}/(2\pi) \leq$ 100 MHz. The frequency of $\omega_\mathrm{rf}/(2\pi) = 13.56$ MHz and its harmonics are liberalized for technical applications and widely used. At this frequency, under typical conditions the relation

$$\omega_\mathrm{pe} \gg \omega_\mathrm{rf} \gg \omega_\mathrm{pi} \tag{1.7}$$

is found, where ω_pe is the electron plasma frequency defined in eqn. (1.6), and ω_pi is the analogous ion plasma frequency. As electrons and ions cannot respond to oscillations much higher than their plasma frequencies, the electrons respond to an rf field instantly, whereas the ion inertia is too large and they remain stationary. Thus, the electrons can be energized exclusively, and due to their small energy loss in elastic electron-heavy particle collisions the electron population becomes hot.

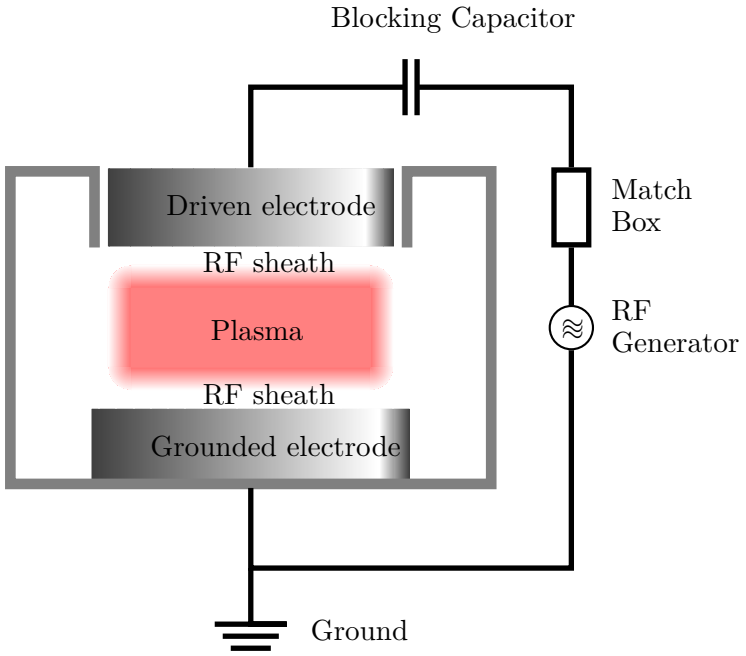

Figure 1.6.: Scheme of a capacitively coupled rf discharge similar to PULVA-INP. Bottom electrode and vacuum chamber are grounded, the upper electrode is driven. Between the electrodes the plasma establishes, separated from the electrode surface by an rf sheath.

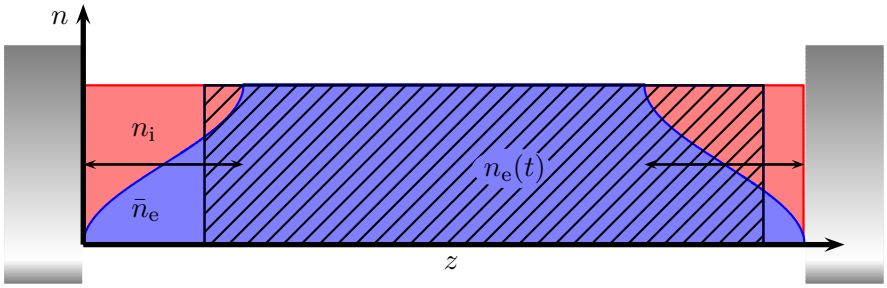

Figure 1.7.: Simple sketch of the electron and ion population between two symmetrical rf electrodes. Here, the ion density (red) is assumed to be homogeneous and stationary, while the electrons (hatched area) move back and forth with the applied rf voltage. Also the time-averaged electron density (blue) is shown.

In the same time, energy transfer for elastic ion-neutral collisions is effective and kinetic ion energy is easily dissipated.
There are different ways of coupling rf power to the discharge volume. One possibility is to use inductive coils inside or outside of the discharge vessel. This type of 'inductive coupled' discharge achieves high plasma densities because induced electrical fields are parallel to the plasma boundary. Another possibility is 'capacitively coupling', where the plasma may be generated between two parallel electrodes. A sketch of a typical capacitively coupled rf discharge is shown in fig. 1.6. Two disk-shaped electrodes are located inside a vacuum vessel. The distance between both electrodes is typically up to 100 mm. One of the electrodes is grounded, the other one is driven by an rf generator. Because the plasma impedance is changed especially if the type of gas or the gas pressure is varied and the generator usually is designed for a load of 50 Ω, a variable impedance matching network (match box) is required. The discharge power typically varies from 10 W to 100 W up to 2 kW in plasma etching applications. Furthermore, often a blocking capacitor is used to avoid a dc current flowing through the plasma. This capacitor causes the occurrence of a negative dc 'self bias' potential at the electrodes, which is influenced by the relative electrode area [50]. The plasma is formed between the electrodes at gas pressures of typically 1 to 100 Pa. A simple sketch is shown in fig. 1.7, where the ion population is assumed to be homogeneous and stationary, while the electron population responds instantly to the rf field and performs a sinusoidal oscillation. Their density $n_\mathrm{e}(t)$ equals the ion density n_i in the plasma bulk, where quasi-neutrality is given and electrons can not reach the electrode. In the moving region where electrons would hit the electrode during the rf cycle, $n_\mathrm{e}(t) = 0$. This is of course a very simplified picture, but it shows an important feature: As a consequence of the oscillation, the time-averaged electron density monotonically decreases towards the electrodes in a region where no (time-averaged) quasi-neutrality is given and which is referred to as 'rf sheath'. At every position z within the rf sheath, an electron duty cycle $\alpha(z)$ can be defined [51] via

$$\alpha = \alpha(z) := \frac{\bar{n}_\mathrm{e}(z)}{n_\mathrm{i}(z)} \quad , \tag{1.8}$$

where α is a small fraction of the rf-cycle when quasi-neutrality appears. Commonly, α has been estimated to be in the order of 0.1 [52]. In a more realistic picture, where ions are accelerated towards the electrodes due to the potential drop in the rf sheath, electrons can reach the electrode for a short interval within the rf cycle. During the remainder, they are repelled from the electrode by the negative self bias potential, and the time averaged net current is zero. The rf sheath can be split into a nearly quasi-neutral 'presheath' and a nearly electron-free sheath, which are separated by the 'sheath edge' [53]. In the presheath, a self-consistent solution requires the acceleration of ions towards the sheath edge, where they reach ion sound velocity

$$v_\mathrm{B} = \sqrt{\frac{k_\mathrm{B} T_\mathrm{e}}{m_\mathrm{i}}} \quad , \tag{1.9}$$

which is also known as 'Bohm velocity' [40]. The potential drops about $k_B T_e/(2e_0)$ within the presheath. Furthermore, the acceleration of ions towards the electrodes causes the ion density to decrease, forming a non-homogeneous ion density profile which is decreasing towards the electrodes. At the position of the sheath edge, the ion density $n_{i,s}$ can be estimated to be reduced by a factor of $\exp\{-0.5\}$ with respect to the plasma volume ($n_{i,0}$)

$$n_{i,s} = n_{i,0} \exp\left\{-\frac{1}{2}\right\} \tag{1.10}$$

if ion collisions are neglected.

The self bias potential, apparent in capacitively coupled rf-discharges is a useful tool in plasma technology, where it can be used for the acceleration of ions towards substrates. Moreover, electrical contact between plasma and electrodes is not required as no net current is flowing. Electrodes can be covered with dielectrics, which offers the possibility to treat non-conducting surfaces in a plasma (dielectric barrier discharge) [49, 51].

1.4. Confinement of micro-particles in an rf-discharge

As mentioned above, any object in contact to the plasma is hit by free electrons and ions. Due to the much larger mobility of the electrons, the electron flux towards the object is initially much higher than that of the ions. Thus, if processes like photodetachment or secondary emission can be neglected, negative charge is accumulated on the object and a negative potential is established. As a consequence the electron flux is reduced. When a specific electrical object potential is achieved - which is called the floating potential V_f - electron and ion flux are balanced and no further net charging occurs. A micro-particle in an rf discharge is, hence, negatively charged with respect to the plasma. Inside the plasma it is affected by different forces, e.g. by gravitation, ion drag or thermophoretic forces. However, for micro-particles with mass m_μ the gravitational force $\vec{F}_g = m_\mu \vec{g}$ is by far the most important one, and the particle will sink downwards. Here, $\vec{g}$ is the earth's gravity constant in form of a vector.

As a consequence from the violation of quasi-neutrality in the (time-averaged) rf sheath an electrical field exists which increases towards the electrodes and is directed away from the plasma volume. For negatively charged particles in this region, an electrostatic force $\vec{F}_{el} = Q\vec{E}$ exists which is directed towards the plasma volume. $Q = \pm Z e_0$ is the charge of the particle, where Z is the number of positive elementary charges e_0.

The electrical field, which is shown in fig. 1.8 on the left, can at least partwise be approximated by a linear function [54] and increases towards the electrode. In contrast, the gravitational force remains constant. Under conditions which are typically found in rf discharges, the electrostatic force F_{el} on a micro-particle at floating potential V_f is of the same order than F_g. If both forces show in opposite directions, which is the case in front of a bottom electrode, the effective potential

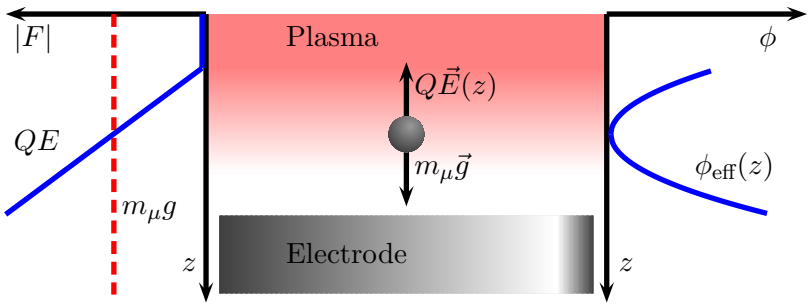

Figure 1.8.: Micro-particle, confined in the rf sheath in front of an electrode (center). Its vertical equilibrium position is mainly determined by gravitational and electrostatic force F_{g} and F_{el} (left). The effective vertical confinement potential $\phi_{\text{eff}}(z)$ in the vicinity of the particle can be approximated by a parabolic potential well (right).

for the micro-particle is

$$-\nabla\phi_{\text{eff}}(z) = m_\mu g - QE(z) \quad . \tag{1.11}$$

It can, thus, show a minimum at a position z_μ within the rf sheath where the local effective potential is approximately harmonic (fig. 1.8 right). Then, the micro-particle is confined at a position z_μ in the rf-sheath without mechanical contact to any solid surface (fig. 1.8 center).

The particle charge Q of a small grain with radius $r_\mu \ll \lambda_{\text{D}}$ can be linked to its floating potential V_f using the model of a spherical capacitor [40, 43, 44] in vacuum with a capacitance of $C = 4\pi\varepsilon_0 r_\mu$. The constant ε_0 is the vacuum permittivity. From this, the particle charge becomes

$$Q = C \cdot V_f = 4\pi\varepsilon_0 r_\mu V_f \quad . \tag{1.12}$$

A more detailed, quantitative description of the charging of micro-particles and of their floating potential will be given in the next chapter.

Bibliography

[1] S. D. Bernstein, T. Y. Wong and R. W. Tustison: *Comparison of the temperature dependence of the properties of ion beam and magnetron sputtered Fe films on (100) GaAs.* J. Vac. Sci. Technol. A **17** (2), pp. 571–576 (1999). See page: 1

[2] C. Cardinaud, M. Peignon and P. Tessier: *Plasma etching: principles, mechanisms, application to micro- and nano-technologies.* Appl. Surf. Sci. **164** (2000). See page: 1

[3] J. G. Han: *Recent progress in thin film processing by magnetron sputtering with plasma diagnostics.* J. Phys. D Appl. Phys. **42** (4), p. 043001 (2009). See page: 1

[4] A. von Keudell: *Surface processes during thin-film growth.* Plasma Sources Sci. T. **9** (4), p. 455 (2000). See page: 1

[5] B. Window: *Recent advances in sputter deposition.* Surf. Coat. Tech. **71** (2), pp. 93 – 97 (1995). See page: 1

[6] J. A. Thornton: *Substrate heating in cylindrical magnetron sputtering sources.* Thin Solid Films **54** (1), pp. 23 – 31 (1978). See page: 1

[7] H. Kersten, D. Rohde, H. Steffen, H. Deutsch, R. Hippler, G. H. P. M. Swinkels and G. M. W. Kroesen: *On the determination of energy fluxes at plasma-surface processes.* Appl. Phys. A Mater.: **72**, pp. 531–540 (2001). See page: 1

[8] D. Lundin, M. Stahl, H. Kersten and U. Helmersson: *Energy flux measurements in high power impulse magnetron sputtering.* J. Phys. D Appl. Phys. **42** (18), p. 185202 (7pp) (2009). See page: 1

[9] M. Stahl, T. Trottenberg and H. Kersten: *A calorimetric probe for plasma diagnostics.* Rev. Sci. Instrum. **81** (2), 023504 (2010). See page: 1

[10] A.-L. Thomann, N. Semmar, R. Dussart, J. Mathias and V. Lang: *Diagnostic system for plasma/surface energy transfer characterization.* Rev. Sci. Instrum. **77** (3), 033501 (2006). See page: 1

[11] A. V. Gavrikov, A. S. Ivanov, A. F. Pal, O. F. Petrov, A. N. Ryabinkin, A. O. Serov, Y. M. Shulga, A. N. Starostin and V. E. Fortov: *Dusty Plasma Technology of DCM with Nanostructure Surface Layer Production.* AIP conf. proc. **1041**, pp. 237–238. AIP (2008). See page: 1

[12] P. R. i Cabarrocas, N. Chaâbane, A. V. Kharchenko and S. Tchakarov: *Polymorphous silicon thin films produced in dusty plasmas: application to solar cells.* Plasma Phys. Contr. F. **46** (12B), p. B235 (2004). See page: 1

[13] P. R. i Cabarrocas, Y. Djeridane, T. Nguyen-Tran, E. V. Johnson, A. Abramov and Q. Zhang: *Low temperature plasma synthesis of silicon nanocrystals: a strategy for high deposition rate and efficient polymorphous and microcrystalline solar cells.* Plasma Phys. Contr. F. **50** (12), p. 124037 (2008). See page: 1

[14] P. R. i Cabarrocas, P. Gay and A. Hadjadj: *Experimental evidence for nanoparticle deposition in continuous argon–silane plasmas: Effects of silicon nanoparticles on film properties.* J. Vac. Sci. Technol. A **14**, pp. 655–659. AVS (1996). See page: 1

[15] T. Ishigaki, T. Sato, Y. Moriyoshi and M. I. Boulos: *Influence of plasma modification of titanium carbide powder on its sintering properties.* J. Mater. Sci. Lett.**14** (23), pp. 1694–1697 (1995). See page: 1

[16] H. Kersten, H. Deutsch, E. Stoffels, W. W. Stoffels and G. M. W. Kroesen: *Plasma-powder interaction: trends in applications and diagnostics.* Int. J. Mass Spektrom. **223-224**, pp. 313 – 325 (2003). See page: 1

[17] H. Kersten, H. Deutsch, E. Stoffels, W. W. Stoffels, G. M. W. Kroesen and R. Hippler: *Micro-Disperse Particles in Plasmas: From Disturbing Side Effects to New Applications.*
Contrib. Plasm. Phys. **41** (6), pp. 589–609 (2001). See page: 1

[18] U. Kortshagen: *Nonthermal plasma synthesis of semiconductor nanocrystals.* J. Phys. D Appl. Phys. **42** (11), p. 113001 (2009). See page: 1

[19] E. Stoffels, W. W. Stoffels, G. Ceccone, R. Hasnaoui, H. Keune, G. Wahl and F. Rossi: *MoS[sub 2] nanoparticle formation in a low pressure environment.* J. Appl. Phys. **86** (6), pp. 3442–3451 (1999). See page: 1

[20] J. E. Allen: *Probe theory - the orbital motion approach.*
Phys. Scripta **45** (5), pp. 497–503 (1992). See page: 1

[21] C. Arnas and A. A. Mouberi: *Thermal balance of carbon nanoparticles in sputtering discharges.* J. Appl. Phys. **105** (6), 063301 (2009). See page: 1

[22] F. Galli and U. Kortshagen: *Charging, Coagulation, and Heating Model of Nanoparticles in a Low-Pressure Plasma Accounting for Ion - Neutral Collisions.* IEEE T. Plasma Sci. **38** (4), pp. 803 –809 (2010). See page: 1

[23] R. Piejak, V. Godyak, B. Alexandrovich and N. Tishchenko: *Surface temperature and thermal balance of probes immersed in high density plasma.* Plasma Sources Sci. T. **7** (4), pp. 590–598 (1998). See page: 1

[24] F. X. Bronold, H. Fehske, H. Kersten and H. Deutsch: *Towards a Microscopic Theory of Particle Charging.*
Contrib. Plasm. Phys. **49** (4-5, Sp. Iss. SI), pp. 303–315 (2009). See page: 1

[25] S. A. Khrapak and G. E. Morfill: *Grain surface temperature in noble gas discharges: Refined analytical model.* Phys. Plasmas **13** (10), 104506 (2006). See page: 1

[26] E. Stoffels, W. W. Stoffels, H. Kersten, G. H. P. M. Swinkels and G. M. W. Kroesen: *Surface processes of dust particles in low pressure plasmas.*
Phys. Scripta **2001** (T89), p. 168 (2001). See page: 1

[27] J. E. Daugherty and D. B. Graves: *Particulate temperature in radio frequency glow discharges.*
J. Vac. Sci. Technol. A **11** (4), pp. 1126–1131 (1993). See page: 1

[28] H. Maurer, R. Basner and H. Kersten: *Measuring the temperature of microparticles in plasmas.* Rev. Sci. Instrum. **79** (9), 093508 (2008). See page: 1

[29] H. Maurer, R. Basner and H. Kersten: *Micro-Particles As Thermal Probes In Plasmas.* AIP Conf. Proc. **1041**, pp. 283–284. AIP (2008). See page: 1

[30] H. R. Maurer, R. Basner and H. Kersten: *Temperature of particulates in low-pressure rf-plasmas in Ar, Ar/H2 and Ar/N2 mixtures.* Contrib. Plasm. Phys. **50** (10), pp. 1521-3986 (2010). See page: 1

[31] H. R. Maurer, S., M. Hannemann, R. Basner and H. Kersten: *Measurement of plasma-surface energy fluxes in an argon rf-discharge by means of calorimetric probes and fluorescent microparticles.* Phys. Plasmas **17** (11), p. 113707 (2010). See page: 1

[32] H. R. Maurer, V. Schneider, M. Wolter, R. Basner, T. Trottenberg and H. Kersten: *Microparticles as plasma diagnostic tools.* Manuscript accepted for publication in Contr. Plas. Phys. Special Issue for the 2010 International Conference on Plasma Diagnostics. See page: 1

[33] D. Oliver and R. Enikov: *Micro-particles temperature measurements in a plasma jet.* Vacuum **58** (2-3), pp. 244 – 249 (2000). See page: 1

[34] G. Swinkels, H. Kersten, H. Deutsch and G. M. W. Kroesen: *Microcalorimetry of dust particles in a radio-frequency plasma.* J. Appl. Phys. **88** (4), pp. 1747 – 1755 (2000). See page: 1

[35] *Downloaded at September 09, 2010 from http://www.af.mil/shared/media/photodb/photos/050118-F-3488S-003.jpg* . See page: 4, 77

[36] *Downloaded at September 09, 2010 from http://www.nasa.gov/images/content/205946main_eaglefairy_hst_big.jpg* . See page: 4, 77

[37] *Downloaded at September 09, 2010 from http://grin.hq.nasa.gov/ABSTRACTS/GPN-2000-001995.html* . See page: 5, 77

[38] G. S. Selwyn, J. E. Heidenreich and K. L. Haller: *Rastered laser light scattering studies during plasma processing: Particle contamination trapping phenomena.* J. Vac. Sci. Technol. A **9** (5), pp. 2817–2824 (1991). See page: 5, 6, 77

[39] *Downloaded at September 09, 2010 from http://www.mpe.mpg.de/theory/plasma-crystal/PKE/Bilder/Selwyn/gary15.gif* . See page: 5, 77

[40] A. Piel: *Plasma Physics.* Springer Verlag Berlin Heidelberg (2010). See page: 3, 6, 8, 11, 12

[41] *Downloaded at September 09, 2010 from http://www.mpe.mpg.de/pke/PKE/images/PK-soliton_cr.gif* . See page: 6, 77

[42] G. S. Selwyn, J. Singh and R. S. Bennett: *In situ laser diagnostic studies of plasma-generated particulate contamination.* J. Vac. Sci. Technol. A **7** (4), pp. 2758–2765 (1989). See page: 6

[43] A. Melzer: *Der Plasmakristall : Phasenübergang und Stabilität.* Harri Deutsch, Frankfurt/Main (1997). See page: 6, 12

[44] P. K. Shukla and A. A. Mamun: *Introduction to Dusty Plasma Physics.* IoP Publishing, London (2002). See page: 6, 12

[45] V. Fortov, A. Ivlev, S. Khrapak, A. Khrapak and G. Morfill: *Complex (dusty) plasmas: Current status, open issues, perspectives.* Phys. Rep. **421** (1-2), pp. 1 – 103 (2005). See page: 6

[46] D. A. Mendis: *Progress in the study of dusty plasmas.* Plasma Sources Sci. T. **11** (3A), p. A219 (2002). See page: 6

[47] P. K. Shukla: *A survey of dusty plasma physics.* Phys. Plasmas **8** (5), pp. 1791–1803 (2001). See page: 6

[48] F. F. Chen: *Introduction to Plasma Physics and controlled Fusion.* Plenum Press, New York (1974). See page: 7, 8

[49] R. Hippler, H. Kersten, M. Schmidt and K. H. Schoenbach (eds.): *Low Temperature Plasmas, 2nd revised and enlarged edition.* Wiley-VCH, Weinheim (2008). See page: 8, 11

[50] K. Köhler, J. W. Coburn, D. E. Horne, E. Kay and J. H. Keller: *Plasma potentials of 13.56-MHz rf argon glow discharges in a planar system.* J. Appl. Phys. **57** (1), pp. 59–66 (1985). See page: 10

[51] M. A. Lieberman and A. J. Lichtenberg: *Principles of Plasma Discharges and Materials Processing.* John Wiley and Sons, Inc., New York (1994). See page: 10, 11

[52] T. Trottenberg, A. Melzer and A. Piel: *Measurement of the electric charge on particulates forming Coulomb crystals in the sheath of a radiofrequency plasma.* Plasma Sources Sci. T. **4** (3), p. 450 (1995). See page: 10

[53] J. E. Allen: *The plasma-sheath boundary: its history and Langmuir's definition of the sheath edge.* Plasma Sources Sci. T. **18** (1), p. 014004 (2009). See page: 10

[54] E. B. Tomme, D. A. Law, B. M. Annaratone and J. E. Allen: *Parabolic Plasma Sheath Potentials and their Implications for the Charge on Levitated Dust Particles.* Phys. Rev. Lett. **85** (12), pp. 2518–2521 (2000). See page: 11

2. Theory

In this chapter the collection of electrons and ions by an object immersed in a plasma is described. In the model an idealized plasma is assumed where electrons show a Maxwellian velocity distribution, with streaming ions at the sheath edge and where collisions are negligible . It will be used to describe both particle and thermal fluxes between plasma and the surface and was originally used in probe theory [1]. In this concept, the flux of attracted charge carriers towards the object is limited due to their orbital trajectories, and it is therefore called Orbital Motion Limited (OML) theory or the Orbital Motion Limit.
After the introduction of the OML currents a brief description is given of the algorithm used for plasma diagnostics based on the evaluation of Langmuir probe characteristics. Then the energy fluxes between plasma and micro-particles are specified. Because charge carriers provide an essential part of the energy deposited onto the particle surface, electrical and thermal behavior are closely connected. Finally, the evaluation of temperature characteristics of macroscopic objects exposed to a plasma, are explained

2.1. OML collection of charge carriers by a small object immersed in a plasma

As mentioned earlier, in a laboratory plasma immersed objects and walls are negatively charged with respect to the plasma due to the higher electron mobility and reach an equilibrium potential V_f when electron current I_e and ion current I_i towards the surface become equal. We will now describe the collection of electrons and positive ions by a negatively charged spherical object at V_f with a diameter of $2r_\mu$, located inside a plasma at rest where collisions can be neglected. The plasma is considered to contain free electrons and ions with an electron velocity distribution which is described by the Maxwellian speed distribution function. The fraction of species with a speed $v = |\vec{v}|$ within the interval $v + dv$ is described by

$$f_\mathrm{M}(v)\,dv = \left(\frac{m}{2\pi k_\mathrm{B}T}\right)^{3/2} \exp\left\{-\frac{mv^2}{2k_\mathrm{B}T}\right\} 4\pi v^2 dv \quad , \tag{2.1}$$

$$\int_0^\infty f_\mathrm{M}(v)\,dv = 1 \quad .$$

Here, the exponential term is the Boltzmann factor which describes the speed distribution for a gas with temperature T in thermal equilibrium, where m is the mass of the gas species and k_B the Boltzmann constant. The factor in front of the Boltzmann term is for normalization purposes and $4\pi v^2\,dv$ accounts for the volume

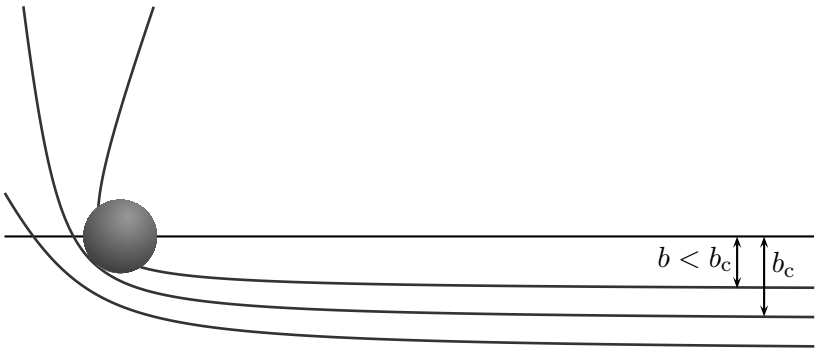

Figure 2.1.: Ion trajectories in the presence of a negatively charged microsphere. Due to the attracting potential, the unbound ions move in hyperbolic orbits.

element in three-dimensional velocity space. The mean speed of eqn. (2.1) is

$$\langle v \rangle = v_{\mathrm{th}} = \int_0^\infty f_{\mathrm{M}}(v) v \, dv \quad = \quad \sqrt{\frac{8 k_{\mathrm{B}} T}{\pi m}}$$

and the mean kinetic energy

$$\langle E \rangle = E_{\mathrm{kin}} = \frac{m}{2} \int_0^\infty f_{\mathrm{M}}(v) v^2 \, dv \quad = \quad \frac{3}{2} k_{\mathrm{B}} T \quad .$$

By substitution of $v = \sqrt{E/(2m)}$ and $dv = 1/\sqrt{2mE}\, dE$, the analogous expression of eqn. (2.1) can be obtained in energy units. With respect to electrons it is convenient to speak of a Maxwellian electron energy distribution function (EEDF), as the electron energy distribution can be accessed from the second derivative of Langmuir probe characteristics.

Ions

The ions are singly positively charged. Primarily located at a position far away from the object, they are attracted by the object and are thus accelerated towards it. The density is assumed to be low enough to neglect collisions. Possible ion trajectories are shown in fig. 2.1. Depending on the undisturbed (thermal) velocity $v = v_0$ of the ions far away from the object they possess an angular momentum and the trajectories of free ions in the electrical field of the object show a hyperbolic shape. Those ions with an impact parameter b smaller than the critical impact parameter b_{c} will hit the object, whereas ions with $b > b_{\mathrm{c}}$ will miss it. If $b = b_{\mathrm{c}}$ the ion will hit the object with grazing incidence. Its angular momentum at infinity is

$$\left| \vec{L} \right| = |\vec{r} \times \vec{p}| = m_{\mathrm{i}} v b_{\mathrm{c}}$$

If no collisions occur, the angular momentum is conserved when approaching the object, and

$$\left|\vec{L}\right| = m_\mathrm{i} v_\mu r_\mu \quad .$$

Here, v_μ describes the ion velocity at the radius r_μ where the radial motion is zero. Using conservation of energy, one can write

$$\frac{1}{2} m_\mathrm{i} v_\mu^2 = \frac{1}{2} m_\mathrm{i} v^2 - e_0 V_f \quad .$$

$$1 = \frac{v_\mu^2}{v^2} + 2\frac{e_0 V_f}{m_\mathrm{i} v^2} = \frac{b_\mathrm{c}^2}{r_\mu^2} + 2\frac{e_0 V_f}{m_\mathrm{i} v^2}$$

The critical impact parameter is hence described by

$$b_\mathrm{c} = r_\mu \left(1 - 2\frac{e_0 V_f}{m_\mathrm{i} v^2}\right)^{1/2}$$

with $b_\mathrm{c}/r_\mu > 1$. Due to the attractive potential $e_0 V_f < 0$, the effective surface is increased. For an ideal cylindrical object, where fig. 2.1 represents a plane through the radial cylinder axis, the cross section is increased by a factor b_c/r_μ. For a spherical object where the effective area πb_c^2 is a circle , the correction term is

$$\frac{b_\mathrm{c}^2}{r_\mu^2} = \left(1 - 2\frac{e_0 V_f}{m_\mathrm{i} v^2}\right) \quad . \tag{2.2}$$

If the ion velocity can be described by a directed drift speed $u_\mathrm{i} \gg v_\mathrm{th,i}$, it can be considered as a uniform flow. This is the case for cold ions, when they approach the ion sound (Bohm) velocity $v \approx v_\mathrm{B} = (k_\mathrm{B} T_\mathrm{e}/m_\mathrm{i})^{1/2}$ at the sheath edge. Thus, the ion current towards a spherical object located close to the sheath edge can be approximated via

$$I_\mathrm{i} = e_0 \pi r_\mu^2 n_\mathrm{i} \sqrt{\frac{k_\mathrm{B} T_\mathrm{e}}{m_\mathrm{i}}} \left(1 - 2\frac{e_0 V_f}{k_\mathrm{B} T_\mathrm{e}}\right) \tag{2.3}$$

as the product of ion density, Bohm velocity and the corrected collection area. From this, the ion flux density for a planar surface element facing towards the plasma volume becomes

$$j_\mathrm{i} = n_\mathrm{i} \sqrt{\frac{k_\mathrm{B} T_\mathrm{e}}{m_\mathrm{i}}} \left(1 - 2\frac{e_0 V_f}{k_\mathrm{B} T_\mathrm{e}}\right) \quad . \tag{2.4}$$

However, for non-plane geometry it has to be considered that the flow is not isotropic but a directed flow is present. For a spherical object with a surface $A \propto 4\pi r_\mu^2$, the projected area is just $A_\mathrm{eff} \propto \pi r_\mu$. The current has to be averaged over the full area. For a spherical object

$$j_\mathrm{i} = \frac{1}{4} n_\mathrm{i} \sqrt{\frac{k_\mathrm{B} T_\mathrm{e}}{m_\mathrm{i}}} \left(1 - 2\frac{e_0 V_f}{k_\mathrm{B} T_\mathrm{e}}\right) \quad . \tag{2.5}$$

Electrons

In analogy to the ions, the impact parameter for grazing incidence for electrons would be described by

$$b_\mathrm{c} = r_\mu \left(1 + 2\frac{e_0 V_f}{m_\mathrm{e} v^2}\right)^{1/2} \quad . \tag{2.6}$$

However, in contrast to the ions the electrons are repelled, and the fraction in the correction term obtains the opposite sign. Now $b_\mathrm{c}/r_\mu < 1$ and the effective collision cross section is reduced. If the electrons show an isotropic Maxwellian velocity distribution, the electron flux density j_e to a repulsing surface element can be obtained by

$$j_\mathrm{e} = n_\mathrm{e} \int_0^{2\pi} d\varphi \int_{v_\mathrm{min}}^{\infty} v^2\, dv \int_0^{\theta_\mathrm{max}} v \cos\theta f_\mathrm{M}(v,\theta,\varphi) \sin\theta\, d\theta$$

integrating over the Maxwellian velocity distribution function in vector notation

$$f_\mathrm{M}(\vec{v}) = \left(\frac{m}{2\pi k_\mathrm{B} T}\right)^{3/2} \exp\left\{-\frac{m\,|\vec{v}|^2}{2k_\mathrm{B} T}\right\} \quad . \tag{2.7}$$

The electrons are described by a velocity $v\cos\theta$ in normal directions towards the surface element and by an angle of incidence θ, which both are known far from the surface. The maximum angle is determined by the minimum velocity

$$v_\mathrm{min} = \sqrt{-2\frac{e_0 V_f}{m_\mathrm{e}}}$$

which is required to reach the surface. The maximum angle is, thus,

$$\theta_\mathrm{max} = \arccos\sqrt{-2\frac{e_0 V_f}{m_\mathrm{e} v^2}} \quad .$$

The electron flux density becomes

$$\begin{aligned} j_\mathrm{e} &= 2\pi n_\mathrm{e} \int_{v_\mathrm{min}}^{\infty} v^3\, dv \int_0^{\theta_\mathrm{max}} f_\mathrm{M}(v,\theta,\varphi) \sin\theta\cos\theta\, d\theta \quad , \\ &= \pi n_\mathrm{e} \int_{v_\mathrm{min}}^{\infty} v^3 f_\mathrm{M}(v,\theta,\varphi) \sin^2\left(\arccos\sqrt{-2\frac{e_0 V_f}{m_\mathrm{e} v^2}}\right) dv \quad , \\ &= \pi n_\mathrm{e} \int_{v_\mathrm{min}}^{\infty} v^3 f_\mathrm{M}(v,\theta,\varphi) \left(1 - \cos^2\left(\arccos\sqrt{-2\frac{e_0 V_f}{m_\mathrm{e} v^2}}\right)\right) dv \quad , \end{aligned}$$

$$= \pi n_\mathrm{e} \int\limits_{v_\mathrm{min}}^{\infty} v^3 f_\mathrm{M}(v,\theta,\varphi) \left(1 + 2\frac{e_0 V_f}{m_\mathrm{e} v^2}\right) dv \quad .$$

Inserting $f_\mathrm{M}(\vec{v})$ yields

$$j_\mathrm{e} = \pi n_\mathrm{e} \left(\frac{m_\mathrm{e}}{2\pi k_\mathrm{B} T_\mathrm{e}}\right)^{3/2} \int\limits_{v_\mathrm{min}}^{\infty} \left(1 + \frac{2e_0 V_f}{m_\mathrm{e} v^2}\right) v^3 \exp\left\{-\frac{m_\mathrm{e} v^2}{2k_\mathrm{B} T_\mathrm{e}}\right\} dv \quad .$$

We can identify the sum in the brackets as the factor b_c^2/r_μ^2, given in eqn. (2.6). A substitution into energy units, using $v = (2E/m_\mathrm{e})^{1/2}$ and $dv = (2m_\mathrm{e}E)^{-1/2} dE$ yields

$$j_\mathrm{e} = \frac{n_\mathrm{e}}{k_\mathrm{B} T_\mathrm{e}} \sqrt{\frac{1}{2m_\mathrm{e}\pi k_\mathrm{B} T_\mathrm{e}}} \int\limits_{-e_0 V_f}^{\infty} (E + e_0 V_f) \exp\left\{-\frac{E}{k_\mathrm{B} T_\mathrm{e}}\right\} dE \quad , \tag{2.8}$$

where the minimum kinetic energy of the impinging electrons of $E_\mathrm{min} = -e_0 V_f$, far away from the object is considered. This integral can be evaluated easily, and the result is

$$j_\mathrm{e} = \frac{1}{4} n_\mathrm{e} \sqrt{\frac{8k_\mathrm{B} T_\mathrm{e}}{\pi m_\mathrm{e}}} \exp\left\{\frac{e_0 V_f}{k_\mathrm{B} T_\mathrm{e}}\right\} \quad . \tag{2.9}$$

The different terms in this flux density can easily be identified as the mean thermal electron velocity and the Boltzmann factor. The term 1/4 considers a factor 1/2 for the amount of electrons moving towards the surface, and another factor 1/2 which results from the consideration of the incident angle θ.

To obtain the kinetic electron energy flux density J_e an integration over the electron energy times the electron flux density can be performed, using

$$J_\mathrm{e} dE = j_\mathrm{e} \left(E + e_0 V_f\right) dE \quad , \tag{2.10}$$

where the electron energy is corrected for the repulsive potential of the object. Starting from eqn. (2.8), one obtains

$$J_\mathrm{e} = \underbrace{\frac{n_\mathrm{e}}{k_\mathrm{B} T_\mathrm{e}} \sqrt{\frac{1}{2m_\mathrm{e}\pi k_\mathrm{B} T_\mathrm{e}}}}_{:=C} \int\limits_{-e_0 V_f}^{\infty} (E + e_0 V_f)^2 \exp\left\{-\frac{E}{k_\mathrm{B} T_\mathrm{e}}\right\} dE$$

$$= C \underbrace{\int\limits_{-e_0 V_f}^{\infty} E^2 e^{-\frac{E}{k_\mathrm{B} T_\mathrm{e}}} dE}_{①} + 2Ce_0 V_f \underbrace{\int\limits_{-e_0 V_f}^{\infty} E e^{-\frac{E}{k_\mathrm{B} T_\mathrm{e}}} dE}_{②} + Ce_0^2 V_f^2 \underbrace{\int\limits_{-e_0 V_f}^{\infty} e^{-\frac{E}{k_\mathrm{B} T_\mathrm{e}}} dE}_{③} \quad . \tag{2.11}$$

Using

$$① : \int_{-e_0V_f}^{\infty} E^2 e^{-\frac{E}{k_\mathrm{B}T_\mathrm{e}}} dE = \exp\left\{\frac{e_0V_f}{k_\mathrm{B}T_\mathrm{e}}\right\}\left(e_0^2V_f^2k_\mathrm{B}T_\mathrm{e} - 2e_0V_fk_\mathrm{B}^2T_\mathrm{e}^2 + 2k_\mathrm{B}^3T_\mathrm{e}^3\right)$$

$$② : \int_{-e_0V_f}^{\infty} E e^{-\frac{E}{k_\mathrm{B}T_\mathrm{e}}} dE = \exp\left\{\frac{e_0V_f}{k_\mathrm{B}T_\mathrm{e}}\right\}\left(k_\mathrm{B}^2T_\mathrm{e}^2 - e_0V_fk_\mathrm{B}T_\mathrm{e}\right)$$

$$③ : \int_{-e_0V_f}^{\infty} e^{-\frac{E}{k_\mathrm{B}T_\mathrm{e}}} dE = \exp\left\{\frac{e_0V_f}{k_\mathrm{B}T_\mathrm{e}}\right\}(k_\mathrm{B}T_\mathrm{e})$$

one obtains

$$J_\mathrm{e} = \frac{1}{4}n_\mathrm{e}\sqrt{\frac{8k_\mathrm{B}T_\mathrm{e}}{\pi m_\mathrm{e}}}\exp\left\{\frac{e_0V_f}{k_\mathrm{B}T_\mathrm{e}}\right\}2k_\mathrm{B}T_\mathrm{e} \tag{2.12}$$

$$= j_\mathrm{e}\cdot 2k_\mathrm{B}T_\mathrm{e} \tag{2.13}$$

From a comparison with eqn. (2.9) the factor $2k_\mathrm{B}T_\mathrm{e}$ can be identified as the mean kinetic energy of the impinging electrons. This result is different to the mean kinetic energy of the electron gas, which is $3/2k_\mathrm{B}T_\mathrm{e}$. This difference can be explained by a weighting of the more energetic electrons [2]. Furthermore one might wonder why this result is the same result than that which is obtained for a neutral gas [2], and no influence of V_f is included. However, it should be stated that this is a feature of the Maxwellian velocity distribution which is based on an exponential function. Even if the mean kinetic energy is unchanged, the number density j_e of incoming electrons and, thus, the kinetic energy flux density J_e are well influenced by V_f.

2.2. Evaluation of Langmuir probe characteristics

Langmuir probes, invented in the 1920es by Mott-Smith and Langmuir, are additional electrodes introduced into the plasma to study their current-voltage characteristics. From these characteristics it is possible to determine electron temperature T_e [1], electron density n_e and the plasma potential V_p and, hence, to obtain the basic plasma parameters. Despite their old history and their invasive character, they are still widely used in plasma physics because of their simplicity and versatility. There exist a wide repertory of alternative diagnostics, from optical spectroscopy over microwave interferometry to the determination of plasma oscillations, but none of these techniques is as inexpensive and simple to use as Langmuir probes. The advantage of a non-invasive method is often compensated by its non-local character and resulting uncertainties in space resolution.
Electron-ion plasmas cover a huge area of different conditions, from dense to weak plasmas under collisionless or strongly collisional conditions. The ions can be hot or

[1] if the EEDF is Maxwellian. If it is not, the mean kinetic electron energy is obtained.

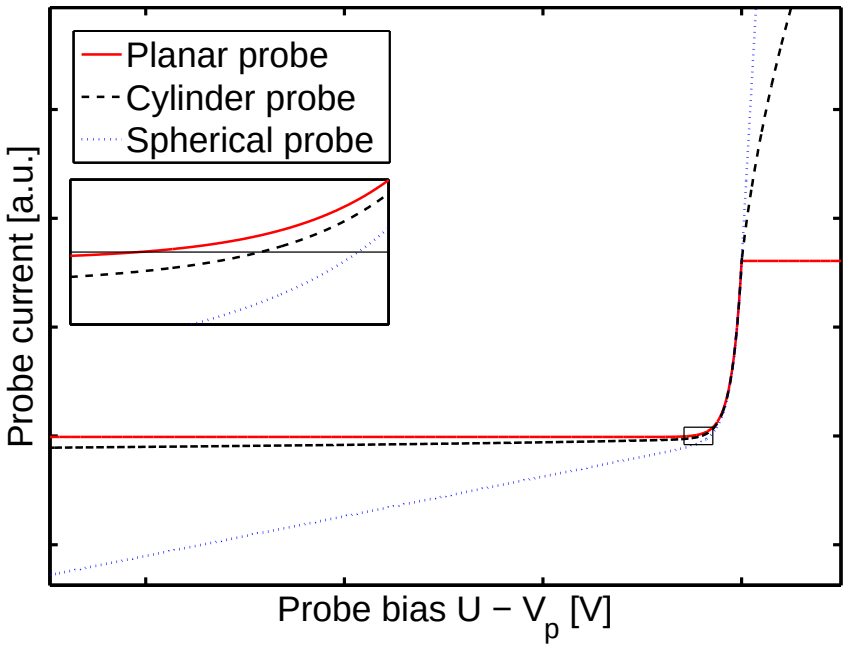

Figure 2.2.: A sketch of current-voltage characteristics for different probe geometries in the OML regime. For demonstration purposes the ion temperature is strongly exaggerated. At the plasma potential V_p a sharp knee occurs in the planar probe current. The insert shows a detail of the marked region where $I(U)$ intersects the U axis. Historically the negative current is drawn in Langmuir probe current-voltage plots.

cold, and can also be negatively charged. There also exist magnetized plasmas and different mechanisms of plasma ignition, and each condition requires specific probe design and data evaluation. The appearance of different probes and theories are, thus, very manifold and the amount of literature on this topic, covering nearly one century, is tremendous. Therefore, Langmuir probes are a topic in many textbooks and review papers [3, 4, 5]. A good introduction and further literature is found in [6].

In the present study in the experimental set-up PULVA-INP, low pressure conditions in an unmagnetized plasma are present, allowing for a relatively simple evaluation of the electron current which is not affected by collisions. During the measurement, a voltage ramp $U(t)$ is biased to the probe and the resulting current $I(t)$ between probe and surrounding plasma is determined and stored. Later, the current-voltage characteristics $I(U)$ are evaluated.

Fig. 2.2 shows theoretical $I(U)$ characteristics for different probe geometries in the OML regime for an electropositive plasma with a Maxwellian EEDF. Historically, the negative current is drawn in Langmuir probe plots. The characteristics can be divided into three regions: The region with positive bias with respect to V_p is called the “electron saturation region”. Here, the current is determined by elec-

trons only, since the (positive) ions are repelled. In analogy, the region with larger negative probe bias is called the "ion saturation region", because the electrons are repelled and the current is only determined by ions. However, due to the relatively high electron energy, a region exists where both electrons and ions can reach the probe. This region is called the "electron retarding region". For a Maxwellian EEDF, the electron current in this region is described by an exponential law which is connected to the electron energy.

For different probe geometries, different behavior can be observed. An ideal plane probe shows no bias dependence in the saturation regions. The plasma potential occurs as a sharp knee. By contrast, an ideal spherical probe does not show a knee, and the current shows a linear dependence on the probe bias in the saturation regions. For a cylindrical probe, this dependence is described by a root function. The reason for the different characteristics is a change of the effective probe surface with changing bias voltage, which is zero for an infinite plane area. The floating potential V_f is defined as the probe bias U where the probe current $I(U)$ vanishes

$$V_f := U(I = 0) \quad . \tag{2.14}$$

As a consequence from the difference in probe currents, also the floating potential is influenced by the probe geometry, as shown in the insert. At the plasma potential V_p the transition occurs from electron retarding to electron saturation region. For simplicity it is convenient to define V_p as the reference potential, i.e. $V_\mathrm{p} := 0$ in the following. In practice, V_p is obtained from the maximum in dI/dU or from the intersection of an extrapolation of electron retarding current and the saturation current. The third possibility is calculating V_p from the second derivative via

$$V_\mathrm{p} := U\left(\frac{d^2I}{dU^2} = 0\right) \quad . \tag{2.15}$$

This method is also used in the analysis of Langmuir probe data in the present work. The algorithm will be briefly explained in the following. For the calculation of the second derivative the probe characteristic is filtered by means of a Sawitzky Golay filter and a linear interpolation between data points is used.

For the analysis of the electron current $I_\mathrm{e}(U)$, first an analytical expression [7, 8, 9] is fitted to the ion saturation current to obtain a description for the ion current $I_\mathrm{i}(U)$. In the region with $U \ll V_f$, no electrons can reach the probe, and the ion current can be described by

$$I_\mathrm{i}(U) = \alpha_\mathrm{i} U^{\gamma_\mathrm{i}} \quad , \tag{2.16}$$

where α_i and γ_i are treated as free parameters. The electron current is then obtained by

$$I_\mathrm{e}(U) = I(U) - I_\mathrm{i}(U) \quad . \tag{2.17}$$

Assuming a Maxwellian EEDF, the electron temperature is computed from an exponential fit of the electron retarding current by

$$I_\mathrm{e}(U) = I_\mathrm{e}(V_\mathrm{p}) \exp\left\{\frac{U}{V_\mathrm{e}}\right\} \quad , \tag{2.18}$$

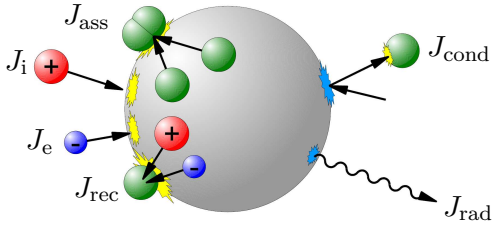

Figure 2.3.: Scheme of the energy flux densities between a micro-particle and the surrounding plasma environment. The particle gains energy from the kinetic energy of electrons and ions, from their recombination and from plasma specific processes like the association of atoms at the particle surface. Energy loss occurs via conduction and radiation.

and the electron density is calculated via

$$n_{\mathrm{e}} = \frac{I(V_{\mathrm{p}})}{A_{\mu}} \sqrt{\frac{2\pi m_{\mathrm{e}}}{e_0 V_{\mathrm{e}}}} \quad . \tag{2.19}$$

The assumption of a Maxwellian EEDF was ascertained to be a good approximation in a specific parameter range. This will be discussed in more detail in chapter 5.

2.3. Energy balance of substrates in a plasma environment

Micro-particles, confined in the sheath of a plasma, are exposed to multi-species bombardment from neutrals, radicals, electrons and ions as well as to electromagnetic plasma irradiation. The kinetic energy of the impinging electrons and ions, as well as their recombination energy, contributes to the heating of the particle surface. Furthermore - depending on the plasma environment - other processes like latent heat release of deposited material, exothermic reaction processes or association energy from recombination of dissociated molecules can account for the heating of the particle. Typically, due to its small heat capacity a micro-particle reaches a stable temperature T_{μ} within tens of milliseconds [10]. Then, the integral energy influx density J_{in} is balanced by integral energy loss density J_{out}

$$J_{\mathrm{in}} = J_{\mathrm{out}} \tag{2.20}$$

due to radiation and conduction to the environment [11, 12].

The contribution from plasma irradiation can be assumed to be negligible in typical rf discharges [12], and also the role of metastables, which has been benchmarked by Do et al. [13] to be in the order of some $\mu\mathrm{Wcm}^{-2}$, is insignificant. In the case of argon and argon-hydrogen plasmas, the integral energy influx density J_{in} can thus be described as

$$J_{\mathrm{in}} = J_{\mathrm{e}} + J_{\mathrm{i}} + J_{\mathrm{rec}} + J_{\mathrm{ass}} \quad , \tag{2.21}$$

where J_{e}, J_{i}, J_{rec} and J_{ass} denote the kinetic energy release density of electrons and ions and the energy influx densities due to recombination of charge carriers and

dissociated molecules, respectively. The energy influx is balanced by energy loss J_{out} due to radiation and conduction to the environment

$$J_{\mathrm{out}} = J_{\mathrm{rad}} + J_{\mathrm{cond}} \quad . \tag{2.22}$$

A scheme of the mentioned energy flux densities is sketched in fig. 2.3. Now the mentioned energy flux densities for particles in the sheath of an electropositive low-pressure rf-discharge will be quantified by a simple model.

The electron particle influx density j_{e} towards a retarding surface at a yet unknown floating potential V_f is described by

$$j_{\mathrm{e}} = \alpha \frac{1}{4} n_{\mathrm{e},0} \exp\left\{\frac{V_f}{V_{\mathrm{e}}}\right\} \sqrt{\frac{8 e_0 V_{\mathrm{e}}}{\pi m_{\mathrm{e}}}} \tag{2.23}$$

as deduced in eqn. (2.9), where $n_{\mathrm{e},0}$ is the electron density in the undisturbed (bulk) plasma, m_{e} the electron mass, $V_{\mathrm{e}} = k_{\mathrm{B}} T_{\mathrm{e}}/e_0$ the electron temperature in Volts, e_0 the elementary charge, T_{e} the electron temperature in K and k_{B} the Boltzmann constant. This description is valid for electrons with a Maxwellian EEDF. The exponential term describes the reduction in n_{e} due to repulsion from the negatively charged surface and the root describes the mean electron thermal velocity. The duty cycle is an approximation for the time-averaged electron density at a position z in the rf-sheath. In addition to the definition in eqn. (1.8), α also includes the electron sticking coefficient. However, α will be named 'electron duty cycle' in the following for simplicity. The kinetic energy influx density due to electrons is then

$$J_{\mathrm{e}} = j_{\mathrm{e}} \cdot 2 e_0 V_{\mathrm{e}} \quad . \tag{2.24}$$

The factor $2e_0V_{\mathrm{e}} = 2k_{\mathrm{B}}T_{\mathrm{e}}$ is the mean kinetic energy of the electrons arriving at the particle surface, which was identified in eqn. (2.13).

By contrast, for ions the particle is attractive, and the ion flux density j_{i} towards the particle is

$$j_{\mathrm{i}} = \eta\, n_{\mathrm{e},0} \exp\{-0.5\} \sqrt{\frac{e_0 V_{\mathrm{e}}}{m_{\mathrm{i}}}} \cdot \left(1 - 2\frac{V_f}{V_{\mathrm{e}}}\right)^{\beta} \quad , \tag{2.25}$$

where the root describes the ion's velocity, which approaches sound (Bohm) velocity v_{B} at the sheath edge, as deduced in eqn. (2.3). Here the ion density at the sheath edge is described via the bulk electron density times a reduction factor, which accounts for the attenuation of ion density due to acceleration of the ions to v_{B}, and m_{i} denotes the ion mass. For impinging ions, the particles are assumed to be perfect absorbers in this description. The factor η accounts for the area of a two-dimensional projection of the object, as seen by the streaming ions. For a sphere, $\eta = 1/4$, for an ideal cylinder $\eta = 1/\pi$ and for a planar object $\eta = 1$. Again, this equation is adopted from OML probe theory [1]. In the OM limit, also a geometric OML correction factor is necessary, given in the brackets, where β again depends on the geometry. For an ideal plane probe $\beta = 0$, whereas for a small micro-particle

$\beta = 1$. The kinetic energy influx density of ions is then given by

$$J_\mathrm{i} = -j_\mathrm{i} \cdot e_0 V_f \quad . \tag{2.26}$$

However, if the plasma consists of more than one kind of positive ions, e.g. in an argon-hydrogen mixture, the behavior of the different species has to be taken into account. In a multiple ion low pressure plasma with comparable ion densities $n_{\mathrm{i,k}}$, each species marked with an index k, enters the sheath with the bulk ion sound velocity [14]

$$v_\mathrm{B} = \sqrt{\frac{e_0 V_\mathrm{e}}{n_{\mathrm{e},0}} \sum_\mathrm{k} \frac{n_{\mathrm{i,0,k}}}{m_\mathrm{k}}} \quad , \tag{2.27}$$

and eqn. ((2.25)) has to be modified to

$$j_\mathrm{i} = \sum_\mathrm{k} j_{\mathrm{i,k}} = \eta \sum_\mathrm{k} n_{\mathrm{i,s,k}} v_\mathrm{B} \cdot \left(1 - 2\frac{V_f}{V_\mathrm{e}}\right)^\beta \quad . \tag{2.25a}$$

In this equation, $n_{\mathrm{i,s,k}}$ is the ion density of species k at the sheath edge.

After hitting the particle, the ion can recombine at the particle surface. As the particle is not connected to an external electrical circuit, the involved electron has been collected by the particle from the plasma before, and the net work function is zero. Assuming that the recombination energy $E_{\mathrm{ion,k}}$ is released to the particle, the energy influx density from recombination of a species k is

$$J_\mathrm{rec} = \sum_\mathrm{k} j_{\mathrm{i,k}} (E_{\mathrm{ion,k}} - E_{\mathrm{diss,k}}) \quad . \tag{2.28a}$$

When the ions are molecular, such as H_3^+ or ArH^+, some energy might be required for their dissociation into stable atoms or molecules, which is considered in the term $E_{\mathrm{diss,k}}$, and the ionization energy $E_{\mathrm{ion,k}}$ (see table 2.1) of the ion resulting from the dissociative reaction is released. In a pure noble gas discharge with one ion species, (2.28a) can simply be written as

$$J_\mathrm{rec} = j_\mathrm{e} E_\mathrm{ion} \quad , \tag{2.28}$$

and the easier accessible j_e can be utilized instead of j_i due to the floating condition.

Above the dissociation of molecular ions was mentioned. Dissociation of molecules in a plasma can also occur via electron neutral collisions. In low pressure plasmas the association process, where dissociated molecules recombine, most probably occurs on surfaces [15]. The released energy from this process often plays an important role for the energy balance. Assuming a Maxwellian speed distribution, the resulting energy flux density towards the particle can be estimated analogous to eqn. (2.23) [12]

$$J_\mathrm{ass} = \frac{1}{2}\Gamma_\mathrm{k} \frac{1}{4} n_\mathrm{k} \sqrt{\frac{8 k_\mathrm{B} T_\mathrm{gas}}{\pi m_\mathrm{k}}} E_{\mathrm{diss,k}} \quad . \tag{2.29}$$

In this equation, n_k is the number density of the dissociated gas species, 1/2 is the

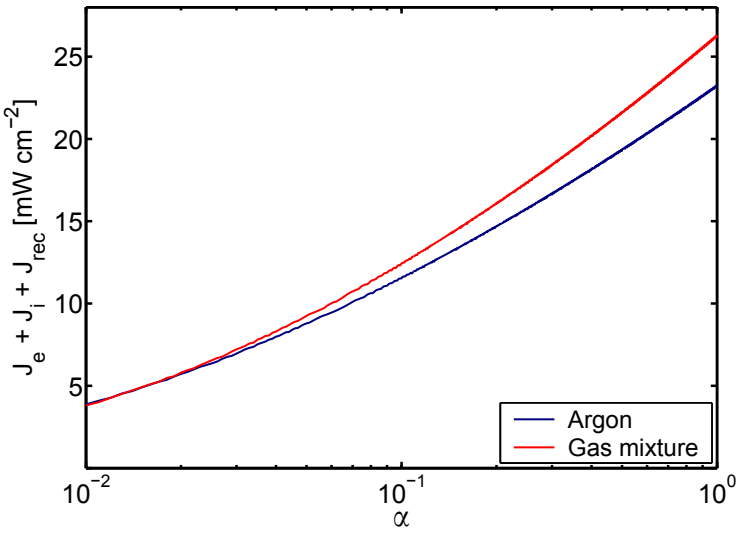

Figure 2.4.: Energy influx density towards a planar surface, facing towards the plasma volume due to the contribution of charge carriers, modeled for $V_e = 1$ eV and $n_{e,0} = 1 \cdot 10^{16}$ m^{-3} in argon as well as with an admixture of 10% hydrogen in dependence of the electron duty cycle α.

stoichiometric factor and the factor 1/4 accounts for the same geometric consideration as for the impinging electrons but without retarding potential. Γ_k is the association probability at the particle surface. For oxygen on melamine formaldehyde, it has been estimated to be in the order of $\Gamma_O \approx 0.05$. For hydrogen the probability is expected to be $0.1 \ll \Gamma_H \leq 1$.

The integral energy influx density towards the particles, described by (2.21), is thus determined by the plasma parameters, the electron duty cycle α, the gas mixture and occasionally by the release of energy at the surface due to association processes. Fig. 2.4 shows the dependence of the contribution of the sum of kinetic and potential energy of the impinging charge carriers to a plane area in dependence on α for a plasma with $V_e = 1$ eV and $n_{e,0} = 1 \cdot 10^{16}$ m^{-3}. Two cases are shown, the first one is an argon discharge and the second one a gas mixture of 90% argon

	Ar	H_2	H	ArH^+	H_3^+
m [u]	39.9	2.0	1.0	40.9	3.0
E_{ion} [eV]	15.76	15.37	13.60	-	-
E_{diss} [eV]	-	4.52	-	4.02	4.37
γ	5/3	7/5	5/3	7/5	8/6

Table 2.1.: Specific constants of the most important species in an Ar-H_2 plasma [16, 17, 18]. The dissociation energies of the ions refer to the reactions $H_3^+ \rightarrow H_2 + H^+$ and $ArH^+ \rightarrow Ar + H^+$, after [19, 20].

and 10% hydrogen. If the ion masses are comparable, J_i is weakly influenced by a change in the relative densities because v_B is not altered strongly. In an argon-hydrogen plasma, a drop in the relative fraction of the light ion population causes v_B to decrease. The contribution from kinetic ions to the integral energy influx is very small, moreover the ionization energies of different gases are often comparable. However, if v_B is changed also V_f is affected and and as a result also the J_e and J_rec are governed directly. The relative ion densities for the gas mixture in fig. 2.4 were taken from [21], where discharge conditions were modeled which are comparable to the experimental conditions discussed in chapter 4. However, the contribution J_ass is not shown in fig. 2.4.

In thermal equilibrium, J_in is balanced by energy loss and (2.22) is valid. The radiative energy loss density can be estimated from Stefan Boltzmann's law

$$J_\mathrm{rad} = \sigma \varepsilon_\mu \left(T_\mu^4 - T_\mathrm{env}^4 \right) \quad , \tag{2.30}$$

where T_μ and T_env are the temperatures of the particles and the inner walls of the plasma chamber, respectively, ε_μ is the emissivity of the particles and σ is the Stefan Boltzmann constant. The emissivity of the particles is estimated to be $\varepsilon = 0.5$. In the present setup the plasma may be optical dense in the center of some optical transitions but optical thin over nearly the whole spectrum. Thus, the absorption of thermal radiation during transmission of the plasma can be neglected. In low pressure conditions, the behavior of the gas molecules is described in the Knudsen regime [11, 12], where the energy loss density is linear in the gas pressure

$$J_\mathrm{cond} = p_\mathrm{gas} \frac{\gamma + 1}{16\,(\gamma - 1)} \alpha_\mu \sqrt{\frac{8 k_\mathrm{B}}{\pi m_\mathrm{gas} T_\mathrm{gas}}} \left(T_\mu - T_\mathrm{gas} \right) \quad . \tag{2.31}$$

The adiabatic coefficient $\gamma = c_\mathrm{p}/c_\mathrm{v}$ for different gases is listed in table 2.1. The accommodation coefficient of the particles is estimated to be $\alpha_\mu \approx 0.86$ [12, 22].

2.3.1. Self-consistent calculation of the floating potential

The floating potential, used in eqn. ((2.23)), is computed from $j_\mathrm{e} = j_\mathrm{i}$ by solving

$$0 = (1 - 2\chi)^\beta \, \eta \exp\left\{ -\frac{1}{2} \right\} \exp\left\{ -\chi \right\} \sqrt{\frac{2\pi m_\mathrm{e}}{m_\mathrm{i}}} - \alpha \tag{2.32}$$

where a normalization to the electron temperature is used

$$\chi := \frac{V_f}{V_\mathrm{e}} \quad .$$

Within an electropositive plasma, where $\alpha = 1$, the floating potential depends on the gas mass, the electron temperature and - in the OM limit - on the probe geometry. However, as the particles are confined inside the rf sheath where $\alpha \ll 1$ and $\eta \leq 1$, the floating potential is weaker. Fig. 2.5 shows the dependence of χ on α for a spherical particle in argon, as obtained from eq. (2.32). If more than one ion species is present, the valid expression for j_i has to be considered and eqn.

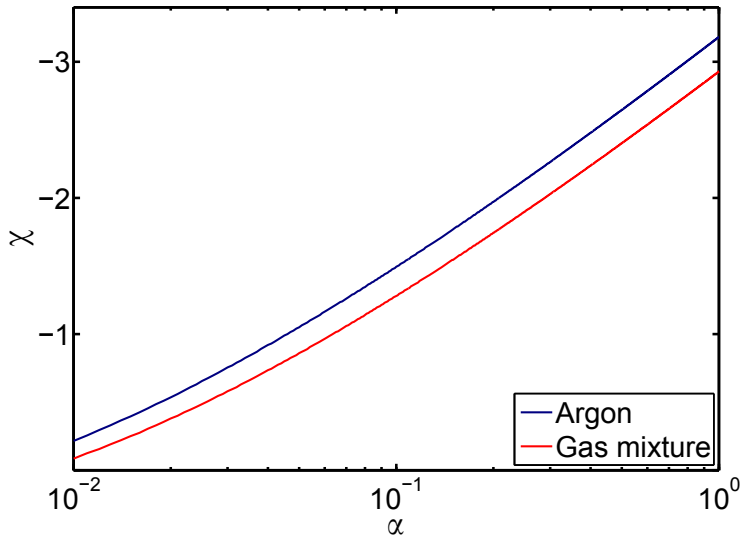

Figure 2.5.: The normalized floating potential χ of a planar surface, facing towards the plasma volume as a function of the electron duty cycle α for a spherical body in argon and an argon mixture with 10% hydrogen.

((2.32)) is modified to

$$0 = (1-2\chi)^{\beta}\,\eta\exp\{-\chi\}\sqrt{\frac{2\pi m_{\mathrm{e}}}{n_{\mathrm{e},0}^{3}}}\sqrt{\sum_{\mathrm{k}}\frac{n_{\mathrm{i},0,\mathrm{k}}}{m_{\mathrm{k}}}}\sum_{\mathrm{k}}n_{\mathrm{i,s,k}}-\alpha \quad . \tag{2.32a}$$

In fig. 2.5 the dependence of χ on α under the admixture of 10% hydrogen is shown, calculated by eqn. (2.32a). Elsewhere the floating potential for similar calculations has often been obtained by Langmuir probe measurements directly [12, 22, 23]. However, if the ion flow towards the Langmuir probe and the surface under consideration is different due to OM and geometric effects, this should be taken into account. Generally, the floating potential of a surface within the quasineutral plasma bulk strongly differs from that within the rf sheath.

2.4. Macroscopic bodies in a plasma environment

In contrast to micro-particles, a macroscopic body or substrate shows a different thermal response to the exposure to a plasma environment. The mechanisms of heating and cooling are in principle the same, but due to the large thermal inertia of the substrate it takes a long time (at least minutes) to reach an equilibrium temperature. Thus, the energy flux to the substrate can be determined by measuring its temperature change. This has first been utilized by Thornton [24] by attaching a temperature sensor to a dummy substrate, which was exposed to a plasma. These so-called calorimetric probes, sometimes also referred to as thermal probes, are an active field of recent research [23, 25, 26, 27], used for the determination of energy

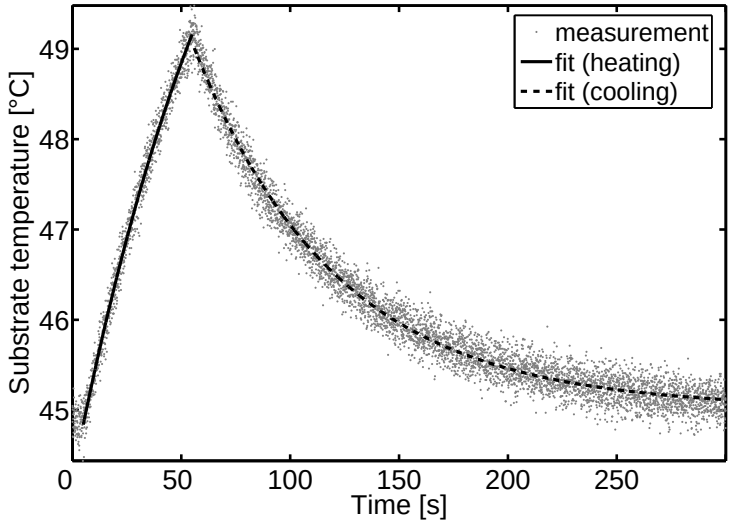

Figure 2.6.: Temporal evolution of the substrate temperature in response to a plasma exposure of approximately 55 s duration. The heating and cooling of the substrate can be described by an exponential law.

fluxes between plasma and surfaces. This is of interest in many technical and industrial applications as mentioned in the introduction of this thesis. An example of a typical measurement curve is given in fig. 2.6. The net energy influx to the substrate can be written in terms of the change in substrate temperature [24]

$$P_{\mathrm{in}} - P_{\mathrm{out}} = C_{\mathrm{S}} \cdot [\dot{T}]_{\mathrm{heat}}, \tag{2.33}$$

where C_{S} is the effective heat capacity of the probe which has to be measured, and $P_{\mathrm{in}} = J_{\mathrm{in}} \cdot A$ is the power deposited on the substrate with area A. Details on the calibration of a probe can be found elsewhere [27].

During exposure to the plasma, also power P_{out} is lost due to radiation, convection and conduction to the substrate holder and the gas. When the energy input from the plasma is interrupted by switching off the plasma, the substrate cools down, and the power balance reads as

$$P_{\mathrm{out}} = C_{\mathrm{S}} \cdot [\dot{T}]_{\mathrm{cool}} \quad . \tag{2.34}$$

Connecting equation 2.33 and 2.34 leads to

$$P_{\mathrm{in}} = C_{\mathrm{S}} \cdot [\dot{T}_{\mathrm{heat}} - \dot{T}_{\mathrm{cool}}] \quad , \tag{2.35}$$

which describes the total or integral energy flux to a substrate. Thus, the total energy in- and outflux can be determined directly by the temporal behavior of the surface temperature in response to a plasma pulse. Additionally, further information on the composition of the total energy input can be obtained by applying a bias voltage to the substrate [25, 26].

Bibliography

[1] J. E. Allen: *Probe theory - the orbital motion approach.* Phys. Scripta **45** (5), pp. 497–503 (1992). See page: 17, 26

[2] J. Reece Roth: *Industrial Plasma Engineering*, volume 1. IOP publishing, Bristol and Philadelphia (1995). See page: 22

[3] R. Hippler, H. Kersten, M. Schmidt and K. H. Schoenbach (eds.): *Low Temperature Plasmas, 2nd revised and enlarged edition.* Wiley-VCH, Weinheim (2008). See page: 23

[4] M. A. Lieberman and A. J. Lichtenberg: *Principles of Plasma Discharges and Materials Processing.* John Wiley and Sons, Inc., New York (1994). See page: 23

[5] A. Piel: *Plasma Physics.* Springer Verlag Berlin Heidelberg (2010). See page: 23

[6] R. L. Merlino: *Understanding Langmuir probe current-voltage characteristics.* Am. J. Phys. **75** (12), pp. 1078–1085 (2007). See page: 23

[7] A. Karamcheti and C. Steinbrüchel: *Parametrization of Laframboise's results for spherical and cylindrical Langmuir probes.* J. Vac. Sci. Technol. A **17** (5), pp. 3051–3056 (1999). See page: 24

[8] G. Narasimhan and C. Steinbrüchel: *Analysis of Langmuir probe data: Analytical parametrization, and the importance of the end effect.* J. Vac. Sci. Technol. A **19** (1), pp. 376–378 (2001). See page: 24

[9] C. Steinbrüchel: *A new method for analyzing Langmuir probe data and the determination of ion densities and etch yields in an etching plasma.* J. Vac. Sci. Technol. A **8** (3), pp. 1663–1667 (1990). See page: 24

[10] J. E. Daugherty and D. B. Graves: *Particulate temperature in radio frequency glow discharges.* J. Vac. Sci. Technol. A **11** (4), pp. 1126–1131 (1993). See page: 25

[11] E. Stoffels, W. W. Stoffels, H. Kersten, G. H. P. M. Swinkels and G. M. W. Kroesen: *Surface processes of dust particles in low pressure plasmas.* Phys. Scripta **2001** (T89), p. 168 (2001). See page: 25, 29

[12] G. Swinkels, H. Kersten, H. Deutsch and G. M. W. Kroesen: *Microcalorimetry of dust particles in a radio-frequency plasma.* J. Appl. Phys. **88** (4), pp. 1747 – 1755 (2000). See page: 25, 27, 29, 30

[13] H. T. Do, H. Kersten and R. Hippler: *Interaction of injected dust particles with metastable neon atoms in a radio frequency plasma.* New J. Phys. **10** (5), p. 053010 (2008). See page: 25

[14] D. Lee, L. Oksuz and N. Hershkowitz: *Exact Solution for the Generalized Bohm Criterion in a Two-Ion-Species Plasma.* Phys. Rev. Lett. **99** (15), p. 155004 (2007). See page: 27

[15] A. V. Pipa: *On Determination of the Degree of Dissociation of Hydrogen in Non-Equillibrium Plasmas by Means of Emission Spectroscopy.* Logos, Berlin (2004). PhD thesis, EMAU Greifswald (1999). See page: 27

[16] W. Bleakney: *The Ionization Potential of Molecular Hydrogen.* Phys. Rev. **40** (4), pp. 496–501 (1932). See page: 28, 81

[17] Darwent, B. deB.: *Bond Dissociation Energies in Simple Molecules.* (1970). See page: 28, 81

[18] Y. Ralchenko, A. Kramida, J. Reader and N. A. Team: *NIST Atomic Specta Database.* NIST Atomic Spectra Database (version 3.1.5), [Online], (2008). See page: 28, 81

[19] P. C. Cosby and H. Helm: *Experimental determination of the H3+ bond dissociation energy.* Chemical Physics Letters **152** (1), pp. 71 – 74 (1988). See page: 28, 81

[20] J. Lorenzen, H. Hotop, M. W. Ruf and H. Morgner: *Rovibronic structure in the electron energy spectrum for associative ionization: Ne(3P2), Ar(3P2)+H.* Zeitschrift fuer Physik A Hadrons and Nuclei **297** (1), pp. 19 – 23 (1980). See page: 28, 81

[21] E. Neyts, M. Yan, A. Bogaerts and R. Gijbels: *Particle-in-cell/Monte Carlo simulations of a low-pressure capacitively coupled radio-frequency discharge: Effect of adding H_2 to an Ar discharge.* J. Appl. Phys. **93** (9), pp. 5025–5033 (2003). See page: 29

[22] G. Swinkels: *Optical studies of micron-sized particles immersed in a plasma.* PhD Thesis, TU Eindhoven (1999) (1999). See page: 29, 30

[23] A.-L. Thomann, N. Semmar, R. Dussart, J. Mathias and V. Lang: *Diagnostic system for plasma/surface energy transfer characterization.* Rev. Sci. Instrum. **77** (3), 033501 (2006). See page: 30

[24] J. A. Thornton: *Substrate heating in cylindrical magnetron sputtering sources.* Thin Solid Films **54** (1), pp. 23 – 31 (1978). See page: 30, 31

[25] H. Kersten, D. Rohde, H. Steffen, H. Deutsch, R. Hippler, G. H. P. M. Swinkels and G. M. W. Kroesen: *On the determination of energy fluxes at plasma-surface processes.* Appl. Phys. A Mater.: **72**, pp. 531–540 (2001). See page: 30, 31

[26] D. Lundin, M. Stahl, H. Kersten and U. Helmersson: *Energy flux measurements in high power impulse magnetron sputtering.* J. Phys. D Appl. Phys. **42** (18), p. 185202 (7pp) (2009). See page: 30, 31

[27] M. Stahl, T. Trottenberg and H. Kersten: *A calorimetric probe for plasma diagnostics*. Rev. Sci. Instrum. **81** (2), 023504 (2010). See page: 30, 31

3. Thermographic phosphors

For the determination of the particle temperatures in the plasma, a non-invasive technique for a temperature measurement is required. A promising possibility is to utilize the effect of temperature on luminescent materials [1, 2, 3]. In this chapter, a short summary on luminescence and the influence of temperature to certain solid phosphors is given. The focus will be on a specific class of phosphors and some benchmark results are presented which lead to the choice of the phosphor utilized in the experiments. I want to emphasize that my choice is just a subjective decision, based on specific provisional instrumentation and a limited amount of phosphor samples.

3.1. Luminescence

Luminescent materials convert certain types of energy into non-thermal electromagnetic radiation [4]. Apart from reflection one may distinguish the emission processes of electromagnetic radiation from a solid by the terms incandescence (thermal radiation) and luminescence (non-thermal radiation). The latter process involves the optical transition of an electron from an excited state to a lower one, accompanied by the emission of a photon. There are different types of luminescence, e.g. photoluminescence, cathodoluminescence, thermoluminescence, chemiluminescence and more, which vary in the mechanisms of luminescence excitation. Here the focus will be on photoluminescence, which means the conversion of electromagnetic radiation.

Luminescent emission is not occurring instantly with excitation, but always continuing for a certain time interval after the initial exciting radiation is switched off. This so-called afterglow may be in the order of picoseconds or up to milliseconds

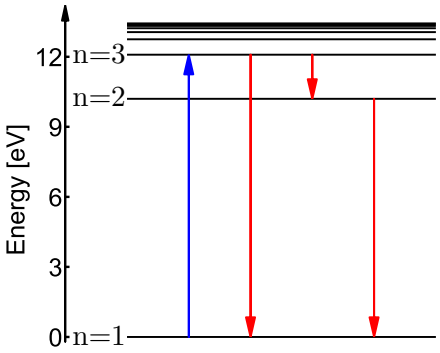

Figure 3.1.: Energy levels of the hydrogen atom and the possibilities of fluorescent emission after excitation to $n = 3$.

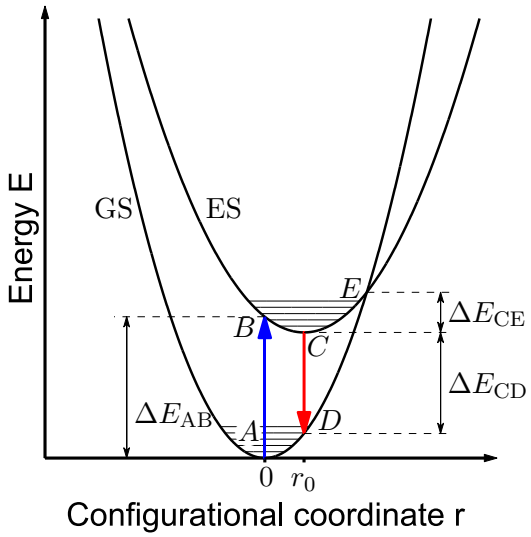

Figure 3.2.: Configurational coordinate diagram for an activator ion in a solid. Shown is the path of excitation and emission between ground state GS and an excited state ES, and the role of vibrational levels.

or even seconds. Historically, luminescent phenomena are divided into short emission (fluorescence) and long emission (phosphorescence), but this classification is not strictly valid anymore. Today, the term 'phosphorescence' is often used to describe processes where forbidden optical transitions are included, e.g. if the excited electron is trapped in a metastable state before the luminescent emission occurs.

Consider the most simple photoluminescent system: A hydrogen atom. An energy level diagram is shown in fig. 3.1. If the atom is in ground state (n = 1, with the principal quantum number n) and absorbs a photon of 102.5 nm wavelength, its electron will be lifted to the second excited state (n = 3). From this state it may either relax directly to the ground state (n $\rightarrow$ 1) under re-emission of 102.5 nm radiation (Lyman-β), or via the first excited state (n $\rightarrow$ 2 $\rightarrow$ 1) emitting 626.3 nm (Balmer-α) and subsequently 121.6 nm radiation (Lyman-α).

3.2. The influence of temperature on phosphor materials

There is a large arsenal of different photoluminescent materials, ranging from organic dyes to semiconductors and isolators doped and co-doped with sensitiver and activator ions providing luminescent properties. If the luminescent material under consideration is localized as a single ion or as group of ions in a solid, which is the case for most phosphor materials, for an appropriate description of the optical transitions often the 'configurational coordinate diagram' is used [4, 5]. In this simplified picture the energetic potential curves of the ground and excited states at the localized center are sketched as function of their spatial coordinate. This diagram is able to qualitatively explain a number of frequent observations such as Stokes shift, line broadening or thermal quenching.

For example, fig. 3.2 shows a configurational coordinate diagram of a ground state (GS) and an excited state (ES). The ES is shifted in its equilibrium position due to interaction with a neighboring ion by $\Delta r = |r_0|$, since its interaction to the neighbor ions is stronger than that of the ground state. Optical transitions are shown as vertical arrows in fig. 3.2. This implies the Franck Condon principle in which optical transitions can be assumed to appear instantly, compared to the movement of the heavy nucleus.
At a temperature of 0 K, only optical excitation into point B occurs from the equilibrium position $r = 0$ within the ground state. From the vibrational level at the excited state, the vibrational relaxation time is some orders of magnitudes smaller than the time constant for optical transitions [5], so the electron will relax into the equilibrium position r_0 in point C. From there, optical transition towards D occurs, followed again by vibrational relaxation to the equilibrium position of the ground state. From this path it is obvious that the energy ΔE_{AB} is larger than ΔE_{CD} because of energy losses in vibrational relaxation, and hence the stoke shift occurs.

If the system is at finite temperatures, optical transitions can also originate from vibrational levels and the energy gaps can differ from ΔE_{AB} and ΔE_{CD}. This results in a widening of the spectral lines. When the vibrational levels are occupied, also the possibility for an electron to overcome the energy barrier ΔE_{CE} is given. In point E, the ground and excited states intersect and excitation can be quenched without emitting radiation. As the optical emission is competing against thermal quenching, its intensity and decay time are influenced by the quenching rate and, thus, by temperature. On the other hand, consider GS to be another excited state from which emissive transition to a ground state occurs. In this case, quenching from ES to GS would enhance the optical transition from GS to the ground state.

3.3. Thermographic phosphors

Among the various principal phosphor materials, in particular the trivalent rare earth (RE^{3+}) ions have been investigated for the applicability in temperature-sensoring instrumentations due to their high quenching temperature and their emission characteristics [6, 7, 8]. They have been used for temperature measurements in combustion engines [9], in aerodynamic model testing [10] or in optical fibers [8]. As a measure for temperature, different characteristics are utilized, in emission (rise time, decay time, line ratios [6, 8]) as well as in absorption (differential excitation [11]) depending on respective conditions and demands.

The RE ions are characterized by an incompletely filled $4f$ electron shell. This shell is located inside the ion and is shielded from the environment by the outer $5s^2$ and $5d^6$ electrons. The influence of the crystal field on optical $f - f$ transitions is therefore small resulting in a small offset Δr and line-type emission. In the absorption spectrum two types of interconfigurational optical transitions are observed [4]: $4f^n \rightarrow 4f^{n-1}5d$ transitions within the RE ion and so-called charge-transfer

(CT) transitions $(RE)4f^n \rightarrow (RE)4f^{n+1}A^{-1}$ where an electron is transfered from a surrounding anion A [4, 5]. Both processes appear in the uv region and offer very efficient quantum yield in suitable host materials.

3.4. The fluorescent method for temperature measurement of micro-particles in a plasma

For the evaluation of the phosphor temperature, different temperature-dependent features are available offering certain advantages and disadvantages for the experimental configuration, the measurement accuracy and the accessible temperature range. In this section possible features are discussed with respect to their setup requirements and feasibility for measurements in a plasma.

Experimental studies on the temperature of micro-particles in plasmas have been performed only by few authors before. Oliver and Enikov measured the incandescent radiation from particles in a plasma jet [12] which only occurs at rather high particle temperatures above $T_\mu = 1000$ K. However, in a low pressure rf-discharge one would expect $T_\mu \approx 300 \ldots 400$ K.

Daugherty and Graves measured the temperature-dependent decay-time of manganese activated magnesium fluorogermanate (Mg_4FGeO_6:Mn) particles in a pulsed argon discharge during the plasma-off phase [13]. They reported particle temperatures of $T_\mu = 410 \pm 10$ K at an rf power of $P_{\mathrm{rf}} = 50$ W and a pressure of $p_{\mathrm{Ar}} = 20$ Pa in front of the water-cooled ground electrode. The decay time τ was approximately $\tau = 2$ ms at this temperature. The requirements for this type of measurements are

1A: Pulsed plasma mode or suitable pulsed excitation source (probably uv)

1B: Wavelength-selective system, ICCD[1] triggered with variable delay or with a time resolution better than 10 kHz.

1C: Suitable optics to detect the particle luminescence in the plasma with appropriate intensity even in the luminescence afterglow.

1D: During the measurement of one decay curve the amount of observed phosphor and its illumination intensity should be constant.

Point **1D** can be assumed to be satisfied during one typical afterglow cycle of some ms as the characteristic frequency of the motion of charged dust grains in the plasma appears in the order of some ten Hertz. However, if the luminescence decay is measured from multiple cycles, e.g. with variation of the time delay between luminescence excitation and detector exposure, it should be ascertained that the particles are confined properly.
Swinkels et al. utilized Rhodamine-B dyed melamine-formaldehyde (MF) particles and compared their temperature-dependent emission spectrum in the plasma to spectra obtained in a calibration oven [14, 15]. They reported temperatures of

[1] ICCD - Intensified Charge Coupled Device. Before the photons enter the photo sensitive layer, they are intensified by a photomultiplier. This photomultiplier also can act as a quick shutter, enabling high time resolution.

$T_\mu = 460 \pm 10$ K in $P_{\mathrm{rf}} = 50$ W and $p_{\mathrm{Ar}} = 20$ Pa in front of the driven electrode. For this type of measurement, the requirements are

2A: External excitation source (probably uv), which can be blocked for background subtraction

2B: Spectrograph and suitable CCD camera. If long exposure times are possible conventional CCDs are the best choice.

2C: Suitable optics to detect the particle luminescence with appropriate intensity in the presence of plasma emission.

2D: No requirements are demanded on stability of illumination intensity and the amount of observed material during one measurement.

Furthermore, for some phosphors strong changes in the excitation spectrum with increasing temperature have been reported [11, 16]. No application of this feature for particle temperature measurements is known to the author yet. The demands on this kind of measurements are

3A: At least two external excitation sources with capable wavelengths which can be blocked for background subtraction

3B: Observation of emission not necessarily with spectral resolution

3C: Suitable optics to detect the particle luminescence with appropriate intensity with respect to plasma emission.

3D: The amount of observed material should be constant through one measurement. Also the intensities of the illumination sources should be highly reproducible.

Of course, besides the ability to be confined in the plasma sheath, the emission intensity of the phosphor grains is a crucial parameter for temperature measurements due to the presence of additional plasma emission. Thus, the the optical transition(s) under consideration should be very intense and separable from dominant plasma lines. The sortiment of investigated phosphors was limited, and the choice was influenced by the optical characteristics of the available excitation sources, the optics and the detection system. Excitation measurements have been performed using a light source and a monochromator as shown in fig. 3.3, which was used to select the excitation wavelength. In the uv region transmission was rather poor but, nevertheless, transmission was still possible below 300 nm. For a more complete search the use of a calibrated luminescence spectrometer would be necessary.

However, the brightest phosphors in the available sortiment have formerly been developed for fluorescent lamps and are, thus, optimized for the excitation from Hg sources. Moreover, the spectral region for light transmission in air and optical components is limited towards the high energy end. One can find a general law in optics: The shorter the wavelength the lower are the transmission characteristics of windows, filters and lenses, the faster optical layers are destroyed by the uv

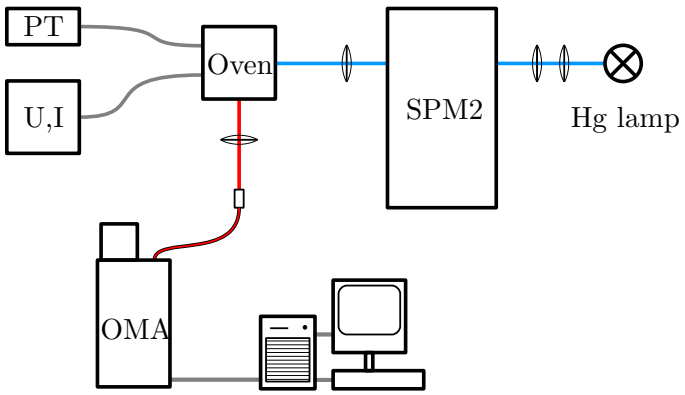

Figure 3.3.: Experimental setup for the characterization of phosphor samples. A certain wavelength from the emission spectrum of a high pressure Hg vapor lamp is selected by a monochromator (SPM2) and focused onto the phosphor sample, placed inside an oven. The temperature inside the oven is monitored via a temperature sensor (PT), the temperature is adjusted by changing the heating current provided by a power supply (U,I). Phosphor emission is collected and guided to a spectrograph with an intensified CCD camera (OMA).

radiation itself and the more expensive the components are. The same holds for organic dyes that are used in dye lasers at shorter wavelength. Thus, focusing to the wavelength region above 300 nm is justified not only from the technological point of view.

Fig. 3.4 shows the dominant emission of some promising phosphors at different temperatures. These measurements have been performed with the phosphor placed on an object holder inside a special calibration oven, as shown in fig. 3.3. Excitation was provided by a mercury lamp followed by a monochromator (Carl Zeiss SPM2) for wavelength selection. The emission spectra were detected by a 500 mm spectrograph (ACTON SpectraPro 2500 i) and an ICCD camera (Andor IStar), and the temperature inside the oven was measured by a PT 1000 temperature sensor.

Especially in the YVO_4 hosts, temperature-dependent emission features at the shown transitions occur. These transitions were excited at 313 nm, while the Y_2O_3 phosphor was excited by 264 nm. However, the most intense emission was observed from YVO_4:Eu.

The temperature features in the excitation spectrum of YVO_4:Eu, which have been published in [11] and could be verified qualitatively, are easily accessible from excitation in the near uv region. Furthermore, YVO_4:Eu showed very bright emission and also strong temperature-dependent effects in the emission spectrum, as shown in fig. 3.4. Besides some line broadening and shifting especially the change in the intensity ratio of the emission at 616.5 nm and 619.4 nm is evident. The mentioned pronounced temperature-dependent features in excitation and emission, together with the brightness of YVO_4:Eu are the reasons for the decision to use this phosphor for the temperature measurements.

The emission lines, dominating in fig. 3.4, belong to the transition $4f^5D_0 \rightarrow$

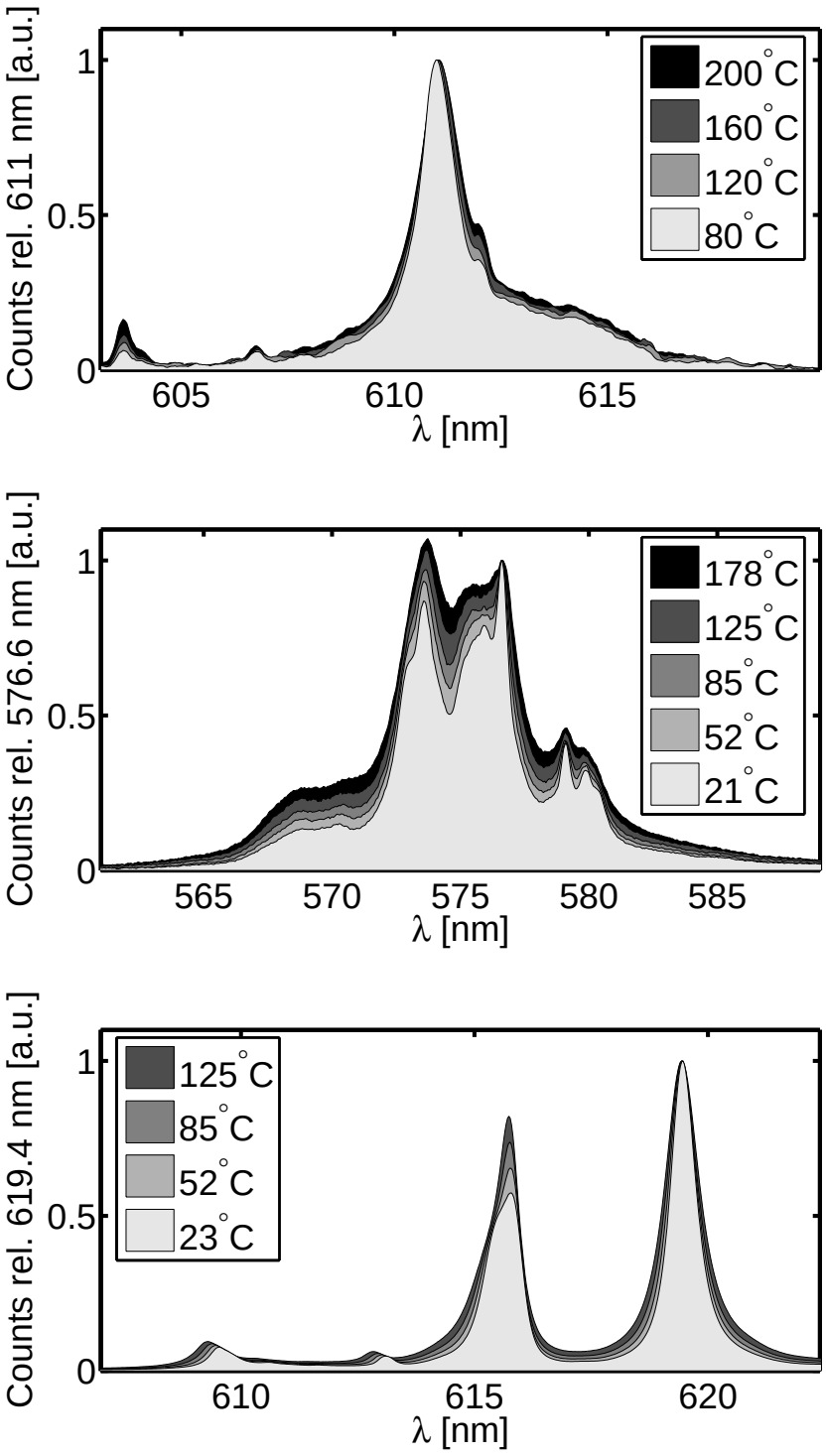

Figure 3.4.: Emission of three phosphor samples at different temperatures - from top to bottom: Y_2O_3:Eu, YVO_4:Dy, YVO_4:Eu. Emission intensity is normalized to the maximum of a well-defined emission peak.

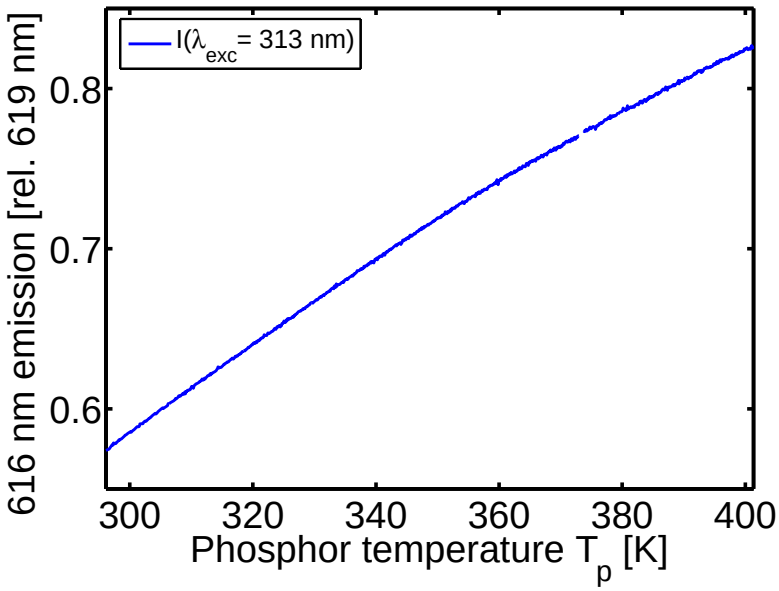

Figure 3.5.: Emission intensity of the 616.5 nm line of YVO_4:Eu, normalized to that of the 619.4 nm line (taken at the maxima). The measurements are shown for an excitation wavelength of $\lambda_{exc} = 313$ nm. The points are well reproducible.

$f4^7F_2$ of Eu^{3+}, which is split by the crystal field of the surrounding oxygen atoms. In fig. 3.5, the ratio of these lines is shown as a function of temperature. The measurements have been performed using interference filters instead of the monochromator, slowly increasing the temperature. This ratio turned out to approach a value of 1 with increasing temperature for the used phosphor sample (of course this can differ from sample to sample, because it also depends on different factors due to the production of the individual sample). The ratio of the mentioned lines was highly reproducible. Moreover, line broadening and shifting with temperature also depend on the temperature.

In contrast, fig. 3.6 shows the temperature-dependent ratio of 619.4 nm emission at 365 nm excitation to that at 313 nm emission, which has been obtained from the same measurements as fig. 3.5. Especially in a temperature range between 100° C and 200° C this ratio is strongly temperature-dependent and the emission intensities are comparable. However, in fig. 3.6 from the pronounced jump it is clearly obvious where the measurement have been paused. This can be explained by the following reasons:

- There was a discontinuity in the temperature of the Hg excitation source even after warming up, changing the emission spectrum of the lamp.
- The electrodes in the lamp were sputtered, changing the emission spectrum. This might appear quickly in new lamps, when the electrodes are shaped cone-like.
- The optical layers, used for filtering the lamp spectrum, were degraded during

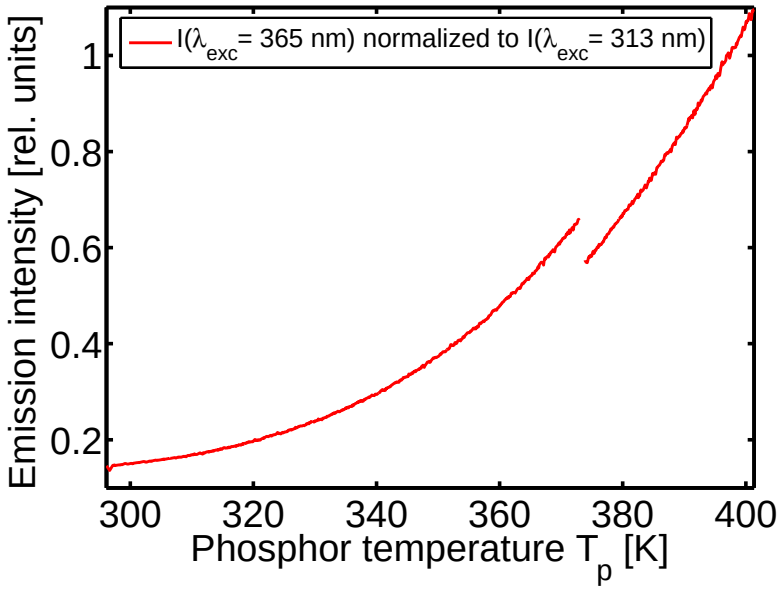

Figure 3.6.: Emission intensity (619.4 nm peak of YVO_4:Eu) under 365 nm excitation, normalized to emission at 313 nm excitation. In the region from room temperature to 350° C this ratio is monotonically increasing and very sensitive. However, as the jump at 373 K reveals the reproducability under the experimental conditions (see text) is poor.

the measurement by uv and temperature effects. In retrospect this is surely the case, as one set of filters was nearly useless after a couple of experiments.

Hence, the mentioned reasons which are expected to contribute to the jump in fig. 3.6 show that the requirement **3D** is not fulfilled in the present setup. Maybe monitoring the excitation intensity would be an option and this method could be interesting for higher temperatures. However, close to room temperature the quantum yield at 365 nm is comparably low and the phosphor emission is hidden behind intense plasma emission lines.
From this observations it can be concluded that temperature measurement using luminescent properties of small phosphor grains, which are confined in a plasma, are most likely based on emission characteristics. By observing line shifts, line broadening or relative intensities the influence by fluctuations in the spectrum of the excitation source or by variation in the amount of observed particles is only small. Among the considered possibilities, this technique is the most robust one and is chosen for the following temperature measurements. A more detailed description of the applied technique is given in the experimental section.

Bibliography

[1] L. P. Goss, A. A. Smith and M. E. Post: *Surface thermometry by laser-induced fluorescence.* Rev. Sci. Instrum. **60** (12), pp. 3702–3706 (1989). See page: 35

[2] H. Kusama, O. J. Sovers and T. Yoshioka: *Line Shift Method for Phosphor Temperature-Measurements.*
Jpn. J. Appl. Phys. **15** (12), pp. 2349–2358 (1976). See page: 35

[3] C. W. Struck and W. H. Fonger: *Thermal Quenching of Tb^{+3}, Tm^{+3}, Pr^{+3}, and Dy^{+3} $4f^n$ Emitting States in La_2O_2S.*
J. Appl. Phys. **42** (11), pp. 4515–4516 (1971). See page: 35

[4] G. Blasse and B. C. Grabmayer: *Luminescent Materials.* Springer (1994). See page: 35, 36, 37, 38

[5] S. Shionoya and W. M. Yen (eds.): *Phosphor Handbook.* CRC Press LLC. (1999). See page: 36, 37, 38

[6] S. W. Allison and G. T. Gillies: *Remote thermometry with thermographic phosphors: Instrumentation and applications.*
Rev. Sci. Instr. **68** (7), pp. 2615–2650 (1997). See page: 37

[7] P. R. N. Childs, J. R. Greenwood and C. A. Long: *Review of temperature measurement.* Rev. Sci. Instrum. **71** (8), pp. 2959–2978 (2000). See page: 37

[8] S. A. Wade, S. F. Collins and G. W. Baxter: *Fluorescence intensity ratio technique for optical fiber point temperature sensing.*
J. Appl. Phys. **94** (8), pp. 4743–4756 (2003). See page: 37

[9] J. P. Feist and A. L. Heyes: *The characterization of Y2O2S : Sm powder as a thermographic phosphor for high temperature applications.*
Meas. Sci. Technol. **11** (7), pp. 942–947 (2000). See page: 37

[10] K. Tobin, G. Capps, J. Muhs, D. Smith and M. Cates: *Dynamic high-temperature-phosphor thermometry.*
Technical Report ORNL/ATD–40, Oak Ridge National Lab., TN (USA); Applied Technology Div. (1990). Technical report. See page: 37

[11] A. Bugos, D. Beshears, M. Cates and S. Allison: *Emission properties of phosphors for high temperature sensor applications.*
In *Southeastcon 1988 ;IEEE Conference Proceedings*, pp. 228–233 (1988).
See page: 37, 39, 40

[12] D. Oliver and R. Enikov: *Micro-particles temperature measurements in a plasma jet.* Vacuum **58** (2-3), pp. 244 – 249 (2000). See page: 38

[13] J. E. Daugherty and D. B. Graves: *Particulate temperature in radio frequency glow discharges.*
J. Vac. Sci. Technol. A **11** (4), pp. 1126–1131 (1993). See page: 38

[14] G. Swinkels: *Optical studies of micron-sized particles immersed in a plasma.*
PhD Thesis, TU Eindhoven (1999) (1999). See page: 38

[15] G. Swinkels, H. Kersten, H. Deutsch and G. M. W. Kroesen: *Microcalorimetry of dust particles in a radio-frequency plasma.*
J. Appl. Phys. **88** (4), pp. 1747 – 1755 (2000). See page: 38

[16] W. Turley, C. Iverson, S. Lutz, R. Flurer, J. Schaub, S. Allison, J. Ladish and S. Caldwell: *A fiber optic detection system for determination of an infrared beam spectrum in an adverse environment.*
In *Proceedings, SPIE, Vol. 1172* (1989). See page: 39

4. Experimental work

4.1. Experimental Setup

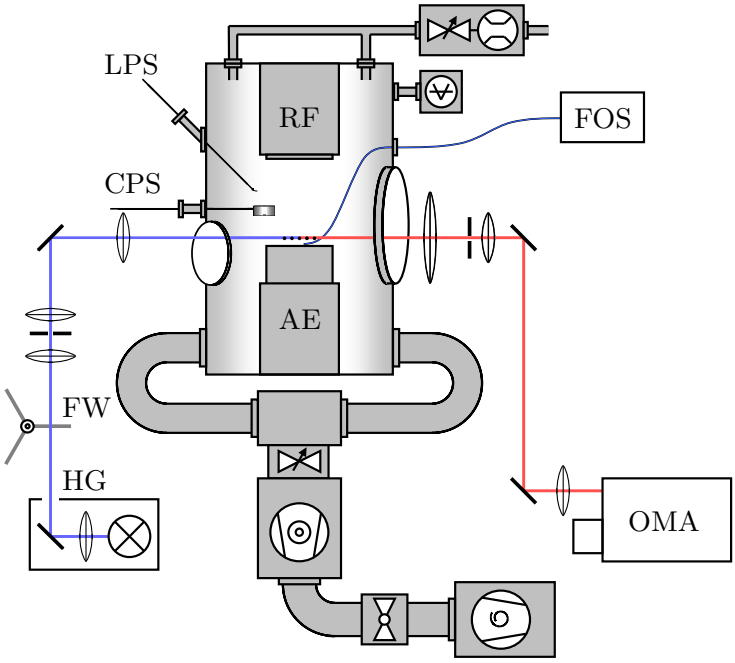

Figure 4.1.: Scheme of PULVA-INP and the experimental setup: RF - driven electrode, AE - Adaptive Electrode. For the Langmuir and calorimetric probe measurements: LPS - Langmuir probe system, CPS - calorimetric probe system. For the particle temperature measurements: OMA - optical multichannel analyzer, FOS - fiber optical system, FW - filter wheel, HG - mercury arc lamp.

Fig. 4.1 shows a sketch of the experimental setup PULVA-INP. This experiment was particularly designed for the confinement and manipulation of micro-particles [1], and for the excitation and observation of luminescence of confined phosphor particulates. The diagnostics shown in fig. 4.1 were not all used simultaneously, but successively under identical plasma conditions.

The device, shown in fig. 4.2(a) as a photograph, consists of a vessel of approximately 70 liters volume which is evacuated by a turbomolecular pump (Pfeiffer Vacuum TPH 521 PC) and a scroll pump (Varian Tri Scroll 600). Between pumps and vessel, a butterfly valve with a stepper motor (VAT Series 14) allows to alter the effective exhaustion rate. The gas feed can be adjusted by digital mass

(a) PULVA-INP in action. Inside the window, an argon plasma (pink) can be seen.

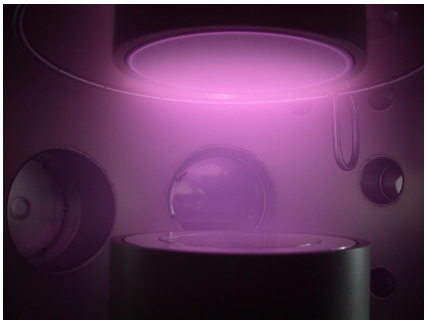

(b) The rf-driven electrode is located at the top, the Adaptive Electrode (AE) at the bottom.

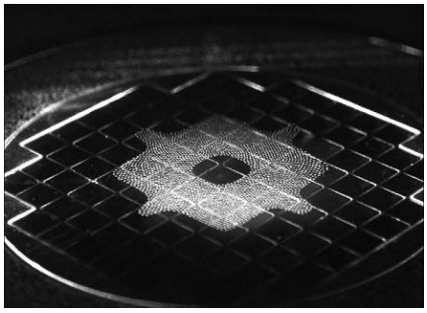

(c) Melamine-Formaldehyde particles of approximately 10 μm in diameter, confined in front of the AE (see text).

Figure 4.2: Photographs of the experiment PULVA-INP, located at the Institute for Plasma Science and Technology e.V. (INP) in Greifswald, Germany.

flow controllers (MKS 1179 B). The gas pressure is monitored by a Baratron gauge (MKS Type 626) which measures the pressure independently of the gas species. All pumps, controllers and valves are controlled by a personal computer.

Because turbomolecular pumps provide different exhaustion rates for different gases, especially for hydrogen containing mixtures a non-linear dependence of the partial pressure ratio on the gas flow ratio is expected.

For a calibration, different gas mixtures at $p_{gas} = 10$ Pa and a total gas flow of 20 sccm were generated and the position of the VAT valve were taken. Afterwards, the conditions were reproduced with only one gas component using the positions of the valve as noted before, and the partial pressures were measured. In an ideal gas mixture, the total gas pressure p_{gas} is the sum of the partial gas pressures as formulated in the Dalton law, e.g.

$$p_{gas} = p_{Ar} + p_{H2} + p_{N2} \tag{4.1}$$

for the given conditions. Fig. 4.3 shows the resulting calibration curves for partial

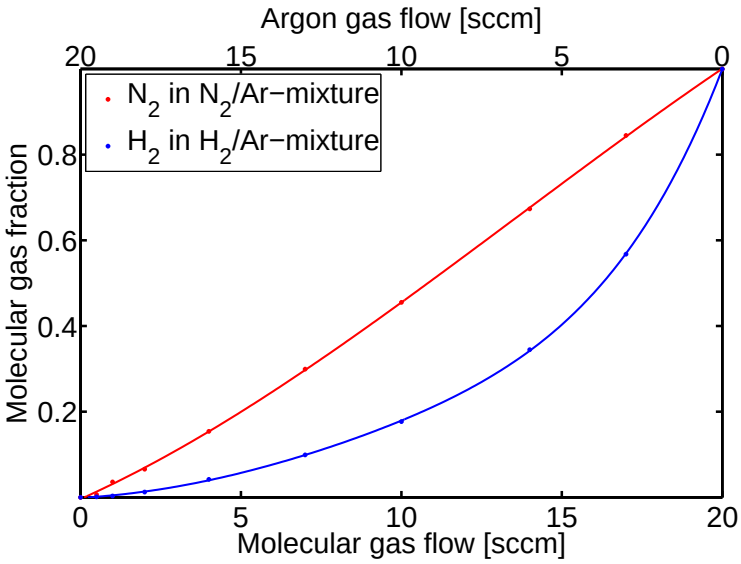

Figure 4.3.: Partial gas flow vs. partial pressure in argon-molecular gas admixtures. Total gas flow is 20 sccm at a total gas pressure of $p_{\mathrm{gas}} = 10$ Pa.

gas flow and pressure in argon-molecular gas mixtures measured in PULVA-INP. The solid lines in fig. 4.3 show a polynomial fit.

The plasma is generated between the upper capacitively coupled rf-electrode (fig. 4.2(b)), which is driven at 13.56 MHz, and the bottom Adaptive Electrode and walls. Typical discharge parameters are gas pressures between $p_{\mathrm{gas}} = 1$ Pa and 100 Pa and rf-power from $P_{\mathrm{rf}} = 5$ W to 100 W with an amplitude up to $V_{\mathrm{rf}} = 1$ kV. Electron densities in the plasma bulk are in the range of $n_{\mathrm{e}} = 10^9$ cm^{-3} to 10^{11} cm^{-3} at temperatures from $k_{\mathrm{B}}T_{\mathrm{e}} = 0.8$ eV to 2.8 eV (argon).

The Adaptive Electrode (AE) [1, 2] is the most prominent component of PULVA-INP, it consists of more than 100 square pixels with an area of $7 \cdot 7$ mm^2 which can be biased individually in real-time. It is a custom-made electrode designed by Kayser Threde [3] after a similar electrode used at the MPI in Garching [4]. Injected micro-particles can be confined in the rf sheath above the bottom electrode, using the biasing options of the AE as shown in fig. 4.2(c). Generally the bias voltages for confining purposes is between $V_{\mathrm{bias}} = -5$ V and -20 V. The position of the particles varies with discharge power and remains almost independent of gas pressure. Typically the particles are confined one millimeter above the AE.

4.2. Langmuir probe measurements

Langmuir probe measurements are performed through a tilted side flange of the vessel as shown in fig. 4.1 using a SmartProbe$^{\mathrm{TM}}$ system (Scientific Systems) and a personal computer. In the present work in PULVA-INP the probe tip consists of a piece of tungsten wire, several mm long and some hundred microns in diameter. It is fixed on a linear translation stage which holds electrical connection and filter electronics. This allows to perform vertically resolved measurements and can

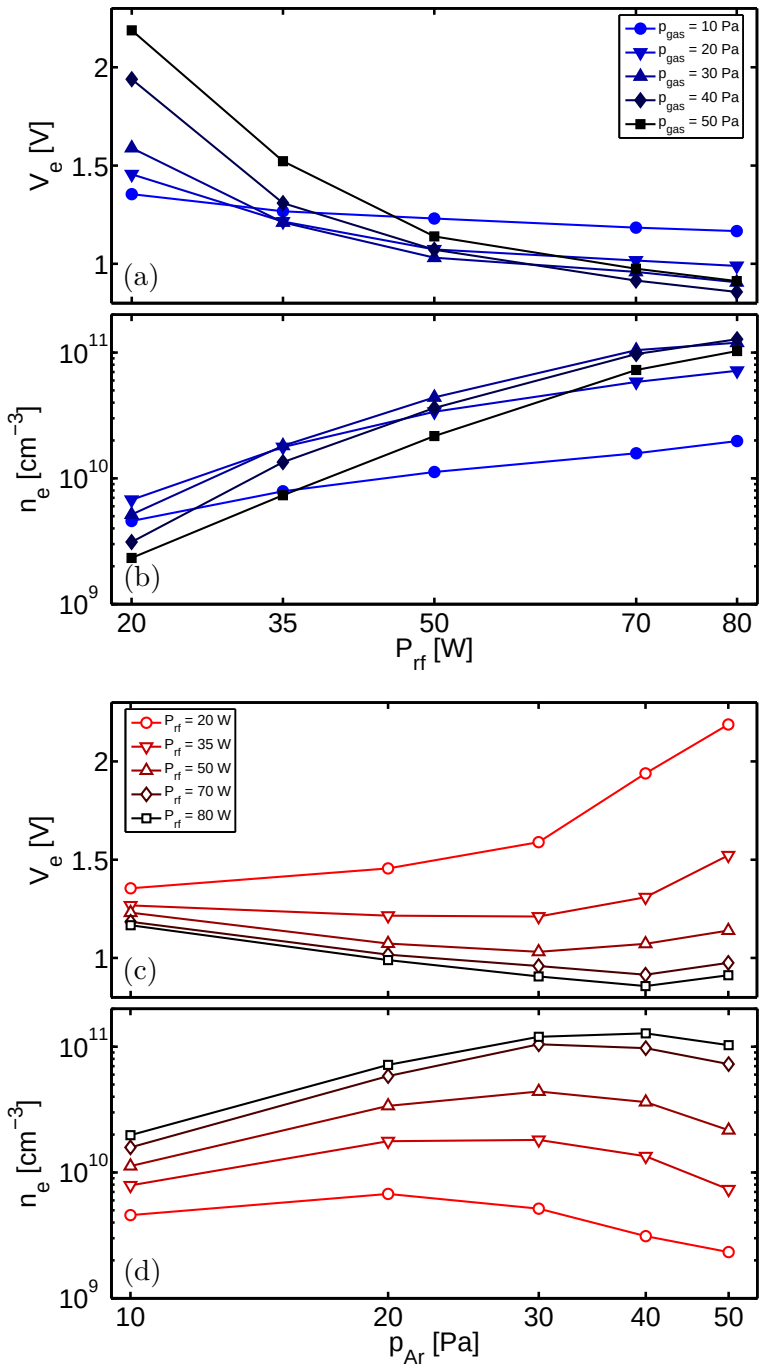

Figure 4.4.: Plasma parameters V_e and n_e in argon at a position of 15.5 mm above the AE, measured with the Smart Probe at different gas pressures and discharge powers.

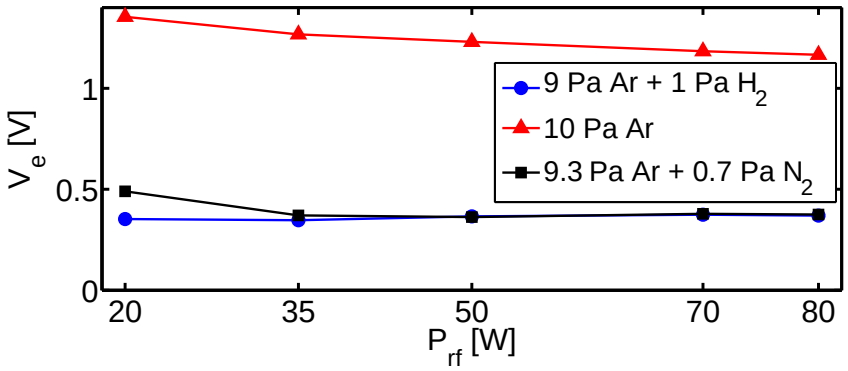

(a) Electron temperature $V_e(P_{rf})$ in Ar, Ar+H_2 and Ar+N_2.

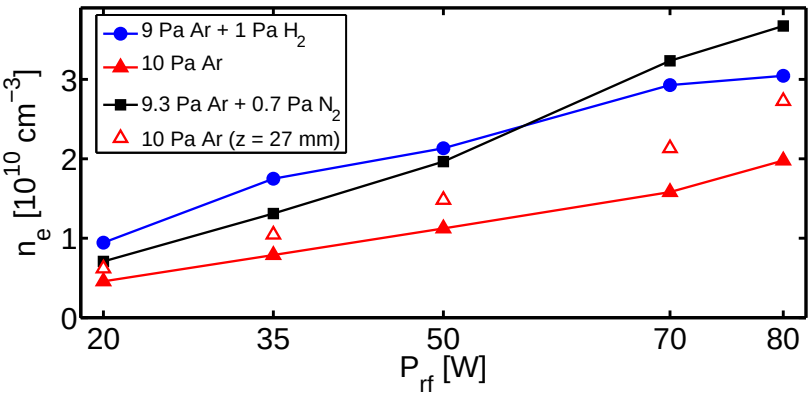

(b) Electron density $n_e(P_{rf})$ in Ar, Ar+H_2 and Ar+N_2.

Figure 4.5.: Plasma parameters V_e and n_e at a gas pressure of $p_{gas} = 10$ Pa in different gas mixtures, measured 15.5 mm above the AE. In (b) also the electron density measured 27 mm above the AE is shown.

also be moved back and forth to avoid unnecessary contact to the plasma. Data acquisition is performed using the commercial software SmartSoft^{TM} [5]. Each measurement series is initiated after manually positioning the probe in the plasma volume and cleaning the probe by applying a positive bias voltage, which has to be adjusted with respect to the plasma density. The bias accelerates electrons towards the probe, resulting in a faint glow of the probe tip and the evaporation of possible contamination. Afterwards, the measurements are initiated, allowing for a pre-selection of the number of voltage sweeps, probe positions and current measurements per probe voltage. The current-voltage characteristics are later evaluated from a selfmade analysis code as described in section 2.2.

The resulting plasma parameters V_e and n_e in argon are shown in fig. 4.4 as a function of gas pressure and discharge power, respectively. The shown measurements have been performed in the center of the discharge, 15.5 mm from the AE. The plasma parameters are very homogeneous in radial direction in front of the AE [6]. In axial direction the electron density increases towards the center of the discharge. In fig. 4.5, the plasma parameters of $p_{Ar} = 10$ Pa are compared to results obtained in argon-molecular gas mixtures (9.3 Pa Ar + 0.7 Pa N_2 and 9 Pa Ar +

1 Pa H_2, respectively). Again the measurement position is 15.5 mm above the AE. Additionally, fig. 4.5(b) shows the electron density n_e measured 27 mm above the AE in argon, which is the position of the calorimetric probe.

4.3. Particle temperature measurements

As discussed in chapter 3, for the determination of the particle temperatures phosphor grains (YVO_4:Eu^{3+}) of approximately 11 μm in diameter are used and the spectral distribution of their luminescent emission is evaluated. After the phosphor particles are confined above the center pixel of the AE (which corresponds to the central dust-free region in the middle of the particle cloud shown in fig. 4.2(c)), their luminescence can be excited by means of a mercury arc lamp (see fig. 4.1). The lamp housing is equipped with a cooled dichroic mirror, reflecting the near-ultraviolet emission of the lamp. A second mirror is used to image the mercury arc onto the particles. This mirror is also used for fine tuning when the vertical position of the particles is changed. To switch the excitation on and off, a filter wheel is placed between lamp and plasma. This wheel is equipped with a broad band interference filter (λ_c = 313 nm), an empty slot and a cover to interrupt illumination.

The empty slot in the wheel is used for aligning purposes and for benchmarking. If the particles are illuminated with the full Hg-spectrum, their temperature is slightly higher than with broadband filter due to radiative heating [7], as illustrated in fig. 4.9(b), but the emission intensity is much stronger. From this it can be seen that the influence of uv particle illumination is negligible for the particle temperature if the filter is used. Emission of the particles is observed at an angle of 90° to the incoming excitation. The light is collected by a large, partially shaded lens, and collimated after passing an aperture. To allow for vertical tracking of the detector optics, a periscope-like construction is implied. Particle emission is finally detected by an 500 mm imaging spectrograph (ACTON SpectraPro 2560 i), using a 1200 mm^{-1} grating blazed at 500 nm, and a back-illuminated CCD-camera (Princeton Instruments PIXIS 400 B).

The emission, related to the particles under *uv*-illumination is separated from the plasma background by subtracting the spectrum with blocked excitation from that with filtered *uv*-excitation, as depicted in fig. 4.6. The occurrence of stray light from the Hg lamp in the spectrum is suppressed by the dichroic mirror in the lamp housing and the interference filter. Several measurements are averaged, this allows for the identification and rejection of spikes and noisy plasma emission lines.

For comparison, calibration spectra are measured inside a special calibration oven at known temperatures. The careful recorded spectra provide a temperature resolution of 0.1 K. A scheme of the oven is shown in fig. 4.7. A copper block, providing large heat capacity and heat conductivity, is heated using an electrical heating wire spooled around an insulating ceramic layer. Inside the copper block, a copper object holder can be housed where the phosphor is placed in a small drill hole. Alternatively, for more precise measurements a small quartz cuvette can be housed inside the copper block, filled with a suspension of phosphor particles in Balzers P3 scroll pump oil. The cuvette is closed by a Teflon cap (not shown).

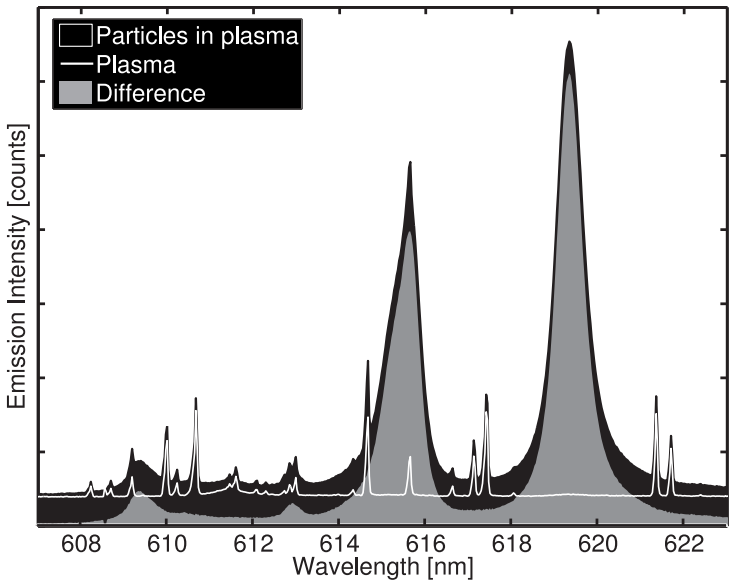

Figure 4.6.: The emission of the YVO_4:Eu particles (gray area) is obtained by the difference of the emission spectrum of excited phosphor particles in the plasma (black area) and the plasma background (white line).

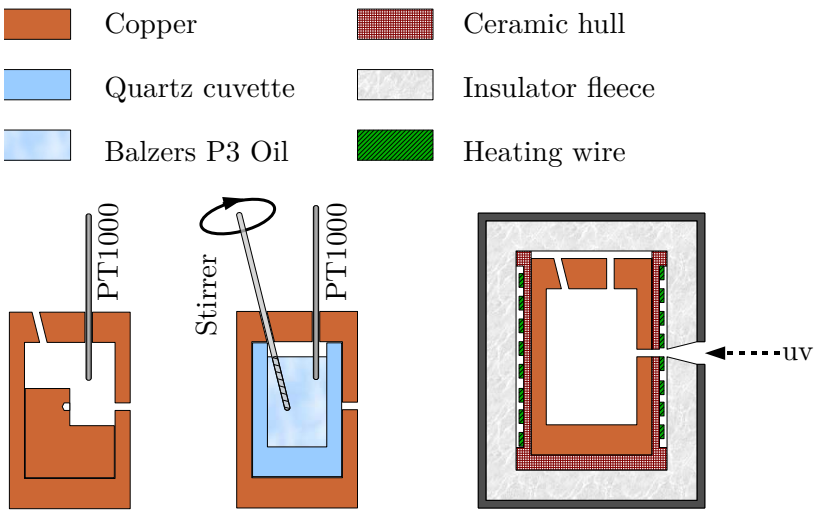

Figure 4.7.: Oven for calibration measurements. It consists of a copper block, heated by an electrical heating wire. The wire is spooled around an insulating ceramic shell. Thermal insulation is maintained from ceramic fleece. The copper block (right) can contain a copper object holder (left) or a quartz cuvette (middle).

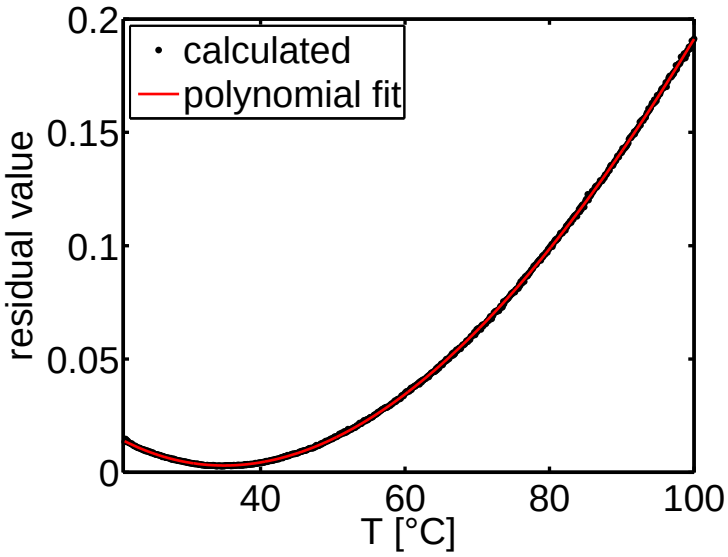

Figure 4.8.: Residuals $R(T)$ calculated as described in eqn. (4.2) and fitted with a sixth-order polynomial. The resulting particle temperature is the minimum temperature value in the fit, which is 34.9° C in this example.

The temperature is measured by a PT 1000 resistance thermometer. The optical setup outside the oven is similar to that shown in fig. 4.1 with the oven instead of the discharge vessel. Phosphor excitation is provided through a small drilling hole at one side of the copper block. Another hole is used to observe the particle emission. The suspended particles turned out to settle down quickly at higher oil temperatures, so continuous stirring is required. This is achieved by a small electro-motor with a drill-shaped stirring tip, fed through an additional hole in the top. The whole apparatus is placed within a box, thermally insulated by 20 mm of ceramic fleece material. Temperature gradients within the copper box are assumed to be very small, if the temperature remains constant or is changing slowly. The calibration measurements were performed with temperature changes smaller than 1 K per minute.

For the determination of the particle temperature, their background corrected spectrum is compared to the calibration measurements. In a few words, the algorithm works like follows: Each measurement consists of a series of N background-corrected spectra $I_\mathrm{N}(\lambda)$. Each of these is fitted to calibration spectra $C_\mathrm{T}(\lambda) = C_\mathrm{T}(\tilde{\lambda} + \lambda_0)$ with known temperature T in a least-square algorithm. In chapter 3, some calibration spectra are shown to illustrate the temperature dependence of the phosphor emission (fig. 3.4). Free parameters in the fit are the scaling parameter c and offset parameters for wavelength λ_0 (semi-global) and intensity I_0, respectively. For the wavelength correction, a linear interpolation between data points is performed. The following procedure may be described via

$$R_\mathrm{N}(T) = \sum_\lambda \left(I_\mathrm{N}(\lambda) - c_\mathrm{N}(T) \cdot C_\mathrm{T}(\lambda, \lambda_0(T)) - I_{0,\mathrm{N}}(T)\right) \quad , \tag{4.2}$$

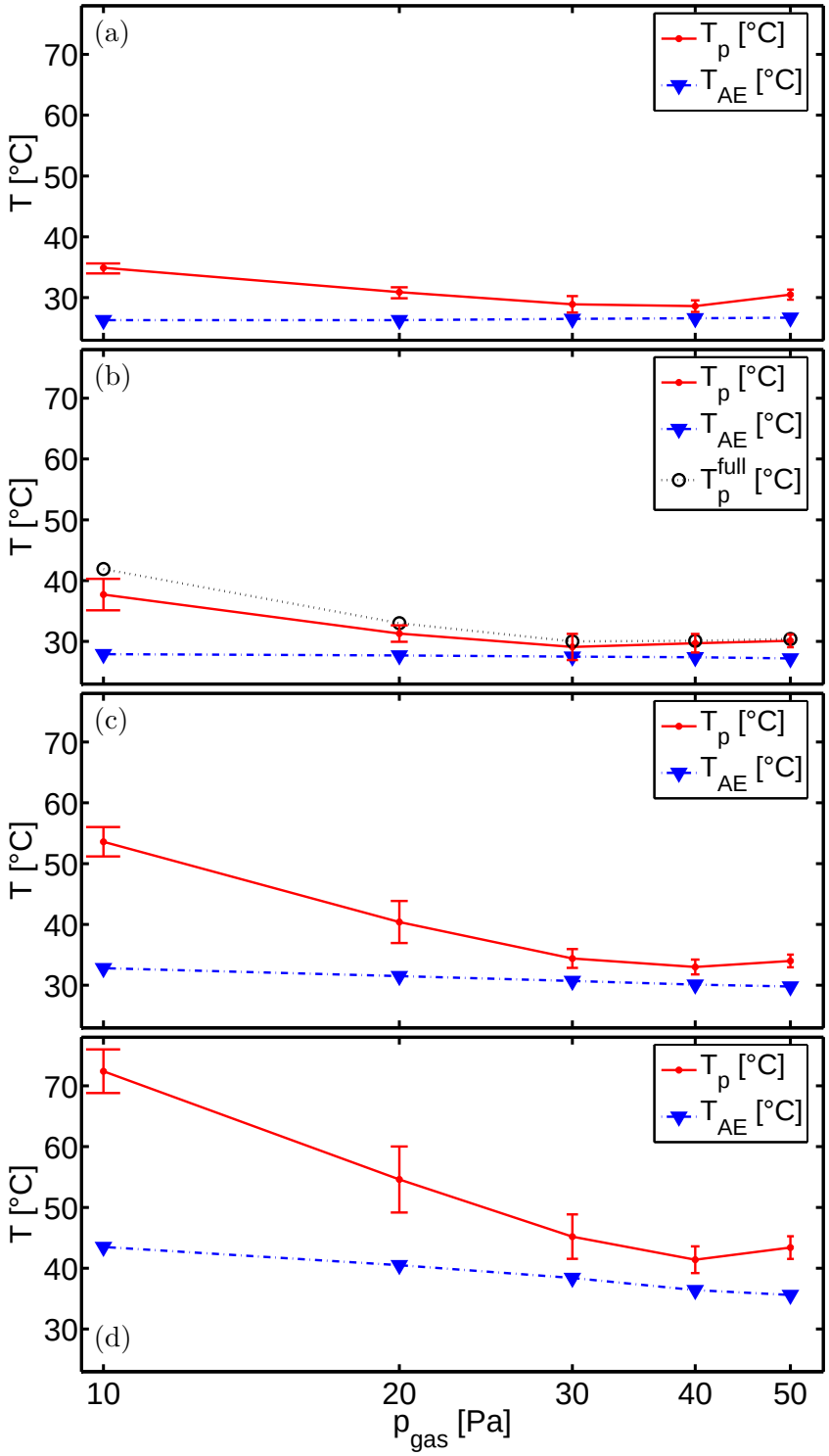

Figure 4.9.: Particle temperature T_μ and electrode temperature T_{AE} as a function of gas pressure for a discharge power P_{rf} of (a) 10 W, (b) 20 W, (c) 50 W and (d) 80 W. Error bars for T_μ show the standard deviation of 10 subsequent measurements.

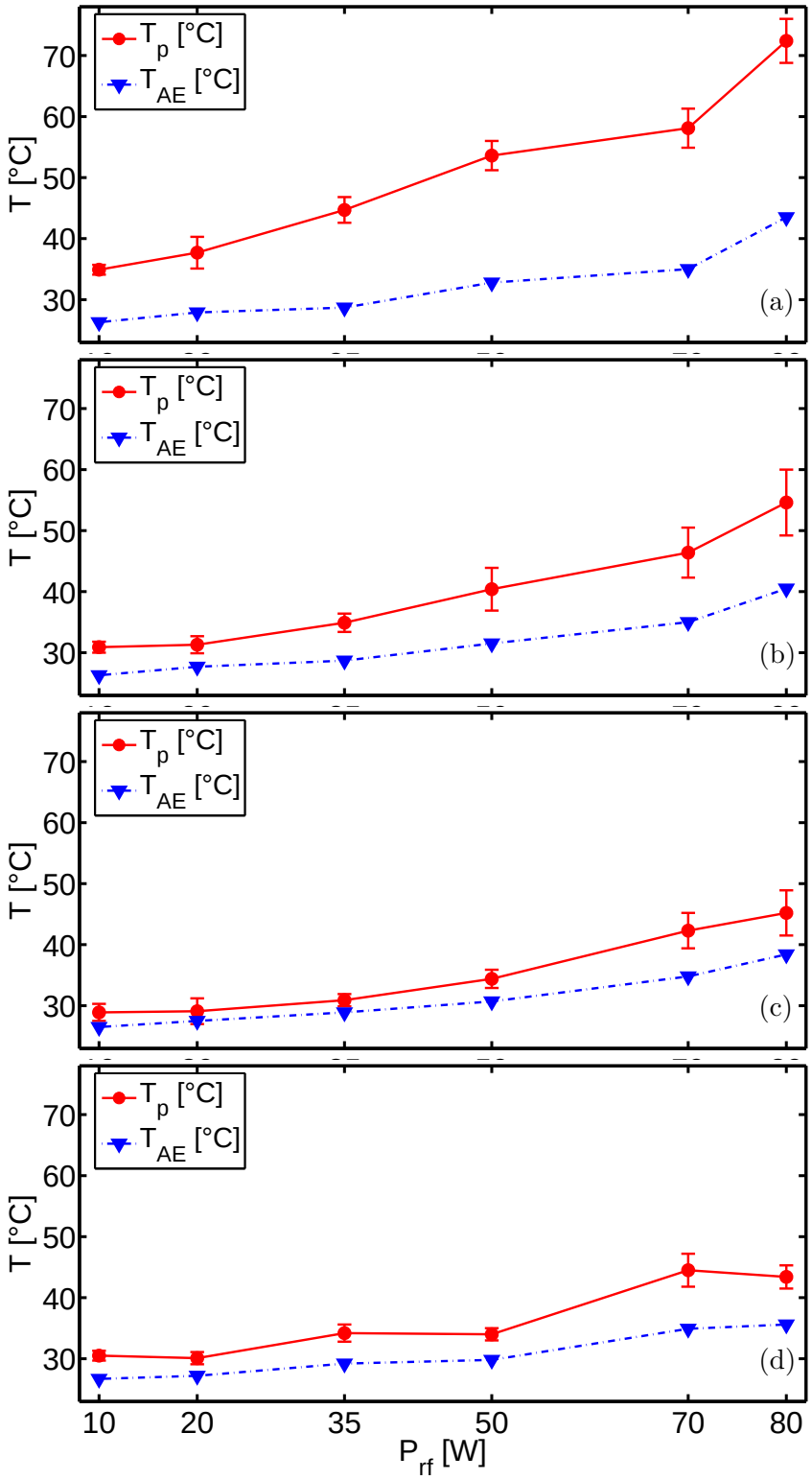

Figure 4.10.: Particle temperature T_μ and electrode temperature T_{AE} as a function of discharge power for different gas pressures in argon. From top to bottom: $p_{\mathrm{Ar}} = 10$, 20, 30 and 50 Pa. The shown error bars for T_μ describe the standard deviation of 10 subsequent measurements.

where $I_{0,\mathrm{N}}(T)$, $\lambda_0(T)$ and $c_\mathrm{N}(T)$ are varied until $R_\mathrm{N}(T)$ reaches a minimum. The temperature-interval for fitting as well as the fitting wavelength interval can be selected manually. To get rid of spikes and artefacts from fluctuations in the plasma emission, wavelengths with fluctuations in the background spectrum larger than an adjustable value are neglected. To that purpose, the spectral standard deviation of the measured intensities in the series of N background spectra is determined. Commonly, spectral regions with strong plasma emission lines are identified in this procedure. The remaining residuals $R_\mathrm{N}(T)$ show a parabola-like shape if plotted versus T, as shown in fig. 4.8. To cancel out noise, a polynomial fit of 6th order is matched to $R_\mathrm{N}(T)$, and the temperature at the minimum is identified as the particle temperature $T_{\mathrm{p,N}}$. This procedure is repeated for all N measurements. Finally, N values for $T_{\mathrm{p,N}}$ are available, from which mean T_μ and the standard deviation ΔT_μ can be calculated.

Unfortunately, heating of the electrodes and the chamber walls due to the plasma cannot be avoided and because of very large heat capacities the thermal conditions of the environment are barely reproducable in practice. To benchmark the environmental temperature conditions the temperature of the adaptive electrode T_AE has to be continuously recorded during the experiments [7]. As an in-situ reference a fiber-optical temperature sensor [8] is fixed at the AE, as shown in fig. 4.1. It is covered with a thin metal sheet to avoid direct plasma interaction. This sensor delivers the absolute temperature T_AE at the surface of the AE. Furthermore, the knowledge of the temperature T_AE provides an estimate for the environmental temperature as well as for the gas temperature. Its influence on the particle temperature, shown in figs. 4.9 and 4.10 can clearly be distinguished in the argon measurements, as explained in the following.

The sequence of the discharge conditions during the measurements in Argon had to be chosen in such a way, that the influence of the previous measurement conditions on the following ones was minimized. To that purpose, the order of measurements was 10 W (10 $\rightarrow$ 50 Pa), 20 W (50 $\rightarrow$ 10 Pa) and so forth, as sketched in fig. 4.11. Additionally, after changing the discharge conditions T_AE has to undergo a certain temperature change (e.g. $\Delta T_\mathrm{AE} \leq 1$ K within the measurement time), before the measurement is started. Fig. 4.9 and 4.10 show the results for T_μ and T_AE as a function of argon pressure and discharge power, respectively. The error bars show the standard deviation of 10 subsequent single measurements.
For the measurements at $P_\mathrm{rf} = 10$, 35 and 70 W an increase in T_AE with pressure is observable. However, at $P_\mathrm{rf} = 20$, 50 and 80 W, T_AE decreases with increasing gas pressure. Of course this does not show a dependence of T_AE on the gas pressure, but rather is an artefact caused by the sequence order and the thermal inertia of vessel and electrode, which does not attract attention when maintaining the original order. If the presentation of the measurements is changed, the influence of T_AE on the particles can clearly be identified: In fig. 4.10, T_AE shows a zigzag-like shape which can be observed especially in 10 Pa and 50 Pa, occurring with an opposite sign. This may look like noise in the first moment, but the same behavior also can be observed in T_μ.

Fig. 4.12 shows T_μ and T_AE in argon-molecular gas mixtures at a gas pressure of $p_\mathrm{gas} = 10$ Pa. No sequential artefacts are present, because no variation in gas pressure has been performed and P_rf was increased step by step. In the gas mixtures,

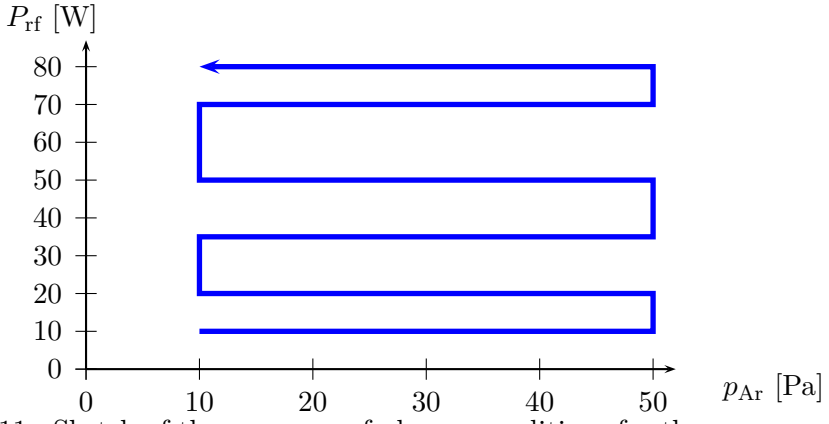

Figure 4.11.: Sketch of the sequence of plasma conditions for the measurement of the particle temperature in argon. Especially at high discharge power and low gas pressure, the chamber heats up quickly. To keep the temperature changes between successive measurements as small as possible, the shown order was chosen for the sequence of discharge conditions.

the shown errors which give the standard deviation of 10 subsequent measurements increase with discharge power, which is not found in the argon measurements in fig. 4.10. In molecular gas mixtures the particle's floating potential is much weaker, therefore the particle confinement in the plasma sheath is more unstable and a lot of particles get lost. This is even more pronounced at higher discharge power where the vertical equilibrium position of the particles approaches the AE surface. Hence less photoluminescent emission is detected and a decrease in the signal-to-noise ratio takes place. It may be noted that the mass density of the phosphor particles is about two times bigger than that of common micro-particles. Confining the phosphor particles generally appeared to be more difficult than e.g. MF particles. A comparison of mass densities and melting points of different materials is given in tab. 4.1. By comparing figs. 4.12(a) and 4.12(b) a much higher particle temperature T_μ seems to occur in argon-hydrogen than in argon-nitrogen. It should be emphasized that also the electrode temperature T_{AE} is higher in the latter case. In analogy to the argon discharge at different powers, this partly might be caused by a different history of discharge conditions. However, the temperature increase with rf-power is stronger in argon-hydrogen. In the same tine, the difference $T_\mu - T_{\mathrm{AE}}$ appears more distinctive. This could be a hint for a more pronounced plasma chemistry taking place in the argon-hydrogen mixture, where the dissociation threshold

	MF	SiO_2	PS	PMMA	YVO_4	Y_2O_3
Density [g/cm^3]	1.51	1.8 - 2.0	1.05	1.19	4.22	5.03
Melting point [K]	ca. 600	ca. 1300	ca. 400	ca. 430	ca. 2100	ca. 3000

Table 4.1.: Comparison of mass densities and melting points of common micro-particles to those uf the phosphor particles

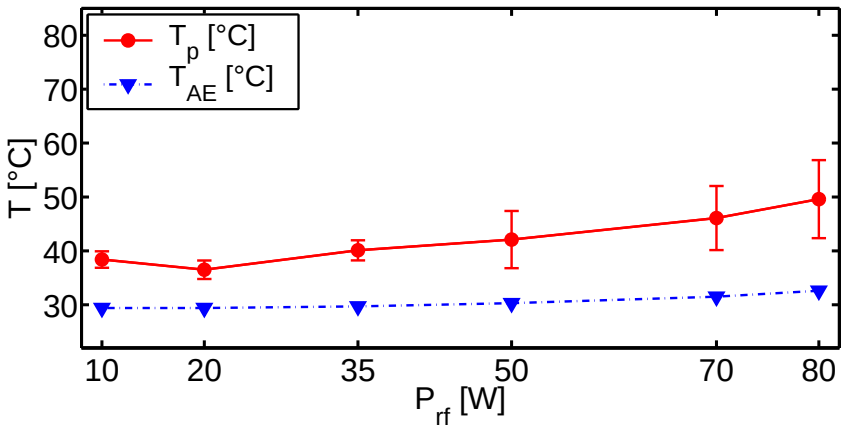

(a) 9.3 Pa argon and 0.7 Pa nitrogen

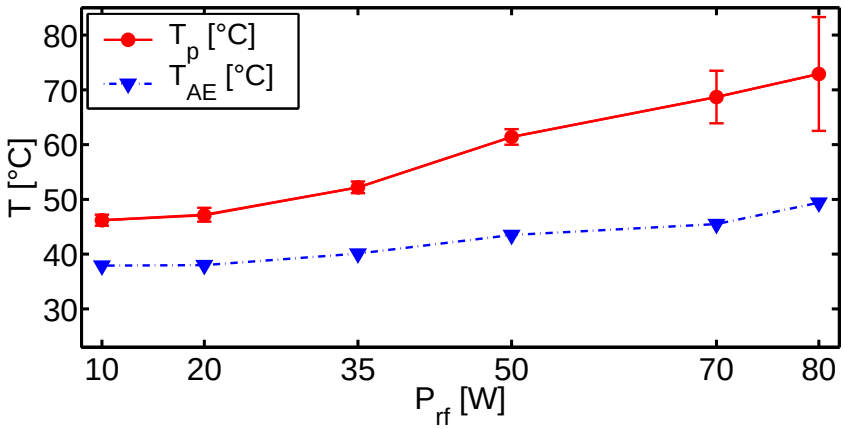

(b) 9 Pa argon and 1 Pa hydrogen

Figure 4.12.: Particle temperature T_μ and electrode temperature T_{AE} as a function of discharge power at $p_{\mathrm{gas}} = 10$ Pa in argon-molecular gas mixtures. The shown error bars for T_μ describe the standard deviation of 10 subsequent measurements.

for H_2 is 4.5 eV while it is 9.8 eV for N_2. From this, a higher electron impact dissociation rate can be expected in argon-hydrogen, causing a larger heat release to the surface of AE and to the micro-particles from association processes than in the argon-nitrogen mixture. Additionally, the charge transfer reactions

$$\mathrm{Ar}^+ + \mathrm{H}_2 \rightarrow \mathrm{ArH}^+ + \mathrm{H}$$
$$\mathrm{Ar} + \mathrm{H}_2^+ \rightarrow \mathrm{ArH}^+ + \mathrm{H}$$

as well as the dissociative recombination

$$e + \mathrm{ArH}^+ \rightarrow \mathrm{H} + \mathrm{Ar}$$

result in the production of atomic hydrogen [9, 10]. As the density of ArH^+ in argon-hydrogen plasmas appears to be rather high, this processes must be very effective.

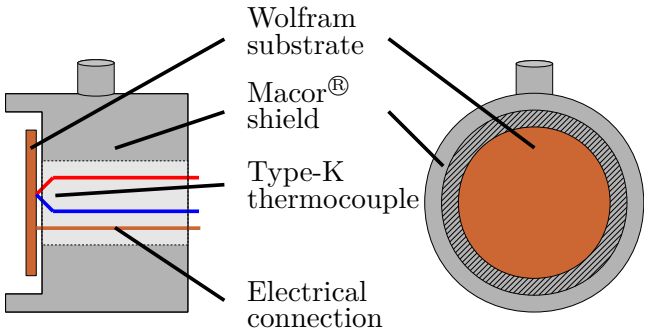

Figure 4.13.: Scheme of the Calorimetric probe. Electrical connections from thermocouple and substrate to the electronic box are fed through the probe shaft.

Analogous processes for ArN^+ in argon-nitrogen mixtures may also occur, but to a much smaller extent [11].

4.4. Calorimetric probe measurements

For comparative measurements with a calorimetric probe, a linear translation stage is fed through a side flange of the vessel as shown in fig. 4.1, allowing the probe to be moved radially through the plasma in a height of 27 mm above the AE inside the plasma volume. The probe consists of a 50 μm thick tungsten dummy substrate, 20 mm in diameter with a heat capacity of $C_S = 0.14$ J K^{-1}. The substrate is housed in a cylindrical Macor® shield [12], providing low heat conductivity and high heat capacity to minimize artefacts from heat conduction to the holder. Underneath the substrate a thermocouple is brazed, allowing the determination of temperature changes of the substrate. A detailed sketch is shown in fig. 4.13.

For the measurements the probe is placed at the center of the discharge, facing towards the rf electrode. The probe surface is at floating potential, which can be measured via an electrical connection. The temperature-dependent voltage at the thermocouple is captured by an electronic box and fed to the PC, where the temperature can be observed in real-time via a LabView™ application. After data capture is started, the plasma is switched on for a certain time and the temperature response from plasma ignition and successive plasma extinction is observed. The stored data are later evaluated as briefly described in section 2.4. The longer the plasma pulse is extended and data acquisition is performed, the more accurately results can be obtained. However, also the Macor shield and holder are heated during plasma interaction, and heat conduction starts to grow important. To avoid this, plasma operation should be rather short. Thus, the power resolution of the probe system is limited and a slow temperature change of the substrate cannot simply be compensated by longer plasma pulses.

The calorimetric measurements in argon in fig. 4.14 show the total energy influx density J_{in} towards the tungsten dummy substrate. To guide the eye, a second-order polynomial fit is drawn. The shown error bars give a guess of the expected

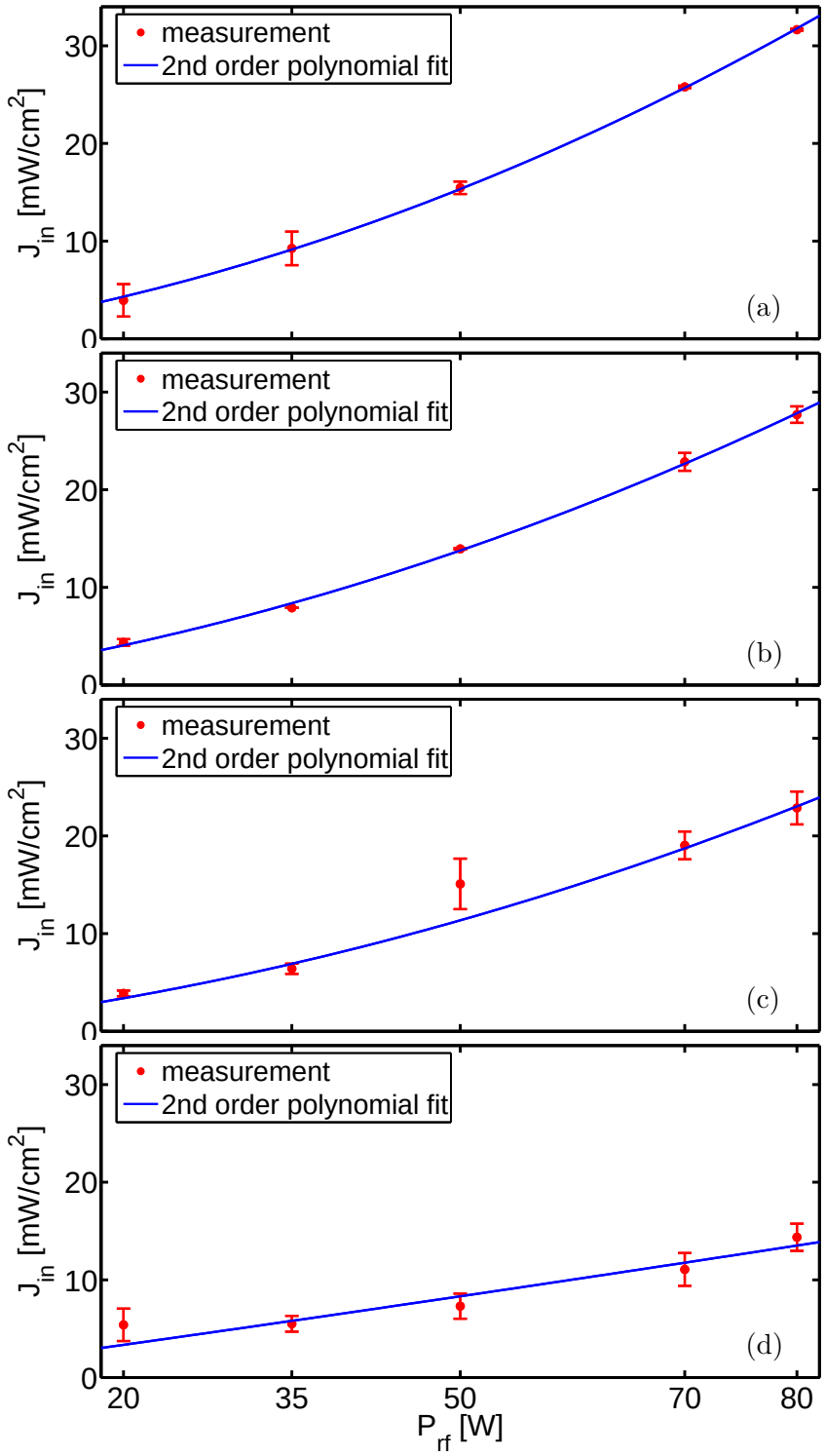

Figure 4.14.: Energy influx density to the dummy surface at different gas pressures. From top to bottom: $p_{\mathrm{Ar}} = 10$, 20, 30 and 50 Pa. The value at $p_{\mathrm{Ar}} = 30$ Pa and $P_{\mathrm{rf}} = 50$ W has been excluded for the fit.

statistical error, they are estimated from the difference in the slopes of dT_{heat}/dt and dT_{cool}/dt. A more detailed discussion on the estimation of the errors can be found in [13].

Bibliography

[1] R. Basner, H. Fehske, H. Kersten, S. Kosse and G. Schubert: *Manipulation of micro-disperse particles in a process plasma.* Vakuum in Forschung und Praxis **17** (5), pp. 259–261 (2005). See page: 46, 48

[2] R. Basner, F. Sigeneger, D. Loffhagen, G. Schubert, H. Fehske and H. Kersten: *Particles as probes for complex plasmas in front of biased surfaces.* New J. Phys. **11** (1), p. 013041 (2009). See page: 48

[3] Kayser-Threde GmbH, Wolfratshauser Straße 48, 81379 Munich, Germany http://www.kayser-threde.de/ See page: 48

[4] B. M. Annaratone, M. Glier, T. Stuffler, M. Raif, H. M. Thomas and G. E. Morfill: *The plasma-sheath boundary near the adaptive electrode as traced by particles.* New J. Phys. **5** (1), p. 92 (2003). See page: 48

[5] Scientific Systems, Dublin, Ireland: *Smart Probe Product Manual.* http://www.scisys.com/langmuir.cfm. See page: 50

[6] M. Tatanova, G. Thieme, R. Basner, M. Hannemann, Y. B. Golubovskii and H. Kersten: *About the EDF formation in a capacitively coupled argon plasma.* Plasma Sources Sci. T. **15** (3), p. 507 (2006). See page: 50

[7] H. R. Maurer, R. Basner and H. Kersten: *Temperature of particulates in low-pressure rf-plasmas in Ar, Ar/H2 and Ar/N2 mixtures.* Contrib. Plasm. Phys. **50** (10), pp. 1521-3986 (2010). See page: 51, 56

[8] U. Roland, C. Renschen, D. Lippik, F. Stallmach and F. Holzer: *A New Fiber Optical Thermometer and Its Application for Process Control in Strong Electric, Magnetic, and Electromagnetic Fields.* Sensor Letters **1**, pp. 93–98 (2003). See page: 56

[9] E. Neyts, M. Yan, A. Bogaerts and R. Gijbels: *Particle-in-cell/Monte Carlo simulations of a low-pressure capacitively coupled radio-frequency discharge: Effect of adding H[sub 2] to an Ar discharge.* J. Appl. Phys. **93** (9), pp. 5025–5033 (2003). See page: 58

[10] E. Neyts, M. Yan, A. Bogaerts and R. Gijbels: *PIC-MC simulation of an RF capacitively coupled Ar/H2 discharge.* Nucl. Instrum. Meth. B **202**, pp. 300 – 304 (2003). 6th International Conference on Computer Simulation of Radiation. See page: 58

[11] Y. Wang, R. J. V. Brunt and J. K. Olthoff: *Mass spectrometric measurement of molecular dissociation in inductively coupled plasmas.* J. Appl. Phys. **83** (2), pp. 703–708 (1998). See page: 59

[12] M. Stahl, T. Trottenberg and H. Kersten: *A calorimetric probe for plasma diagnostics*. Rev. Sci. Instrum. **81** (2), 023504 (2010). See page: 59

[13] M. Stahl: *Energiestrommessungen in Prozessplasmen*. Master's thesis, Institute for experimental and applied physics, University of Kiel (2009). See page: 61

5. Discussion of the energy balance

In chapter 2.3 a model was presented for the description of energy fluxes between a plasma and immersed surfaces. The plasma has been characterized in chapter 4, and the temperatures of the particles and their environment were determined. Also energy fluxes to a calorimetric probe in the plasma have been measured. In this chapter, the experimental results will be summarized and discussed. The model will be applied to some experimental results to quantify the plasma-surface interactions for the calorimetric probe and particle measurements, respectively. The model results are discussed in terms of the different conditions, affecting dummy substrate and micro-particles in argon, and in terms of involved model assumptions. The findings are finally applied for the modeling of energy flux densities in argon-hydrogen mixtures and the plausibility of the resulting achievements are debated.

5.1. Plasma parameters

Langmuir probe measurements in argon have been performed in a parameter range between $p_{\mathrm{gas}} = 10$ to 50 Pa and $P_{\mathrm{rf}} = 20$ to 80 W. In fig. 4.4(a) drop in electron temperature V_{e} with increasing rf power P_{rf} is observed. At low gas pressures this increase is rather weak, but with increasing pressure it becomes more pronounced (see fig. 4.4(c)). Similar results have been measured by Tatanova et al. [1], where this feature is explained by a transition from stochastic electron heating in the rf sheath at very low pressures to ohmic heating in the plasma bulk with increasing collisionality. In fig. 4.4(d) n_{e} shows a maximum, shifting towards higher pressures with increasing P_{rf}. At lower pressures, n_{e} increases monotonically with increasing gas density. The transition into the collisional heating regime, connected with a density drop in the outer plasma regions, depends on the electron temperature and, thus, on the discharge power. Under admixture of molecular gas the electron temperature dramatically decreases. This is caused by the occurrence of inelastic electron collisions with molecules, which can now occur at very low energies, exciting molecular vibrational and rotational energy levels.

Of course a Maxwellian EEDF is assumed for the evaluation of the current-voltage characteristics. The EEDFs were proven to be approximately Maxwellian. Figs. 5.1(a) and 5.1(b) show an example of a measured $I(U)$ characteristic and the obtained EEDF. Similar measurements in PULVA-INP have previoulsly been published by Tatanova and colleagues [1, 2] for a wide parameter range. At $p_{\mathrm{gas}} \leq 20$ Pa, good accordance was found as well in argon as in argon-molecular gas mixtures. At higher gas pressures and simultaneously lower discharge power, the deviation from a Maxwellian distribution function increased.

The same evidence is found if the relation of V_f and V_{e} is compared, which after eqn. (2.32) should remain constant in the OML regime if the effective ion mass is

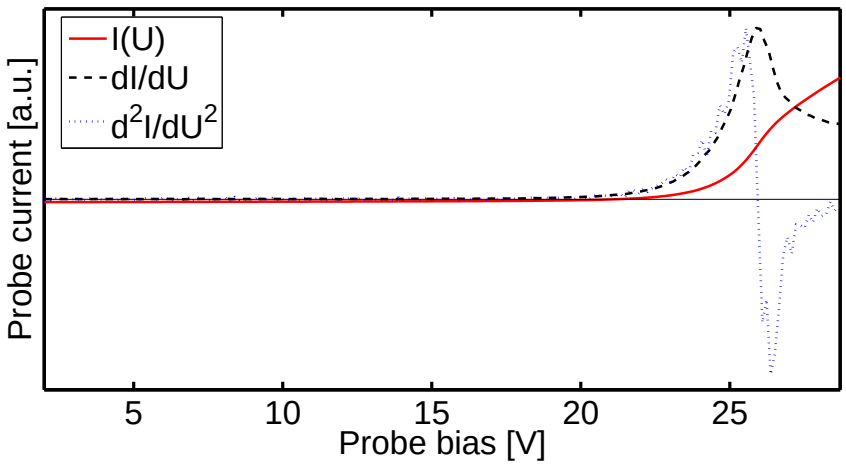

(a) Probe characteristic, measured in 10 Pa argon at $P_{\mathrm{rf}} = 10$ W and the first and second derivative.

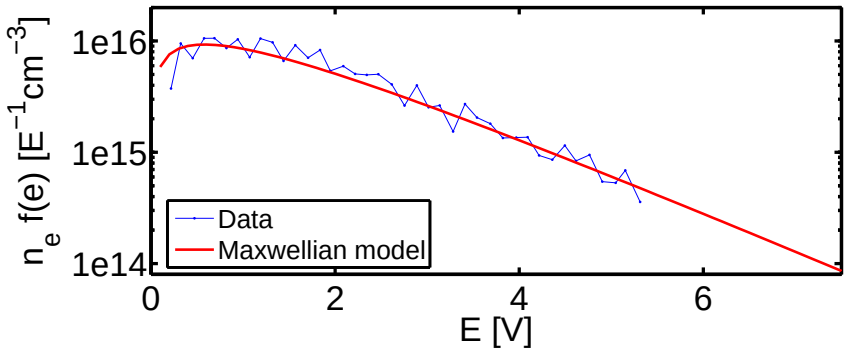

(b) EEDF determined from the probe characteristic shown in fig. 5.1(a) and a theoretical Maxwellian EEDF for comparison.

Figure 5.1.: Probe characteristic and EEDF measured in PULVA-INP. The noise in the measured derivatives and the EEDF results from a relatively large distance between neighboring bias values in the measurement.

unchanged. Fig.5.2(a) shows the (measured) floating potential, normalized by the electron temperature. As expected the value is constant over the full parameter range, except for conditions with $p_{\mathrm{gas}} \geq 30$ Pa and $P_{\mathrm{rf}} \leq 35$ W. In this region, the mean free path for ion-neutral collisions [3] increases with respect to the Debye length, and a collisionless description is not longer valid. In fig. 5.2(b), the same ratio is shown for different gas mixtures at $p_{\mathrm{gas}} = 10$ Pa. From these findings it can be concluded that the results for measurements performed at $p_{\mathrm{gas}} = 10$ Pa are plausible and a collisionless description is still valid under these conditions.

5.2. Energy flux to the dummy substrate

Calorimetric probe measurements in argon have been performed according to the Langmuir probe diagnostics (fig. 4.14). The experimental results are in good agree-

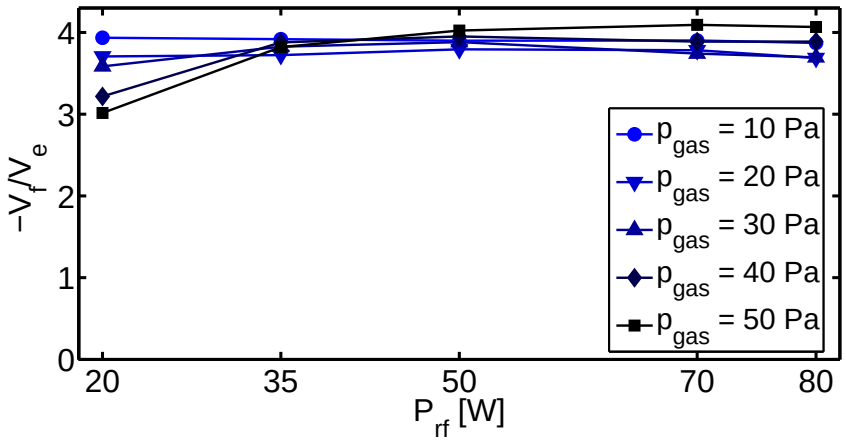

(a) Relation of measured V_f and V_e for the considered parameter range in argon.

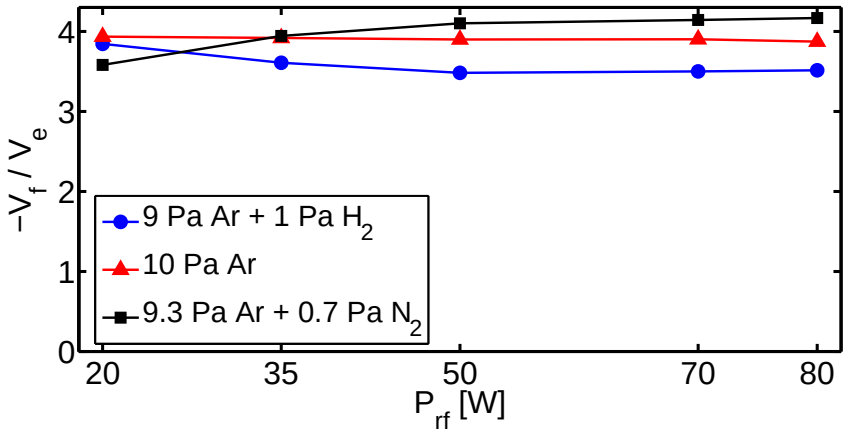

(b) Relation of measured V_f and V_e in the gas mixtures at $p_{gas} = 10$ Pa.

Figure 5.2.: The ratio V_f/V_e under different plasma conditions, measured by a Langmuir probe.

ment to those found in other experiments [4, 5] and appear in the same order of magnitude. The total energy influx density J_{in} towards the dummy surface increases with discharge power, as shown in fig. 4.14. In the same time, J_{in} decreases with increasing gas pressure in the observed pressure range [4]. In fig. 5.3 the measured total energy influx densities J_{in} to the dummy substrate at $p_{gas} = 10$ Pa is compared to model calculations. The geometry of the dummy substrate is plane, and the model results calculated from the plasma parameters, measured in a distance of $z = 27$ mm from the AE in the plasma volume are calculated for an ideal plane probe geometry. The calculation, described in section 2.3 uses an electron duty cycle of $\alpha = 1$, a geometric factor of $\eta = 1$ and a geometry exponent of $\beta = 0$ for the self-consistent calculation of V_f and the resulting energy flux densities. However, in practice plane probes do not show ideal characteristics if no guard ring is used [6] and edge effects are not negligible . In fig. 5.4, $U(I)$ characteristics of the calorimetric probe are shown. The ion saturation current is not constant, nor is the electron saturation current, and a knee appears in the electron current which

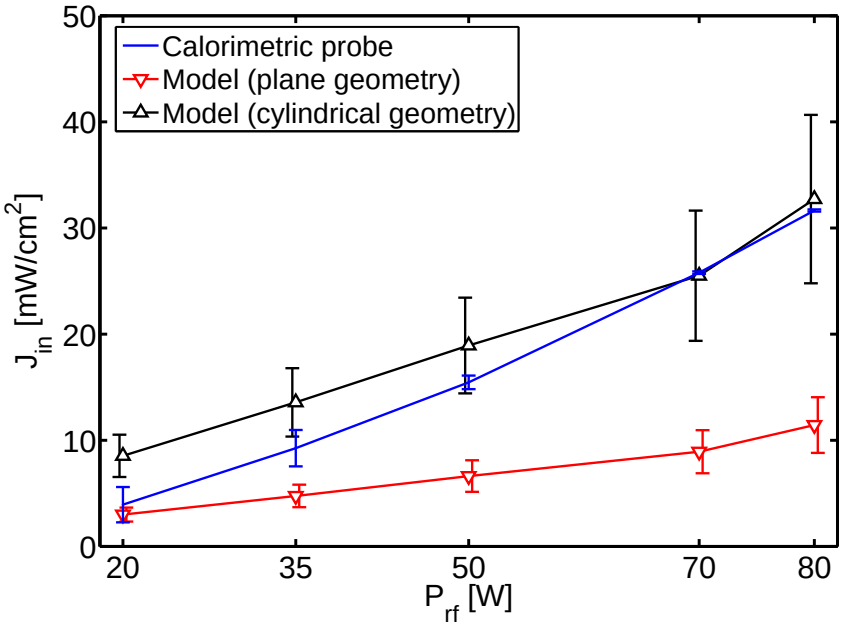

Figure 5.3.: Energy influx density measured at the dummy substrate, compared to model calculations based on the assumption of a plane and a cylindrical substrate geometry.

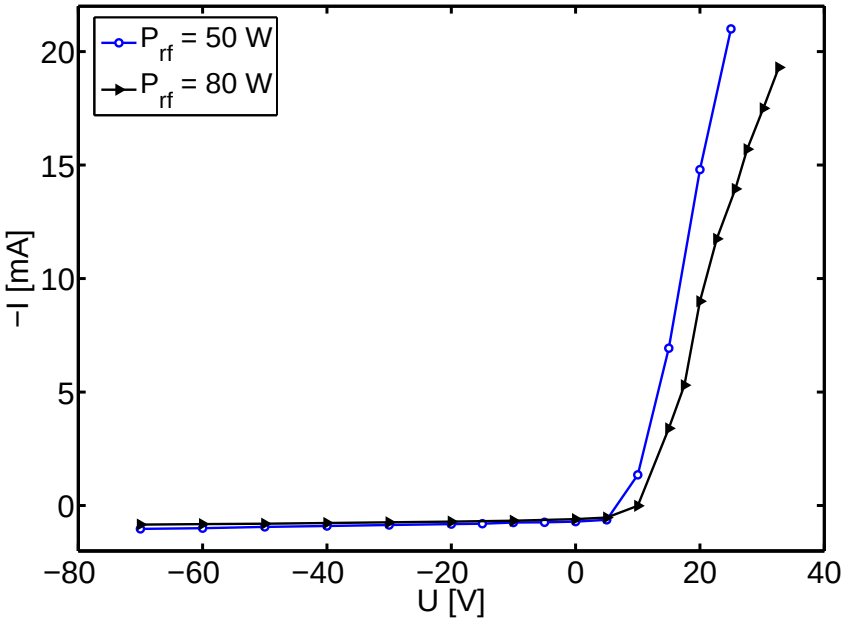

Figure 5.4.: Current-voltage characteristics of the calorimetric probe, measured by a digital multimeter. The lines are drawn to guide the eye.

is similar to that expected from a cylindrical probe as shown in fig. 2.2.
For comparison, J_{in} is also modeled for an ideal cylinder probe in fig. 5.3. Here, $\alpha = 1$, $\eta = 1$ and the geometry exponent $\beta = 0.5$, considering a low cylinder with large diameter which is pointing towards the plasma volume with the probe tip. In principle this case is identical to the model proposed by Swinkels [7, 8] who directly utilized the floating potential measured by the Langmuir probe. In fig. 5.3, the measured J_{in} is well described by the model using cylindrical geometry correction. In every point, the measured values lie between the modeled results for cylindrical and plane geometry.

For such kind of measurements, the use of a guard ring could provide a more defined probe geometry, and could thus enable a more accurate comparison to model calculations. Furthermore, the dummy substrate itself could be utilized as a Langmuir probe. Of course the large area of the substrate could be a problem, because a large current is drawn from the plasma. The cylindrical-like current-voltage characteristics tend to support this concern. However, it should be possible to at least measure the floating potential V_f accurately.

5.3. Particle temperatures and plasma-particle interaction

Particle temperature measurements have been performed in the same parameter range than Langmuir probe diagnostics (figs. 4.9 and 4.10 as well as fig. 4.12). In fig. 4.9(b), the particle temperature was shown for both, filtered uv excitation and full illumination of the uv source. From this, the influence of the uv illumination was shown to be negligible. Furthermore, this demonstrates the feasibility of the presented technique for the determination of external introduced heat fluxes under low-pressure conditions, which could be useful for a more detailed investigation of J_{rad} and J_{cond}.

For dependence of the particle temperature T_μ on p_{gas} and P_{rf} in argon, two features can be stated. First, in fig. 4.9 a decrease in T_μ with increasing argon pressure can be observed, showing a minimum around $p_{\mathrm{Ar}} \approx 40$ Pa followed by temperature increase towards higher pressure. This observation also holds for the difference $T_\mu - T_{\mathrm{AE}}$. It can be interpreted as follows:
With increasing gas pressure, the energy loss due to gas conduction increases linearly with pressure, as described in eqn. (2.31). In the same time, the electron temperature shows a smooth increase which appears above $p_{\mathrm{Ar}} \approx 30$ Pa. However, considering the recombination energy flux density $J_{\mathrm{rec}} \propto V_{\mathrm{e}}^{1/2} n_{\mathrm{e},0}$ (the fraction V_f/V_{e} in the Boltzmann factor in eqn. (2.28) remains constant for a given sort of ions, as shown in fig. 5.2(a)) to be the most important energy source, the behavior of $T_\mu(p_{\mathrm{Ar}})$ at higher pressures cannot be explained by an electron temperature increase alone in the model.

The ion trajectories are determined by orbital motion in the low pressure regime. With increasing gas pressure, collisionality increases and orbital motion starts to be replaced by a radial motion of the ions towards the particle and the ion current towards the particle surface increases. This occurs when the ion mean free path $\lambda_{\mathrm{MFP,i}}$ becomes comparable to λ_{D} [9], which is expected around $p_{\mathrm{gas}} \approx 50$ Pa in this experiment. This could be an explanation for the sudden temperature increase

above $p_{\mathrm{Ar}} = 40$ Pa and should also be observable in the behavior of the particle's floating potential. Further increase of the collisionality would result in an ohmic drop in the ion current.

In agreement to the conclusion in section 5.1 it can, thus, be reasoned that a collisionless description of the ion current to the particles is applicable at $p_{\mathrm{Ar}} = 10$ Pa, but for pressures of $p_{\mathrm{Ar}} \geq 30$ Pa a consideration of ion collisions should be included. Hence, for the modeling of energy fluxes between plasma and the particles, it will be focused on the measurements at $p_{\mathrm{gas}} = 10$ Pa.
Secondly, an increase in T_μ with P_{rf} can be observed in fig. 4.10 in argon as well as fig. 4.12 in the gas mixtures. This observation also holds for the difference $T_\mu - T_{\mathrm{AE}}$. A similar behavior has already been reported by Swinkels and co-authors [7, 8, 10] and is very plausible, because when the discharge power is increased, more power is fed to the plasma which has to be dissipated again. This temperature increase is mainly caused by an increasing plasma density, whilst the effect of V_{e} and V_f is rather small as discussed above.

In fig. 5.5 the total energy flux densities between the micro-particles and the argon plasma at $p_{\mathrm{Ar}} = 10$ Pa are shown. J_{in} is modeled from the plasma parameters, measured 15.5 mm above the AE using an electron duty cycle of $\alpha = 0.12$, a geometric factor of $\eta = 1/4$ and a geometry exponent of $\beta = 1$, as described in section 2.3. J_{out} is calculated from T_μ, T_{AE} and p_{Ar}. The value of α has been treated as a free parameter, and for $\alpha = 0.12$ a good agreement between J_{in} and J_{out} was found. This value for α is in accordance to the findings of other authors [11]. The magnitude of the total energy flux density is comparable to results published elsewhere [4, 7, 8]. The contributions to J_{in} and J_{out} are shown in fig. 5.6(a) and 5.6(b), respectively. As expected, the recombination of free electrons and ions J_{rec} at the particle surface is the most dominant energy source for particle heating,

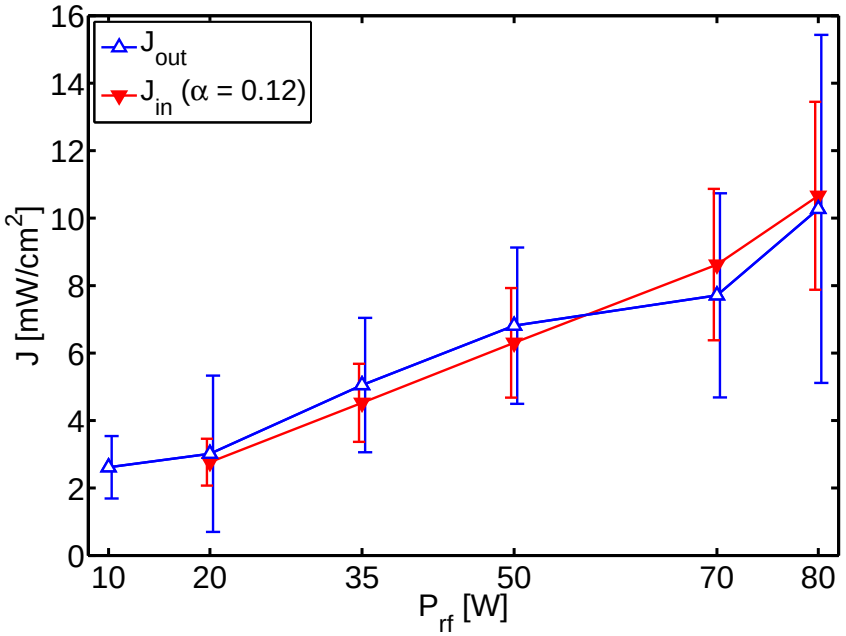

Figure 5.5.: Comparison of the total energy fluxes in 10 Pa argon.

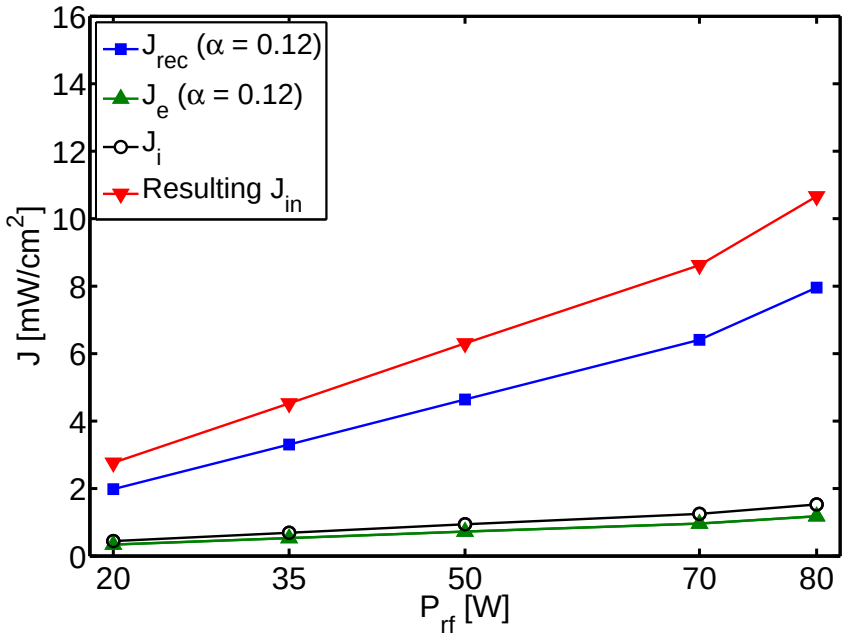

(a) Contributions to the total energy influx density J_{in} for an electron duty cycle of $\alpha = 0.12$, calculated from the plasma parameters.

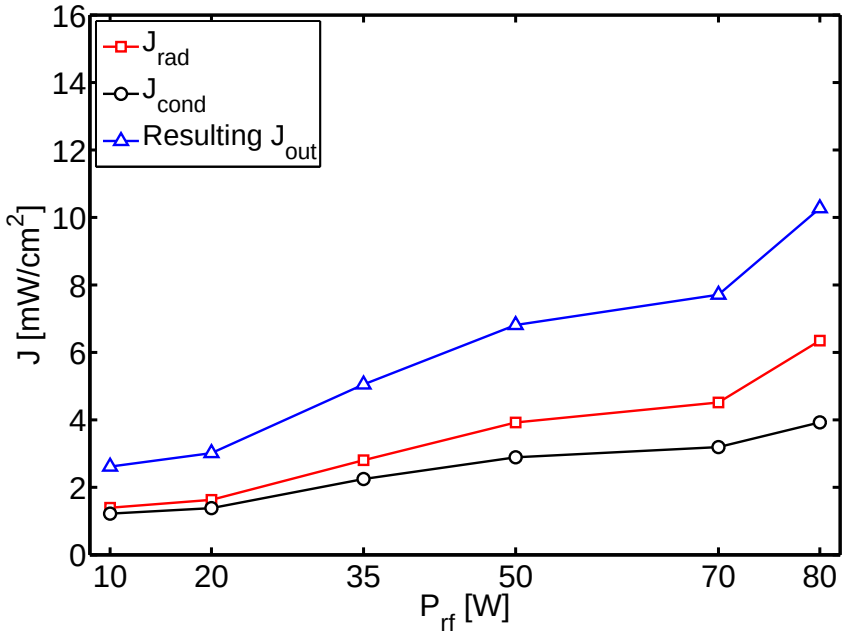

(b) Contributions to the total energy loss density J_{out}, calculated from T_μ and T_{AE}

Figure 5.6.: Comparison of the different contributions to the total energy flux densities shown in fig. 5.5 in a 10 Pa Ar discharge.

providing about 80% of the total energy influx. The contribution of kinetic energy flux densities $J_e \propto 2V_e$ and $J_i \propto V_f(V_e)$ is determined by the electron temperature V_e, and their relation is fixed due to the calculated floating potential, which for $\alpha = 0.1$ in argon becomes $V_f(V_e) \approx -2.6V_e$. Energy loss from the particle surface is obtained by radiation and conduction in comparable quantities at the present gas pressure. In principle this is in accordance to the results of Swinkels, who used a larger emissivity and therefore obtained a higher value for radiative loss. The use of the same emissivitiy would result in a larger radiative energy flux density. However, for the investigated material the use of a lower value appears to be more appropriate.

Provided that the electron duty cycle α is not changed under admixture of molecular gas, the result of $\alpha = 0.12$ can be applied to the measurements in gas mixtures. However, in gas mixture plasmas different ion species occur with different unknown densities. In the case of argon and hydrogen, three dominant ion species were observed in mass spectrometer measurements in PULVA-INP, showing comparable densities: Ar^+, ArH^+ and H_3^+. Similar findings were obtained in simulations, published by the group of Bogaerts et al. [12, 13]. In [12], simulations on a 90% argon, 10% hydrogen rf discharge at a pressure of 13.3 Pa were performed. The relative ion densities at the sheath edge $n_{Ar+} : n_{ArH+} : n_{H3+} = 7.5 : 3.5 : 0.9$, required for the calculation of J_{in} are taken from this simulation. The effect of this admixture of hydrogen on J_{in} was already shown in section 2.3, where floating potential and energy influx density due to charge carriers were calculated for argon as well as the mixture (figs. 2.4 and 2.5). But in this diagram the same plasma parameters were used for the calculations on both gas mixtures. The plasma parameters, measured by the Langmuir probe and shown in fig. 4.5 and show pronounced differences. At

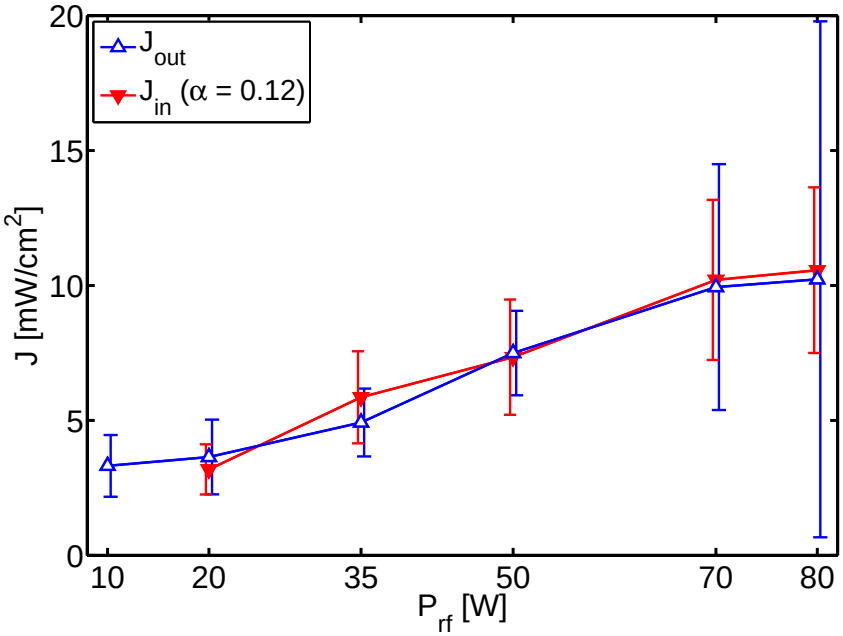

Figure 5.7.: Comparison of the total energy fluxes in the argon-hydrogen mixture

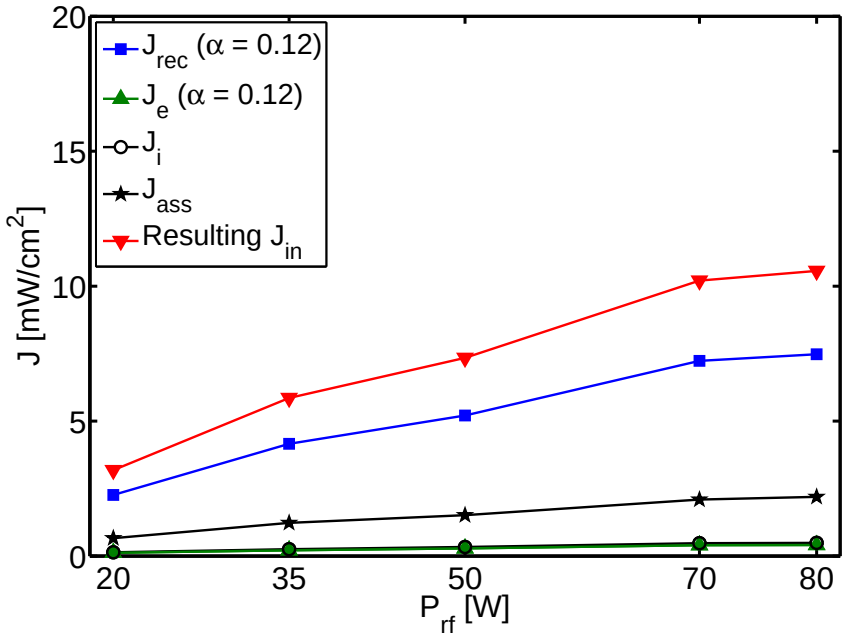

(a) Contributions to the total energy influx density J_{in} for an electron duty cycle of $\alpha = 0.12$, calculated from the plasma parameters.

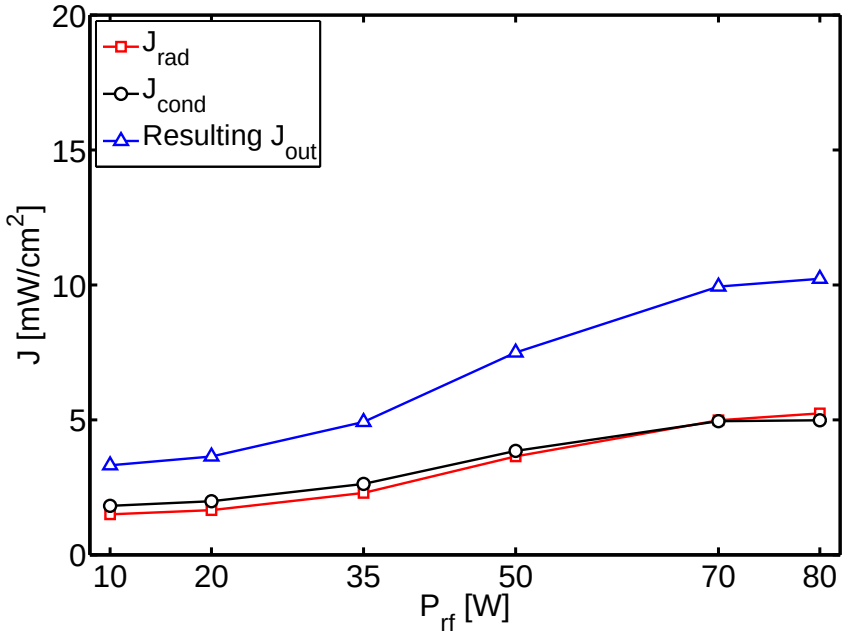

(b) Contributions to the total energy loss density J_{out}, calculated from T_μ and T_{AE}

Figure 5.8.: Comparison of the different contributions to the total energy flux densities shown in fig. 5.7 in a 10 Pa Ar discharge.

admixture of 10% molecular gas the electron temperature is reduced and in the same time the electron density is increased.

The total energy flux densities in the argon-hydrogen mixture are shown in fig. 5.7. Here, the floating potential occurs at $V_f \approx -2.4V_e$. The individual contributions to J_{in} and J_{out} are given in fig. 5.8. In this calculation, the product $\Gamma_H n_H$ was taken as a free parameter and was varied until a good accordance between J_{in} and J_{out} was achieved. As V_e is nearly constant within the considered parameter range, the number density of atomic hydrogen can be expected to be $n_H \propto n_e$. At a value of $\Gamma_H n_H \approx 3n_e$ a good agreement for J_{in} and J_{out} was found. The resulting dissociation ratio

$$\begin{aligned} D &:= \frac{n_H}{n_H + 2n_{H2}} \\ &\approx \frac{3}{\Gamma_H} \cdot 10^{-4} \end{aligned} \tag{5.1}$$

is in the order of 10^{-3}, as the association possibility Γ_H is expected to be close to 1. This value for D is comparable to the results measured in a capacitively coupled rf discharge by Pipa et al. [14, 15] when extrapolated to a position close to the metallic surface. However, the estimation of D is only a rough value, but its agreement to existing evidence can be seen as a confirmation. The contribution to J_{in} due to association processes is significant, as shown in fig. 5.8(a) and its magnitude is approximately 20% even close to the AE. Inside the plasma volume it can be expected to become more dominant if no competitive association can occur at nearby surfaces.

Bibliography

[1] M. Tatanova, G. Thieme, R. Basner, M. Hannemann, Y. B. Golubovskii and H. Kersten: *About the EDF formation in a capacitively coupled argon plasma.* Plasma Sources Sci. T. **15** (3), p. 507 (2006). See page: 63

[2] M. Tatanova, Y. B. Golubovskii, A. S. Smirnov, G. Seimer, R. Basner and H. Kersten: *Electron stochastic heating in a capacitively coupled low-pressure argon rf-discharge.* Plasma Sources Sci. T. **18** (2), p. 025026 (2009). See page: 63

[3] S. Robertson and Z. Sternovsky: *Monte Carlo model of ion mobility and diffusion for low and high electric fields.* Phys. Rev. E **67** (4), p. 046405 (2003). See page: 64

[4] A.-L. Thomann, N. Semmar, R. Dussart, J. Mathias and V. Lang: *Diagnostic system for plasma/surface energy transfer characterization.* Rev. Sci. Instrum. **77** (3), 033501 (2006). See page: 65, 68

[5] M. Wolter, M. Stahl and H. Kersten: *Spatially resolved thermal probe measurement for the investigation of the energy influx in an rf-plasma.* Vacuum **83** (4), pp. 768 – 772 (2008). Proceedings of the "Symposium on

Vacuum based Science and Technology", Greifswald, 5-7 September 2007 - DVG 2007. See page: 65

[6] G. S. Janes and J. P. Dotson: *Shielded Langmuir Ion Collection Probes.* Rev. Sci. Instrum. **35** (11), pp. 1617–1618 (1964). See page: 65

[7] G. Swinkels: *Optical studies of micron-sized particles immersed in a plasma.* PhD Thesis, TU Eindhoven (1999). See page: 67, 68

[8] G. Swinkels, H. Kersten, H. Deutsch and G. M. W. Kroesen: *Microcalorimetry of dust particles in a radio-frequency plasma.* J. Appl. Phys. **88** (4), pp. 1747 – 1755 (2000). See page: 67, 68

[9] P. Bryant, A. Dyson and J.E. Allen: *Langmuir probe measurements of weakly collisional electronegative RF discharge plasmas.* J. Phys. D Appl. Phys. **34**, pp. 95–104 (2001). See page: 67

[10] H. Kersten, D. Rohde, H. Steffen, H. Deutsch, R. Hippler, G. H. P. M. Swinkels and G. M. W. Kroesen: *On the determination of energy fluxes at plasma-surface processes.* Appl. Phys. A - Mater. **72**, pp. 531–540 (2001). See page: 68

[11] T. Trottenberg, A. Melzer and A. Piel: *Measurement of the electric charge on particulates forming Coulomb crystals in the sheath of a radiofrequency plasma.* Plasma Sources Sci. T. **4** (3), p. 450 (1995). See page: 68

[12] E. Neyts, M. Yan, A. Bogaerts and R. Gijbels: *Particle-in-cell/Monte Carlo simulations of a low-pressure capacitively coupled radio-frequency discharge: Effect of adding H[sub 2] to an Ar discharge.* J. Appl. Phys. **93** (9), pp. 5025–5033 (2003). See page: 70

[13] E. Neyts, M. Yan, A. Bogaerts and R. Gijbels: *PIC-MC simulation of an RF capacitively coupled Ar/H2 discharge.* Nucl. Instrum. Meth. B **202**, pp. 300 – 304 (2003). 6th International Conference on Computer Simulation of Radiation. See page: 70

[14] B. P. Lavrov, N. Lang, A. V. Pipa and J. Röpcke: *On determination of the degree of dissociation of hydrogen in non-equilibrium plasmas by means of emission spectroscopy: II. Experimental verification.* Plasma Sources Sci. T. **15** (1), p. 147 (2006). See page: 72

[15] A. V. Pipa: *On Determination of the Degree of Dissociation of Hydrogen in Non-Equillibrium Plasmas by Means of Emission Spectroscopy.* Logos, Berlin (2004). PhD thesis, EMAU Greifswald (1999). See page: 72

6. Summary and conclusion

In this work, the temperature of micro-particles confined in a low-pressure rf discharge was determined and the related energy balance of the particles has been studied. A suitable phosphor material has been found, showing temperature sensitive features which can be used for temperature measurement purposes in a plasma. Using micro-particles made from this material, systematic measurements of the particle temperature have been performed. To that purpose, discharge power and gas pressure have been varied in argon and, then, hydrogen and nitrogen was added to the discharge under low pressure conditions. Moreover, the applicability of the particles as a calorimetric probe was demonstrated. A simple balance model was used to describe the most important energy fluxes between the particle and the surrounding plasma environment. For the application of this model, the performance of additional plasma diagnostics was necessary. A summary of the main results and a final conclusion is given as follows:

The phosphor material used for the experiments in this thesis is suitable for the performance of temperature measurements in a wide temperature range and showed no degradation under the applied conditions. It can be excited by ultraviolet radiation and shows strong spectral emission intensity in a narrow spectral region. In this region, a change of the temperature causes strong changes in the emission spectrum which are reproducible. Thus, a comparison of the emission spectrum obtained under plasma conditions to calibration spectra measured at known temperatures allows the determination of the phosphor temperature. The statistical error of the measured particle temperatures in the plasma was commonly better than ± 5 K and approached values better than ± 1 K under optimal conditions. A systematic influence of warming the electrodes and the plasma reactor due to plasma operation could clearly be identified in the measured particle temperatures as well as in the monitored temperature of the lower electrode. This circumstance is a handicap for the long-term reproducibility of absolute experimental conditions because electrode temperature and particle temperature are strongly correlated. However, short term reproducibility is weakly affected if the system is close to equilibrium. Moreover, also the measurement of a small increase in the particle temperature caused by an external illumination source could be demonstrated. Furthermore, the expected response of the particle temperature to the plasma conditions was observed: With increasing discharge power also the particle temperature increased. At higher gas pressure, this behavior was generally less pronounced because of increased cooling of the micro-particles by the neutral gas.

For the description of the energy fluxes between micro-particle and plasma, a simple model was applied based on the OML currents to a spherical collector. At a pressure of 10 Pa, the assumption of orbital ion motion around the micro-particle is still justified. The observed trend that the particle temperature increases above

40 Pa could be a hint for the destruction of orbital motion and a resulting increase of ion and electron fluxes towards the particle surface, reinforcing the release of kinetic and recombination energy. In this model, an additional parameter α was introduced for the description of the time-averaged electron density at the particle position where no quasi-neutrality occurs. This factor also includes an electron sticking coefficient and is not known exactly but can be estimated. The floating potential of the micro-particle is calculated self-consistently from the balance of electron and ion currents. Also the required balance of total energy influx and total energy loss was obtained. Both floating potential and energy balance rely on the proper estimation of α. As expected, in a noble gas discharge the recombination of electrons and ions at the particle surface is the dominant process for particle heating in this model, delivering about 80% of the total energy influx, while the kinetic contributions of electrons and ions account for the remainder for the presented measurements.

Because the floating potential is strongly determining the flux of charge carriers towards the particle surface it is a basic parameter, which connects calorimetric and electrical approach. Thus, the measurement of both, floating potential and temperature of the same micro-particle (or macroscopic surface) could play a key role in future investigations.

If molecular gas is added to a noble gas discharge, electrons can perform inelastic collisions at very low energies, where rotational and vibrational molecular states are excited. Hence a pronounced drop in electron temperature occurs. By admixture of approximately 10% nitrogen or hydrogen also the particle temperature decreased, which can be addressed to the reduced electron temperature. In contrast to measurements in argon, the confinement of the particles became more difficult because of the smaller floating potential which is equivalent to a small particle charge. Unfortunately, the spectral overlap of particle and plasma emission increased, especially when nitrogen was added which shows broad emission bands in the investigated spectral region. Hence, the accuracy of the particle temperature measurements decreased in comparison to the argon discharge.

For the argon-hydrogen mixture the energy fluxes were modeled. Now, the complexity of the balance equation increases from multiple gas species, multiple ion species and from additional energy release at the particle surface by the association of dissociated hydrogen molecules. The individual ion densities were obtained from published PIC-MC simulations for similar plasma conditions which can be found in literature. The density of hydrogen atoms was assumed to be proportional to the electron density. The different contributions to particle heating deduced from the balance for the investigated gas mixture show a dominant role of recombination processes where free electrons and ions recombine at the particle surface which give approximately 70%. The recombination of dissociated hydrogen delivers about 20% to the total energy influx. The remaining kinetic contributions of electrons and ions are comparably small. As a result from the energy balance, the amount of atomic hydrogen can be estimated indirectly if its value for the sticking probability at the particle surface is estimated. The result is comparable to measurements published in literature, performed in hydrogen containing rf discharges close to metallic surfaces.

In this thesis it could be demonstrated that the measurement of the temperature

of micro-particles, confined in low-pressure rf discharges, can be performed with high temperature resolution. Furthermore it was possible to give a consistent description of the energy fluxes between plasma and particles, which determine the particle temperature, namely in an argon discharge and also under admixture of hydrogen. The application of more advanced theories could explain effects induced by increasing collisionality which can directly be observed in the temperature measurements. A combination of electrical and calorimetric measurements with the same substrate in future experiments would be of interest, because both are determined by the same physical processes. This could provide valuable experimental data and lead to a deeper understanding of plasma-surface interactions.

List of Figures

1.1. Northern lights in the cloudless sky over Bear Lake, Alaska at January 18, 2005. Photographer: Joshua Strang, USAF. Shown is the not digitally processed version of this famous photograph. Downloaded from [35]. 4
1.2. Dust pillar of the Eagle Nebula, photographed by the Hubble telescope by NASA, ESA, STScI/AURA. Downloaded from [36]. 4
1.3. Gas discharge being operated by Raymond W. Plamer at the Lewis Electromagnetic Propulsion Division, Cleveland, Ohio 1961. Photograph downloaded from [37]. 5
1.4. Dust cloud, formed in a processing plasma above three Si wafers and irradiated by a laser sheet, as published by G. Selwyn and co-workers in [38]. Image from [39]. 5
1.5. Plasma crystal, forming a single layer in the plasma sheath, illuminated by laser radiation. Image taken from [41]. 6
1.6. Scheme of a capacitively coupled rf discharge similar to PULVA-INP. Bottom electrode and vacuum chamber are grounded, the upper electrode is driven. Between the electrodes the plasma establishes, separated from the electrode surface by an rf sheath. 9
1.7. Simple sketch of the electron and ion population between two symmetrical rf electrodes. Here, the ion density (red) is assumed to be homogeneous and stationary, while the electrons (hatched area) move back and forth with the applied rf voltage. Also the time-averaged electron density (blue) is shown. 9
1.8. Micro-particle, confined in the rf sheath in front of an electrode (center). Its vertical equilibrium position is mainly determined by gravitational and electrostatic force F_g and F_{el} (left). The effective vertical confinement potential $\phi_{eff}(z)$ in the vicinity of the particle can be approximated by a parabolic potential well (right). 12

2.1. Ion trajectories in the presence of a negatively charged micro-sphere. Due to the attracting potential, the unbound ions move in hyperbolic orbits. 18
2.2. A sketch of current-voltage characteristics for different probe geometries in the OML regime. For demonstration purposes the ion temperature is strongly exaggerated. At the plasma potential V_p a sharp knee occurs in the planar probe current. The insert shows a detail of the marked region where $I(U)$ intersects the U axis. Historically the negative current is drawn in Langmuir probe current-voltage plots. 23

2.3. Scheme of the energy flux densities between a micro-particle and the surrounding plasma environment. The particle gains energy from the kinetic energy of electrons and ions, from their recombination and from plasma specific processes like the association of atoms at the particle surface. Energy loss occurs via conduction and radiation. 25

2.4. Energy influx density towards a planar surface, facing towards the plasma volume due to the contribution of charge carriers, modeled for $V_e = 1$ eV and $n_{e,0} = 1 \cdot 10^{16}$ m^{-3} in argon as well as with an admixture of 10% hydrogen in dependence of the electron duty cycle α. 28

2.5. The normalized floating potential χ of a planar surface, facing towards the plasma volume as a function of the electron duty cycle α for a spherical body in argon and an argon mixture with 10% hydrogen. 30

2.6. Temporal evolution of the substrate temperature in response to a plasma exposure of approximately 55 s duration. The heating and cooling of the substrate can be described by an exponential law. . . 31

3.1. Energy levels of the hydrogen atom and the possibilities of fluorescent emission after excitation to $n = 3$. 35

3.2. Configurational coordinate diagram for an activator ion in a solid. Shown is the path of excitation and emission between ground state GS and an excited state ES, and the role of vibrational levels. 36

3.3. Experimental setup for the characterization of phosphor samples. A certain wavelength from the emission spectrum of a high pressure Hg vapor lamp is selected by a monochromator (SPM2) and focused onto the phosphor sample, placed inside an oven. The temperature inside the oven is monitored via a temperature sensor (PT), the temperature is adjusted by changing the heating current provided by a power supply (U,I). Phosphor emission is collected and guided to a spectrograph with an intensified CCD camera (OMA). 40

3.4. Emission of three phosphor samples at different temperatures - from top to bottom: Y_2O_3:Eu, YVO_4:Dy, YVO_4:Eu. Emission intensity is normalized to the maximum of a well-defined emission peak. . . . 41

3.5. Emission intensity of the 616.5 nm line of YVO_4:Eu, normalized to that of the 619.4 nm line (taken at the maxima). The measurements are shown for an excitation wavelength of $\lambda_{exc} = 313$ nm. The points are well reproducible. 42

3.6. Emission intensity (619.4 nm peak of YVO_4:Eu) under 365 nm excitation, normalized to emission at 313 nm excitation. In the region from room temperature to 350° C this ratio is monotonically increasing and very sensitive. However, as the jump at 373 K reveals the reproducibility under the experimental conditions (see text) is poor. 43

4.1. Scheme of PULVA-INP and the experimental setup: RF - driven electrode, AE - Adaptive Electrode. For the Langmuir and calorimetric probe measurements: LPS - Langmuir probe system, CPS - calorimetric probe system. For the particle temperature measurements: OMA - optical multichannel analyzer, FOS - fiber optical system, FW - filter wheel, HG - mercury arc lamp. 46
4.2. Photographs of the experiment PULVA-INP, located at the Institute for Plasma Science and Technology e.V. (INP) in Greifswald, Germany. 47
4.3. Partial gas flow vs. partial pressure in argon-molecular gas admixtures. Total gas flow is 20 sccm at a total gas pressure of $p_{\mathrm{gas}} = 10$ Pa. 48
4.4. Plasma parameters V_{e} and n_{e} in argon at a position of 15.5 mm above the AE, measured with the Smart Probe at different gas pressures and discharge powers. 49
4.5. Plasma parameters V_{e} and n_{e} at a gas pressure of $p_{\mathrm{gas}} = 10$ Pa in different gas mixtures, measured 15.5 mm above the AE. In (b) also the electron density measured 27 mm above the AE is shown. 50
4.6. The emission of the YVO_4:Eu particles (gray area) is obtained by the difference of the emission spectrum of excited phosphor particles in the plasma (black area) and the plasma background (white line). . 52
4.7. Oven for calibration measurements. It consists of a copper block, heated by an electrical heating wire. The wire is spooled around an insulating ceramic shell. Thermal insulation is maintained from ceramic fleece. The copper block (right) can contain a copper object holder (left) or a quartz cuvette (middle). 52
4.8. Residuals $R(T)$ calculated as described in eqn. (4.2) and fitted with a sixth-order polynomial. The resulting particle temperature is the minimum temperature value in the fit, which is 34.9° C in this example. 53
4.9. Particle temperature T_μ and electrode temperature T_{AE} as a function of gas pressure for a discharge power P_{rf} of (a) 10 W, (b) 20 W, (c) 50 W and (d) 80 W. Error bars for T_μ show the standard deviation of 10 subsequent measurements. 54
4.10. Particle temperature T_μ and electrode temperature T_{AE} as a function of discharge power for different gas pressures in argon. From top to bottom: $p_{\mathrm{Ar}} = 10$, 20, 30 and 50 Pa. The shown error bars for T_μ describe the standard deviation of 10 subsequent measurements. . . 55
4.11. Sketch of the sequence of plasma conditions for the measurement of the particle temperature in argon. Especially at high discharge power and low gas pressure, the chamber heats up quickly. To keep the temperature changes between successive measurements as small as possible, the shown order was chosen for the sequence of discharge conditions. 57
4.12. Particle temperature T_μ and electrode temperature T_{AE} as a function of discharge power at $p_{\mathrm{gas}} = 10$ Pa in argon-molecular gas mixtures. The shown error bars for T_μ describe the standard deviation of 10 subsequent measurements. 58

4.13. Scheme of the Calorimetric probe. Electrical connections from thermocouple and substrate to the electronic box are fed through the probe shaft. 59
4.14. Energy influx density to the dummy surface at different gas pressures. From top to bottom: $p_{\mathrm{Ar}} = 10$, 20, 30 and 50 Pa. The value at $p_{\mathrm{Ar}} = 30$ Pa and $P_{\mathrm{rf}} = 50$ W has been excluded for the fit. 60

5.1. Probe characteristic and EEDF measured in PULVA-INP. The noise in the measured derivatives and the EEDF results from a relatively large distance between neighboring bias values in the measurement. . 64
5.2. The ratio V_f/V_{e} under different plasma conditions, measured by a Langmuir probe. 65
5.3. Energy influx density measured at the dummy substrate, compared to model calculations based on the assumption of a plane and a cylindrical substrate geometry. 66
5.4. Current-voltage characteristics of the calorimetric probe, measured by a digital multimeter. The lines are drawn to guide the eye. 66
5.5. Comparison of the total energy fluxes in 10 Pa argon. 68
5.6. Comparison of the different contributions to the total energy flux densities shown in fig. 5.5 in a 10 Pa Ar discharge. 69
5.7. Comparison of the total energy fluxes in the argon-hydrogen mixture 70
5.8. Comparison of the different contributions to the total energy flux densities shown in fig. 5.7 in a 10 Pa Ar discharge. 71

List of Tables

2.1. Specific constants of the most important species in an Ar-H_2 plasma [16, 17, 18]. The dissociation energies of the ions refer to the reactions $H_3^+ \rightarrow H_2 + H^+$ and $ArH^+ \rightarrow Ar + H^+$, after [19, 20]. 28

4.1. Comparison of mass densities and melting points of common microparticles to those uf the phosphor particles 57

A. List of abbreviations

Acronyms

ac	alternating current
AE	adaptive electrode
CCD	charge coupled device
dc	direct current
EEDF	electron energy distribution function
ICCD	intensified charge coupled device
OML	Orbital Motion Limited
OM	orbital motion
rf	radio frequency
uv	ultraviolet

Important constants and symbols

Constants

$\varepsilon_0 = 8.854 \cdot 10^{-12}$ C/(Vm)	vacuum permittivity
$\sigma = 5.67 \cdot 10^{-8}$ W/(m^{2}K^4)	Stefan Boltzmann constant
$g = \lvert\vec{g}\rvert = 9.81$ m/s^2	earth's gravity field strength at sea level
$e_0 = 1.602 \cdot 10^{-19}$ C	elementary charge
$k_\mathrm{B} = 1.38 \cdot 10^{-23}$ J/K	Boltzmann constant
α_μ	accomodation coefficient
γ	adiabatic exponent
Γ	association probability
η	geometric correction factor for streaming ion density
ε	emissivity

Symbols

index 0	quantity inside the plasma volume, if not defined explicitly
index AE	Adaptive Electrode-
index e	electron-
index env	environment-
index gas	gas-
index i	ion-
index μ	micro-particle-
index i	plasma-

index rf	radio-frequency-
index s	quantity at the plasma sheath edge
α	electron duty cycle (plus sticking coefficient) [-]
β	geometric correction exponent [-]
χ	normalized floating potential [-]
$\phi_{\text{eff}} = \int F_{\text{eff}}\, dz$	effective confinement potential
Φ_{C}	Coulomb potential [J/C]
Φ_{D}	Debye-Hückel (Yukawa) potential [J/C]
λ_{D}	Debye length [m]
τ	time interval [s]
ω	angular frequency [1/s]
A	surface area [m^2]
b_{c}	critical impact factor [m]
C	capacitance [F]
C_{S}	heat capacity [J/K]
E	Energy [J], also electric field strength [V/m]
E_{diss}	dissociation energy [eV]
E_{ion}	ionization energy [eV]
E_{kin}	kinetic energy [eV]
$f(v)$	speed distribution function [1/v]
$f_{\text{M}}(v)$	Maxwellian speed distribution function [1/v]
F	force [N]
I	current [A]
j	flux density [$1/\text{m}^2$]
J	energy flux density [W/m^2]
J_{ass}	energy influx density from recombination of dissociated molecules [W/m^2]
J_{cond}	energy loss density due to gas conduction [W/m^2]
J_{e}	energy influx density due to kinetic electrons [W/m^2]
J_{i}	energy influx density due to kinetic ions [W/m^2]
J_{in}	integral energy influx density [W/m^2]
J_{out}	integral energy loss density [W/m^2]
J_{rad}	energy loss density due to radiation [W/m^2]
J_{rec}	energy influx density due to recombination of electrons and ions [W/m^2]
m	mass [kg]
n	density [$1/\text{m}^3$]
p	pressure [Pa]
P	power [W]
Q	charge [C]
r	length, radius [m]
T	temperature [K]
U	voltage [V]
v	velocity [m/s^2]
v_{B}	ion sound (Bohm) velocity [m/s]
v_{th}	thermal velocity [m/s]
V	bias, electrical potential (for electrons also: temperature) [V]
V_f	floating potential [V]

z	vertical coordinate [m]
Z	number of (positive) elementary charges

List of publications

Publications in peer-reviewed journals

Parts of this thesis have previously been published or submitted to the following journals:

H. R. Maurer, R. Basner and H. Kersten: *Temperature of Particulates in Low-Pressure rf-Plasmas in Ar, Ar/H2 and Ar/N2 Mixtures.*
Contrib. Plasm. Phys. **50** (10), pp. 1521-3986 (2010).

H. R. Maurer, S., M. Hannemann, R. Basner and H. Kersten: *Measurement of plasma-surface energy fluxes in an argon rf-discharge by means of calorimetric probes and fluorescent microparticles.*
Phys. Plasmas **17** (11), p. 113707 (2010).

H. R. Maurer, V. Schneider, M. Wolter, R. Basner, T. Trottenberg and H. Kersten: *Microparticles as plasma diagnostic tools.* Manuscript accepted for publication in Contr. Plas. Phys. Special Issue for the 2010 International Conference on Plasma Diagnostics.

Further peer-reviewed publications:

H. Maurer, R. Basner and H. Kersten: *Measuring the temperature of microparticles in plasmas.*
Rev. Sci. Instrum. **79** (9), 093508 (2008).

Contributions to international conferences

H. Maurer, R. Basner and H. Kersten: *Micro-Particles As Thermal Probes In Plasmas.* AIP Conf. Proc. **1041**, pp. 283–284. AIP (2008).

H. R. Maurer, H. Kersten and R. Basner: *Temperature of micro-particles in a low-pressure rf-discharge.*
Plasma Science, 2010 Abstracts IEEE International Conference on, 7A-4.

Danksagung

An erster Stelle möchte ich mich herzlich bei Herrn Prof. Dr. Holger Kersten bedanken, der mir die Möglichkeit zur Anfertigung der Dissertation in seiner Arbeitsgruppe gegeben hat. Trotz oftmals vollem Terminplan hatte er immer ein offenes Ohr für Fragen und Ideen, und seine guten Kontakte spielten eine entscheidende Rolle bei der Durchführung der Arbeit. Insbesondere gebührt auch Herrn Dr. Ralf Basner (INP Greifswald) herzlicher Dank, der als mein Betreuer in Greifswald ebenfalls jederzeit für Frangen offen war und der duch sein analytisches und gründliches Denken wichtige Fragestellungen angeregt hat. Bei Herrn Prof. Dr. Klaus-Dieter Weltmann möchte ich mich für die Möglichkeit bedanken, meine experimentellen Arbeiten am INP Greifswald durchführen zu können und dabei auf eine hervorragende wissenschaftliche Infrastruktur zugreifen zu können. Mein Dank gilt ebenfalls Herrn Dr. Volker Brüser und der Arbeitsgruppe 'Oberflächen und Materialien', in der ich meine Experimente durchführte.

An dieser Stelle möchte ich mich weiterhin bei den zahlreichen Kollegen am INP sowie am IfP Greifswald, die mir mit wissenschaftlichem Gerät und Gesprächen zur Seite standen, insbesondere Prof. Dr. Röpcke, Prof. Dr. Hippler und Dr. Lange bedanken. Herrn Dr. Jörn Winter und Herrn Dr. Hoang Tung Do möchte ich für ihre Unterstützung bei der Durchführung von TDLAS-Messungen danken, Herr Dr. Andrei Pipa für die zahlreichen Diskussionen zur optischer Messung des Dissoziationsgrades in Molekülgasen, sowie Herrn Dr. Mario Hannemann für die Bereitstellung der Lamgmuirsonde. Weiterer Dank gilt Herrn Prof. Dr. Harm Wulff, der als kompetenter Ansprechpartner für die Beschaffung von Leuchtstoffproben und Diskussionen zur Verfügung stand. Am IEAP in Kiel danke ich der gesamten Arbeitsgruppe 'Plasmatechnologie' für die angenehme Atmosphäre, insbesondere bei Herrn Marc Stahl für seine Hilfestellung bei der Durchführung der Thermosondenmessungen und Herrn Dr. Thomas Trottenberg für zahlreiche Diskussionen, sein immer offenes Ohr und sein kritisches Urteil beim Korrekturlesen.

Nicht zuletzt möchte ich bei meiner Familie und meinen Freunden bedanken für die moralische Unterstützung bei der Anfertigung dieser Arbeit.

Diese Arbeit wurde finanziert von der Deutschen Forschungsgesellschaft (DFG) unter dem Projekt SFB-TR 24 B4.

Wissenschaftlicher Werdegang

Name		Maurer, Horst R.
geboren:		10.07.1973 in Meersburg am Bodensee
Staatsangehörigkeit		deutsch
Schule	1993	Abitur am Droste-Hülshoff-Gymnasium in Meersburg, Leistungskurse Mathematik und Kunst
Dienst	1995 - 1996	Zivildienst in der individuellen Schwerstbehindertenbetreuung, Arbeiterwohlfahrt Freiburg i. Br.
Ausbildung	1996 - 2001	Tischlerlehre in Überlingen, anschliessende Tätigkeit als Tischler in Überlingen und Kiel
Studium:	WS 2001/02	Immatrikulation an der Christian-Albrechts-Universität zu Kiel, Studiengang: Physikalische Ozeanographie (Diplom)
	WS 2003/03	Vordiplom im Studiengang Physikalische Ozeanographie, Studiengangwechsel in den Studiengang Physik (Diplom)
	2005	Diplom-Hauptprüfung, Nebenfach Physikalische Ozeanographie
	WS 2005/06 - WS 2006/07	Anfertigung der Diplomarbeit “Experiment zur Demonstration grundlegender Phänomene Staubiger Plasmen” in der Arbeitsgruppe “Plasmadynamik” am Institut für Experimentelle und Angewandte Physik an der Christian-Albrechts-Universität zu Kiel
	SS 2007 - WS 2010/11	Promotion in der Arbeitsgruppe “Plasmatechnologie” am Institut für Experimentelle und Angewandte Physik an der Christian-Albrechts-Universität zu Kiel
	SS 2007 - SS 2010	Im Rahmen der Promotion angestellt als Wissenschaftlicher Mitarbeiter am Institut für Plasmaforschung und Technologie e.V. in Greifswald

Eidesstattliche Erklärung

Hiermit versichere ich an Eides Statt, dass die vorliegende Dissertation - abgesehen von der Beratung durch meinen wissenschaftlichen Lehrer und der Verwendung der angegebenen Hilfsmittel - nach Inhalt und Form meine eigene ist. Sie hat weder ganz noch teilweise an einer anderen Stelle im Rahmen eines Prüfungsverfahrens vorgelegen. Die Arbeit ist unter Einhaltung der Regeln der Deutschen Forschungsgemeinschaft zur Sicherung guter wissenschaftlicher Praxis entstanden.

Kiel, den